QUASI-BRITTLE SELF-HEALING MATERIALS: NUMERICAL MODELLING AND APPLICATIONS IN CIVIL ENGINEERING

TRAN DIEP PHUOC THAO

NATIONAL UNIVERSITY OF SINGAPORE

2011

QUASI-BRITTLE SELF-HEALING MATERIALS: NUMERICAL MODELLING AND APPLICATIONS IN CIVIL ENGINEERING

TRAN DIEP PHUOC THAO

(B.Eng. Civil (Hons))

A THESIS SUBMITTED

FOR THE DEGREE OF DOCTOR OF PHILOSOPHY

DEPARTMENT OF CIVIL AND ENVIRONMENTAL ENGINEERING

NATIONAL UNIVERSITY OF SINGAPORE

2011

Acknowledgements

Table of Contents

Summary

Self-healing materials (SHM) is a novel class of smart material which can detect and repair damages automatically. From the beginning, researches in this field have been targeted towards aerospace applications. Multiple experiments have been conducted to enhance the self-healing performance. To complement the experimental effort, a numerical model that is able to predict the macro behaviour of this composite is necessary. To tap on the potential of this smart material, attempts have been made to extend the self-healing concepts to cementitious materials for civil engineering applications, where the automatic crack repair can help to increase the durability of the material or to reduce the loss of stiffness and strength of the structure. The objectives of the current study are to develop a numerical modelling strategy that can efficiently predict the macro behaviour of SHM and to extend the self-healing concept to reinforced concrete, the most commonly used civil engineering material.

Firstly, Representative Volume Element (RVE) approach was examined in detail based on simulations with porous epoxy. The simulations show that Multiple-Particle RVE (MP-RVE) approach is suitable for predicting the properties, both elastic and inelastic, of composites containing high volume fraction of reinforcements; and fracture energy, which is a size invariant property, should be used to simulate the damage behaviour of heterogeneous materials.

The RVE approach has been adopted to develop a numerical model to predict material properties of micro-capsule based SHM. Findings from a preliminary study suggest that the micro-capsules, which are much softer than the matrix, can be modelled as voids in the RVEs. The shear-yielding effect of the micro-capsules on the

post-elastic behaviour of the composite is modelled by introducing shear retention in the smeared crack model. Good predictions of Young's modulus, strength, and healing efficiency have been achieved.

A numerical simulation of simply supported beam under three-point bend was carried out to study the effect of self-healing on structural behaviour. The result shows that healing with low strength healing agent is inefficient as the healed cracks will reopen. Ideally, self-healing beam using capsulated system may recover load bearing capacity and stiffness better but this system need more amount of healing agent. On the other hand, self-healing beam using tubular system sacrifices some degree of healing to concentrate on healing only severe cracks.

Lastly, self-healing function was implemented in reinforced concrete as an extension of self-healing concept to civil engineering applications. It was found that the one-part air curing adhesive Isocyanate Prepolymer (POR-15) encapsulated in a hollow glass tubes is a promising self-healing unit. Protected by using spiral wires coated with a thin mortar layer, the proposed self-healing units were implemented in three key reinforced concrete structural members, at structural scale, namely beam, column and slab to test the healing efficiency, in terms of stiffness recovery. The self-healing beam exhibited multiple crack healing capabilities with 84% of the flexural stiffness being recovered. Self-healing function was also introduced in column element where healing efficiency of up to 70% was reported. Multiple crack healings were observed in the self-healing slab with the maximum healing efficiency of 99%.

List of Tables

List of Figures

List of Symbols

a	Edge length of RVE
D	Diameter of inclusion
E	Young's modulus
f	Volume fraction of inclusion
G	Shear modulus
G_{cr}	Cracked shear modulus
G_f	Fracture energy
I_1	Deviatoric strain invariant
K	Bulk modulus
K_{IC}	Fracture toughness of material
n	Number of inclusions
S	Eshelby tensor
U	Strain energy potention
u	Displacement
V	Volume
w_{max}	Maximum crack opening displacement
x	Coordinate
ε	Strain
ε_c	Constrained strain
ε_t	Eigenstrain

ε_{cr}	Direct strain across the crack
ε_{max}	Direct strain across the crack corresponding to the zero shear retention state
λ	Principle stretch
η	Healing efficiency
ν	Poisson's ratio
ρ	Shear retention factor
σ	Stress
σ_f	Strength of material

List of Acronyms

BC	Boundary Condition
CSA	Composite Sphere Assemblage
DCB	Double Cantilever Beam
DD	Dilute Distribution
FEM	Finite Element Method
GSC	Generalizes Self Consistent
HGF	Hollow Glass Fiber
MP-RVE	Multiple-Particle RVE
PBCs	Periodic Boundary Conditions
RSA	Random Sequential Adsorption
RVE	Representative Volume Element
SC	Self Consistent
SEM	Scanning Electron Microscope
SHB	Self-Healing Beam
SHC	Self-Healing Column
SHM	Self-Healing Materials
SHU	Self-Healing Unit
SP-RVE	Single-Particle RVE

THIS PAGE IS INTENTIONALLY LEFT BLANK

CHAPTER 1

INTRODUCTION

1.1.   GENERAL REMARKS

Along the development of material science, the objective of material research, in terms of mechanical behavior, keeps changing from the starting point of finding stronger materials finding high performance materials. Over a few recent decades, advanced materials such as smart materials, multi-functional materials and sustainable materials have attracted the attention of material scientists. No matter how the focus in material research changes, cracking is always the essential issue need to be resolved. The existence of crack in material, regardless of how well it is designed or manufactured, is almost unavoidable as micro-cracks can be initiated during the processing of the material due to non-uniform heating and cooling which give rise to residual stresses, or rough handling of the material. Owing to the creep or fatigue effects during service condition caused by electrical, mechanical and/or thermal loading, these micro-cracks can grow and induced more severe macro-cracking phenomenon such as crack bridging at grain boundaries, debonding at matrix–reinforcement interface or delamination in sandwich or laminated panels, resulting in degradation of material properties.

In materials which are brittle or quasi-brittle, such as polymer composites and concrete, the long-term degradation is highly undesirable. Especially, when the structure

is under-designed or accidental loadings are imposed, the presence of cracks at critical locations increases the vulnerability of the structure. In such cases, if the damage structure is left unrepaired, a sudden catastrophic structural failure may happen and cause some severe losses in property or even human death. Thus, overhaul or regular maintenance, which is costly in many cases particularly in civil and aerospace applications, is necessary to ensure safety and prolong the lifespan of the structure. For example, the average annual maintenance cost for bridges in US is estimated at $5.2 billion (Yunovich and Thompson, 2003). Even with a costly regular maintenance and overhaul, the probability that a catastrophic failure happen can only be reduced to a certain level, rather than being zero as in ideal cases. The collapse of a highway overpass in Quebec in 2006, which happened after the annual inspection, is an obvious example. The fact that the probability of a sudden catastrophic failure cannot be reduced to zero is because in many instances, including of the above failure of the highway overpass in Quebec, damages are too fine or embedded too deep inside the structure so that they cannot be detected by conventional methods and equipments. Therefore, finding a reliable detection and repair method to solve cracking problem is a very challenging and practical issue nowadays.

As a promising solution for the aforementioned cracking problem, self-healing materials has become an attractive topic to researchers over the past few years. The main idea of this novel material is to embed a self-sensing and repairing mechanism within the materials to prevent further damage and recover its material properties such as stiffness, strength and fracture toughness automatically. Indeed, this self-healing system is not entirely new and can be found in almost all living organisms. Through years of evolution,

the sensing and healing network in biological materials are optimized to adapt to their living environment. Obvious examples are the growth of tissue in cuts and abrasions of animal skin, or the remodeling of bone when there are fractured. Mimicking nature, many efforts have been made, experimentally, to find efficient ways to produce self-healing materials and some first promising results have been published recently.

In the next section of this chapter, the self-healing mechanisms in nature will be reviewed in detail. Then, a general strategy to create artificial self-healing mechanism in material will be presented together with a review on achievements in literature.

1.2. LITERATURE REVIEWS

1.2.1. Natural self-healing systems

In nature, living organisms heal themselves by either replacement or bleeding mechanism. The former mechanism is exhibited in the repair of bones with micro stress fractures or the repair of trees from cutting. Figure 1.1 describes the replacement mechanism in human bone. There are 2 different types of cells, the osteoclasts and the osteoblasts, within each repair unit called basic multicellular unit (BMU). While the osteoclasts remove the old and damaged part of the bone, the osteoblasts generate new ones to maintain the bone's integrity. In order to mimic this mechanism artificially, one has to create two separate automatic systems for destruction and generation, which is still at present formidable to mimic. Moreover, effective bonding between new and old material is another difficult issue to content with satisfactorily.
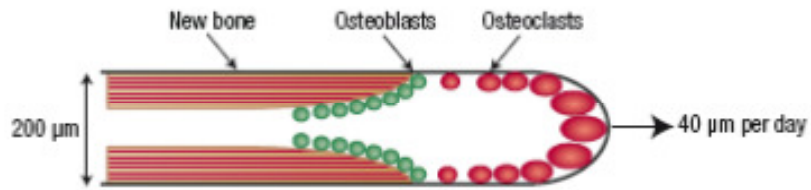
Figure 1.1: Replacement-based healing mechanism of human bone.
(after David Taylor et al., 2007)

Fortunately, there is a simpler way of self-repair in nature which is based on bleeding mechanism. Figure 1.2 shows an example of bleeding-based autonomic healing process. When a cut through an animal skin is made, the intercepted blood vessels rupture and blood is released into the cut or wound. The blood functions as a self healing agent that contains clotting chemicals which can coagulate and mend the wound. The two key factors of this mechanism are (a) presence of a healing agent (blood) which is stored in containers (vessels), and (b) the damage has to rupture the containers to trigger the healing process. Compared to replacement mechanism, this approach is more practical and easier to mimic.
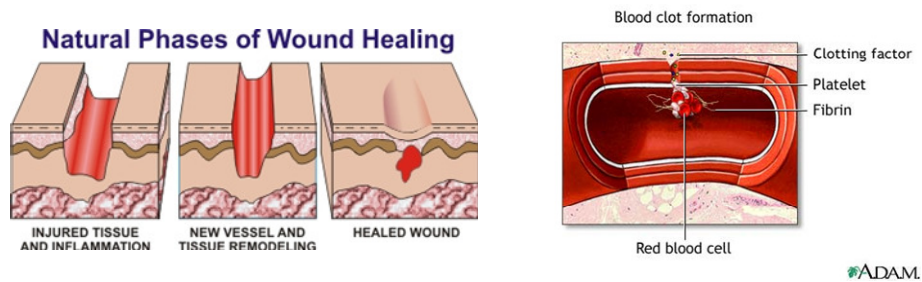
Figure 1.2: Bleeding-based healing mechanism.
(after Martha J. Heil, 2005 and William Matsui, 2007)

1.2.2. Artificial self-healing systems

1.2.2.1. Strategy to create artificial self-healing system

An artificial strategy to create autonomic repairing ability in material has been developed in recent years, which mimics closely the bleeding-based healing mechanism. The strategy is described by the flow diagram in Figure 1.3. Mimicking the bleeding-based healing mechanism in nature, the artificial self healing units comprise of the container and healing agent. These units are embedded inside the neat material to create the self healing function. The container serves both to contain the healing agent and act as a barrier to prevent any reactions between the healing agent and the neat material. When the propagating crack ruptures the container, the healing agent is released into the crack by capillary action or gravity. Chemical reaction takes place between the healing agent and neat material or between parts of healing agent (in the case of 2-parts epoxy) to create bonding between the crack planes and alter the crack tip's shape. Because of this healing process, it can stop the crack propagation and material properties such as stiffness, fracture toughness and strength may be recovered.
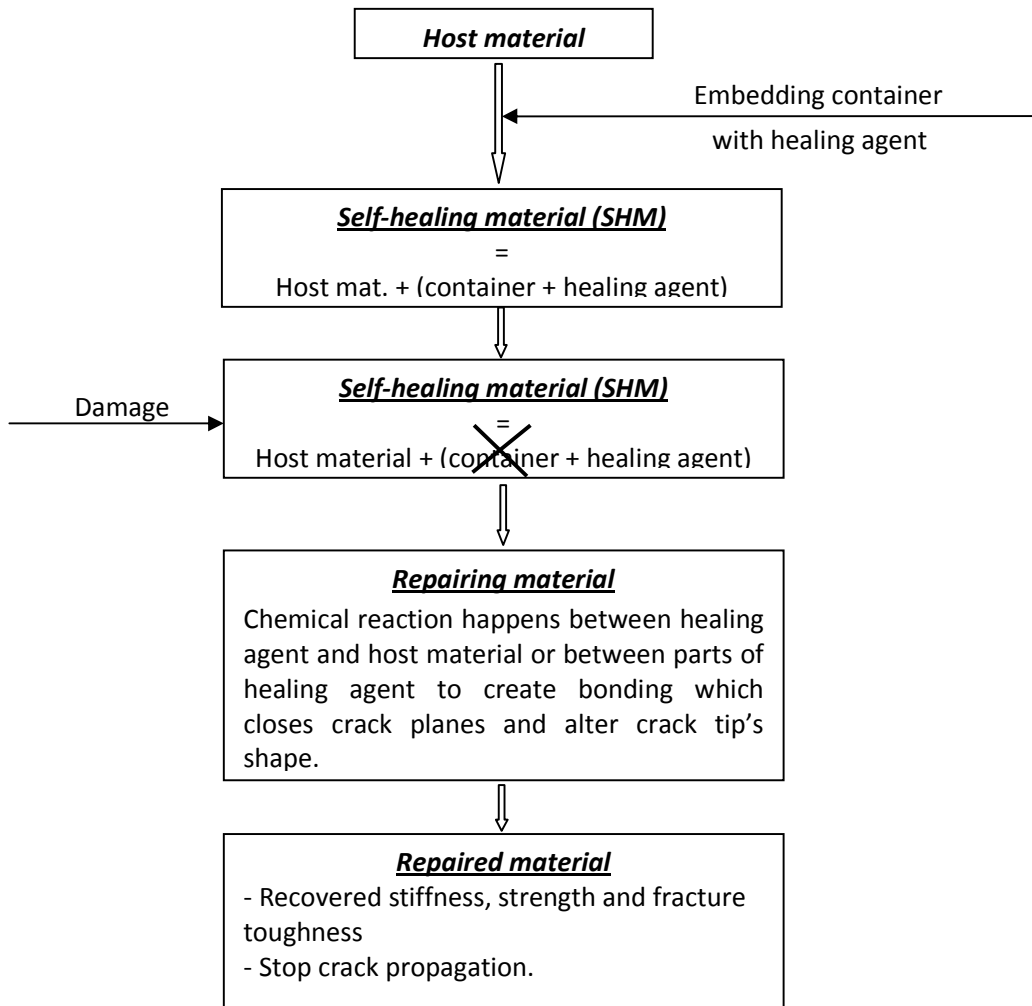
Figure 1.3: Strategy to create artificial self–healing material

Beside the liquid state healing agent which can provide fast chemical reaction to heal the damage, solid state healing agent have been proposed and developed in other systems. For such systems, the container is not necessary because under normal condition, solid healing agent cannot flow nor have chemical reaction with the host material. Instead, chemical reaction is triggered by methods such as heat (Zako and Takano, 1999; Chen et al., 2002; Hayes et al., 2005), light (Chung et al., 2004), or electric current (Christopher et al., 2007). However, such system requires a

complementary damage sensing system, making it more expensive and comparatively less responsive. Additionally, it is difficult to ensure localized healing at the damage area as a wider area is often activated by the trigger. It is not surprising that liquid healing agent is commonly selected as the principal component in the development of self-healing material.

The development of self-healing material requires the integration of multidisciplinary sciences from material, mechanical and chemical fields to find the optimal healing agent and container for each specific class of application. The role of the chemical scientists is to find or develop chemical agents which have the ability to create new chemical bonds that can repair the damage, and to find catalyst that can increase the speed of repair. These aspects are relevant to the chemical and physical properties of the self-healing units and their surrounding environment such as the matrix and the working environment of the whole self-healing structure. Studies on finding and developing chemical agents have been studied vigorously by White et al. (2001), Chen et al. (2002), Jones et al. (2006), Mauldin et al. (2007), Kersey et al. (2007), Wilson et al. (2008, 2009), Caruso et al. (2008), Blaiszik et al. (2009), Kryger et al. (2010), McIlroy et al. (2010), Kingsbury et al. (2011) and Jin et al. (2012) with promising results.

Beside epoxies and adhesives, some bacteria are also used as healing agents in recent researches on self-healing cementitious materials (Kishi et al., 2007; Van Tittelboom et al., 2010 and Jonkers H.M., 2007, 2009). In these studies, bacteria were used to activate the autogeneous healing process of cementitious materials. Experiments with lab-scale beam specimens showed that good results, in terms of crack sealing and increasing the water permeability ability have been achieved.

The selection of appropriate container system has received pursued by material and mechanical scientists and engineers. Two systems have been widely discussed and developed, namely, hollow glass fibers and microcapsules. Both systems have been demonstrated by some pioneered studies sponsored by the US Air Force Office of Scientific Research – AFOSR (Kessler and White, 2001; Kessler et al., 2003; Keller et al., 2007, 2008) and European Space Agency – ESA (Trask et al., 2006a, 2006b) to have enormous practical potential. However, practical limitations still have to be overcome.

1.2.2.2. Bio-inspired self-healing materials with tubular systems

The idea of using tubular system for self-healing material was first come in 1992 when researchers in civil engineering were trying to find a smart cementitious material. Initially, hollow glass fibers were chosen as the container of the healing agnet because it is chemically non-reactive and brittle, which may provide a timely rupture to trigger the healing process when the host material surrounding it is damaged.

Dry and coworkers (Dry, 1992, 1994; Dry and McMillan, 1996) were the first researchers to propose the use of hollow glass fibers as a potential container for a repair system of cracks in concrete. The experiments were conduct at lab-scale with two different modes, namely active modes and passive modes. In the active mode, crack healing was triggered through the release of liquid methyl methacrylate from hollow wax coated fibers embedded in the concrete. When heat was applied to the concrete, the wax coating melted releasing the methyl methacrylate and with further heating, the healing agent will be polymerized to bond the crack faces. In the passive mode design, the self-

healing units with hollow glass fibers as containers and methyl methacrylate as healing agent were adopted. The results showed that active mode design can improve the permeability while passive mode design was able to increase the flexural toughening. However, the glass fibers were so fragile that premature broken of glass tubes were often observed. Additionally, since there is a need of applied heat, the active self-healing system cannot be considered as a full autonomic self-healing system.

Li et al. (1998) and Joseph et al. (2007) studied the possibility of using air-cured chemical (ethyl cyanoacrylate) within a hollow brittle glass tube to implement the self-healing system in a fiber reinforced engineered cementitious composite. The reinforced fibers were used to as a mean to control crack width. The observations from experiments with lab-scale beams showed that healing agent can be drawn to the crack surface under capillary suction and gravity. In addition, self-healing process can be repeated at least twice with a reported flexural stiffness recovery up to 90%, and 70% in the first and the second instances of healing, respectively.

Nishiwaki et al. (2006) combined a self-diagnosis system with a healing system comprising of repair agent encapsulated in heat-plasticity organic film pipe and electric sensors as can be seen in Figure 1.4. When the crack is developed to a certain degree of severity, the sensor increases its resistance leading to the melting of organic film pipe and then the flowing of healing agent to seal the crack. Since the healing agent is compartmentalized, multiple healings can be achieved. However, the drawback of this system is the need of provide electric power continuously, which limit it from large scale applications. Additionally, recovered properties of the healed structure have not been reported yet.
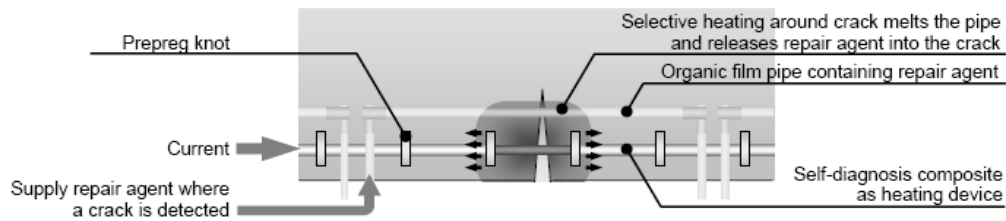
Figure 1.4: Selective healing system (Nishiwaki et al., 2006).

After some first promising result obtained with self-healing cementitious material using tubular system, Motuku et al. (1999) adapted this method to polymeric composites reinforced with woven S2-glass fabric. The study is basically a proof-of-concept and investigated the suitability of glass, copper and aluminum as hollow fiber material to house the healing agent, and vinyl ester 411-C50 and EPON-862 epoxy as the healing agent. Although the author concluded that the combination of glass tube and EPON-862 epoxy is effective in healing the crack, the mechanical properties of the composite after healing were not reported.

Bleay et al. (2001) provided a scheme for filling micro-diameter hollow fibers with healing agent to come up with a self-healing fiber laminate composite. The compressive strength of the damaged composite after healing was 10% higher than that of the untreated one. The study illustrated 3 healing systems as depicted in Figure 1.5. The first comprises hollow fibres filled with one-part resin, whereas the second is a 2-part resin system with the resin and hardener stored in separate hollow fibres. The second system allows faster chemical reaction but there may be occasions when bleeding resins do not meet hardening agent. The third system is a variation of the second system with the hardener encapsulated in micro-spherical modules interspersed in the matrix.
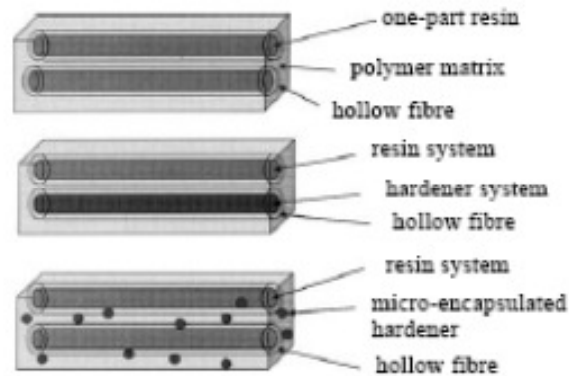
Figure 1.5: Schematic of different hollow fiber SHM approaches (Bleay *et al.,* 2001).

The work of Bleay et al. (2001) has since been extended at Bristol University for composite laminate (Pang and Bond, 2005a, 2005b; Trask and Bond, 2006; Trask et al., 2006a, 2006b; Bond et al., 2007) under the European Space Agency (ESA) research programme. The host is E-glass/913 epoxy composite laminate, aligned in each ply with hollow glass fibers of 60-micron outer diameter and 35-micron inside diameter spread uniformly at a predefined separation distance. The healing agent is a 2-part epoxy system (Cycom 823 epoxy). The self-healing composites are manufactured as pre-impregnated sheet with 900 stacking sequence. Damage was induced through indentation and specimens were then left to heal at a temperature of 100°C for 2 hours, after which a 4-point bend test was carried out. The strengths of virgin, damaged and healed specimens were compared as a measure of healing efficiency. It was reported that up to 87% strength can be recovered after healing. The experimental results are shown in Figure 1.6. The choice of healing agent, types of hollow glass tubes, diameter of the tubes, and distance between the tubes were also investigated. The performance of liquid healing agent at high temperature, and end-capping of the hollow tubes were studied.

<div align="center">(a)   (b)   (c)</div>

(e)

(d)
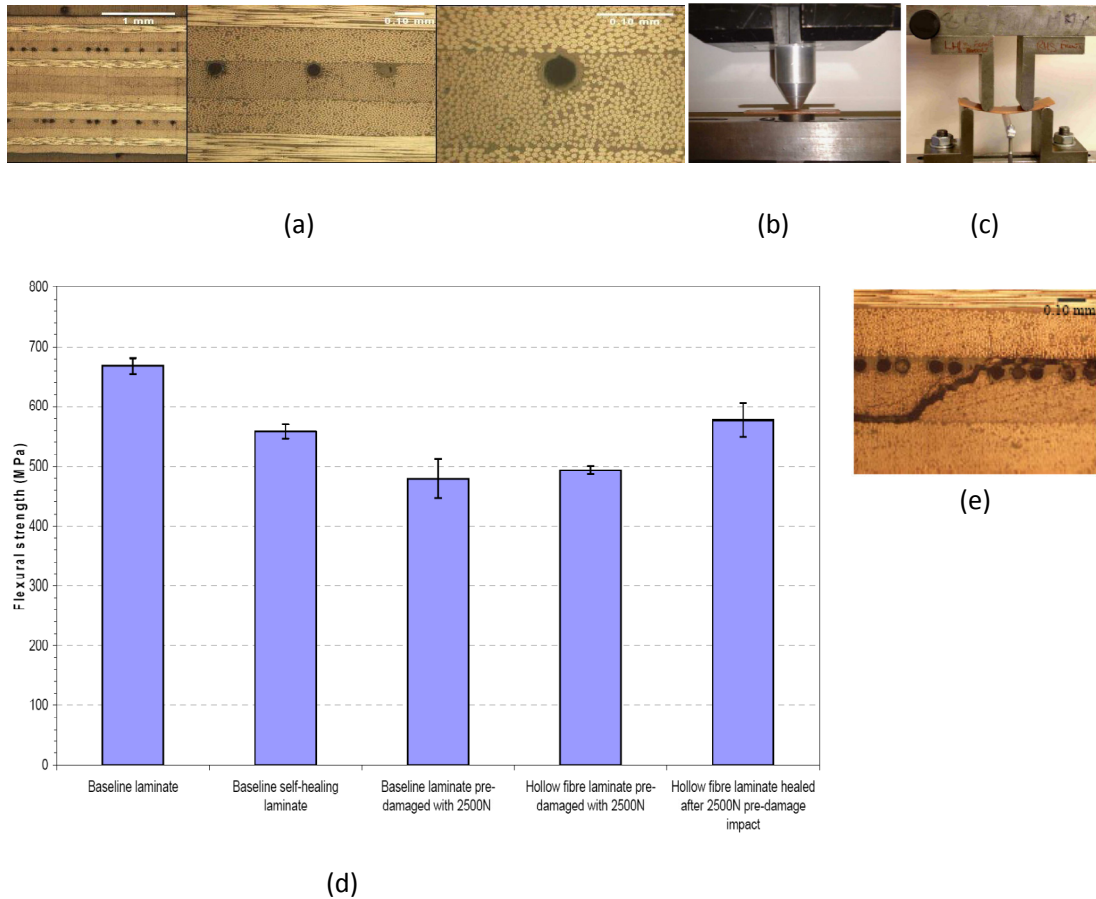
Figure 1.6: SHM using hollow glass fibers: (a) micrograph of hollow glass fibers in laminate composite under increasing magnification; (b) creating initial damage by indentation; (c) 4-point bending test; (d) recorded strength; (e) delamination of SHM using hollow glass fibers. (after Trask *et al.*, 2006b)

In recent years, novel tubular systems have been studied by various researchers. In the new systems, also known as vascular systems, micro tubes/fibers are connected to form 2D or 3D networks. Most of researches on vascular systems are conceptual studies focusing on strategies to design and fabricate self-healing network. William et al. (2008 a,b) studied strategies to design vascular systems by investigating the effect of channel

diameter on fluid flow, network failure modes such as channel blockage and large-scale leakage from ruptured channels. The authors constructed a hierarchical self-healing 2D network using a two-part epoxy system contained in polyvinyl chloride tubes for composite sandwich panels (Williams et al. 2008c). Effects of choices of channel diameter, network shape and network connectivity on reliability of vascular systems were studied by Bejan and coworkers (Kim et al., 2006; Zhang et al., 2007; Lorente and Bejan, 2009). Aragon et al. (2008) proposed a genetic-based algorithm for designing 3D vascular system. Toohey et al. (2007, 2009) and Hansen et al. (2009) investigated direct-ink writing method to produce 3D vascular self-healing systems for self-healing coating applications. It was claimed that surface cracks in the proposed self-healing coating could be healed repeatedly.

1.2.2.3. Bio-inspired self-healing materials with microcapsulated systems

Bio-inspired self-healing materials using microcapsules were pioneered by White et al. (2001) with the concept as illustrated in Figure 1.7. The healing agent (DCPD - Dicyclopentadiene monomer) is encapsulated into microcapsules and embedded into the structural composite matrix containing the catalyst (Grubbs' catalyst). When a crack propagates across and ruptures the capsule, the healing agent will leak out to the crack plane and alter the shape of the crack tip through polymerizing reaction. This polymerization bonds the crack planes together, stops the crack propagation and recovers loss properties such as fracture toughness. Since polymerization requires contact between the healing agent and Grubbs' catalyst, this poses a serious obstacle since there is

likelihood of the healing agent not meeting the catalyst. This problem has been solved

with the use of a new catalyst-free healing agent, chlorobenzene (Caruso et al., 2007).
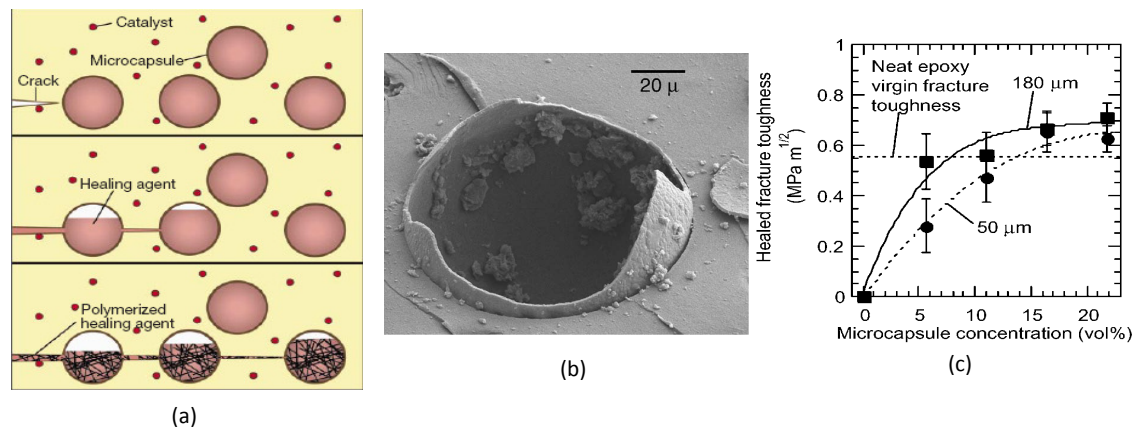
Figure 1.7: Micro-capsule based SHM: (a) diagram of self-healing concept using microcapsules; (b) micrograph of capsules after rupturing; (c) healed fracture toughness vs. microcapsule concentration for different types of capsules (after White *et al.*, 2001).

The microencapsulated approach was first concept-proven by Kessler and White

(2001) in woven composites. Healing efficiency in terms of recovered fracture toughness

was investigated through a double cantilever beam (DCB) test. Two sets of experiments

were conducted. The first involved a so-called reference sample to test the efficiency of

healing by manually injecting the catalyzed healing agent into crack plane of the pure

host material. The second involved a so-called self-activated sample to test if the

embedded catalyst remains active after composite curing by premixing particulate

catalyst into host material and then manually injecting uncatalyzed healing agent into the

crack plane. In both sets of experiments, the specimens were unloaded and clamped after

injection and left to heal for 48 hours before being tested again for their fracture

toughness. The reported highest healing efficiency was 51% to 67%. This low healing efficiency is due to the imperfect interfacial bonding between E-glass fibers (in host composite) and the polymerized product at the healing position.

Kessler et al. (2003) applied this concept in carbon fiber reinforced composite to prevent delamination in host material. The layers where delamination was pre-introduced were filled with 20 wt% microcapsules of average diameter 166 micron and containing DCPD healing agent. After curing for 48 hours at room temperature (27°C), healing efficiency in terms of recovered interlaminar fracture toughness was found to be about 38% but it increased to 80% when cured at 80°C.

Brown et al. (2002) tested the concept of SHM using microcaspsules approach with a homogeneous polymer host matrix (EPON 828 epoxy resin). The tests were carried out using a tapered double cantilever beam (TDCB), which was developed by Mostovoy et al. (1967) to provide crack length-independent measurement of fracture toughness. In situ samples, which are fully integrated systems of this approach containing both microcapsules, catalysts and activated automatically by rupture of microcapsules, were tested. Parametric studies of microcapsule size, microcapsule percentage were also carried out. An average healing efficiency of 85% was reported for system containing 5wt% microcapsules of diameter 180 microns. Moreover, maximum healing efficiency was obtained 10 hour after the fracture occurred. Further investigations carried out by Brown et al. (2004) showed that adding microcapsules containing DCPD increases fracture toughness of material up to 127%. This amount strongly depends on the size and volume fraction of microcapsules. Besides, microcapsules changed the fracture surface

from mirror-like texture (brittle fracture mechanism of neat polymer) to a hackled texture after healing.

Effects of capsule size on performance of self-healing polymers were investigated further by Rule et al. (2007). It is claimed that the minimum size of microcapsules needed for healing performance strongly depends on size of the crack and weight fraction of capsules. For instance, with a crack separation of 3μm, self-healing can be achieved with 1.25 wt% of 251-micron diameter capsules or with 15 wt% of 29-micron diameter capsules. In other words, for the microcapsule system to be effective in self healing, it must satisfy a minimum requirement in terms of the volume of healing agent delivered to the crack but the critical value is still questionable.

Effects of self-healing microcapsule on extending the life of polymer composites under fatigue loading were studied by Brown et al. (2005a, 2005b) and Jones et al. (2007). Successful healing in terms of reducing crack length and retardation of additional crack growth can extend the fatigue life by 89% to 213%. More importantly, if stress amplitude is lower than a threshold, crack growth will be arrested completely. SEM micrograph of the crack tip indicated that the healing was successively achieved through both short and long term effects of the healing process. While short term adhesive effect of healing agent retarded crack growth rate, the long term effect created shielding (solid DCPD wedge) along the crack and/or at crack tip to prevent its propagation. This phenomenon is illustrated in Figure 1.8.
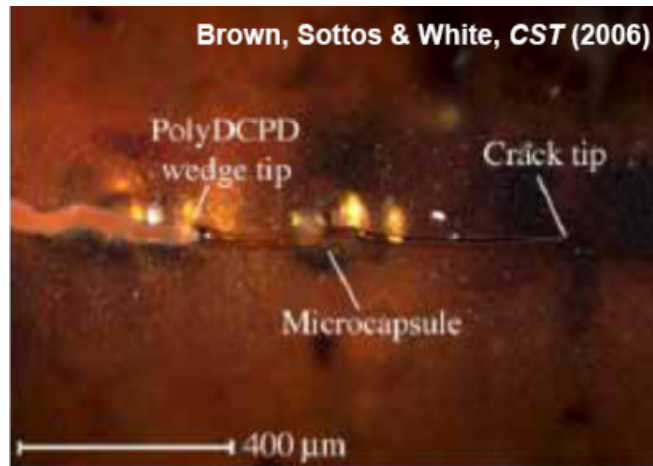
Figure 1.8: Optical micrograph at crack tip of self-healing polymer composite under fatigue loading (after Brown et al., 2006).

Recently, performances of self-healing polymer composite under low-velocity damage impact and torsion fatigue loading are currently investigated. Some early results by Patel et al. (2007, 2009) and Keller et al. (2007) indicated that self healing system not only can recover torsional stiffness significantly but increase the resistance against low-velocity impact. Jin et al. (2011) applied micro-capsule based self-healing approach to create a self-healing adhesive for bonding steel substrates. Experimental results with tapered double cantilever beams showed that the novel adhesive was able to self-heal under both quasi-static fracture and fatigue conditions.

Beside researches on the performance of self healing system using microcapsules in different host materials and under different types of loading, there are other studies on microcapsule manufacturing (Brown et al., 2003), mechanical properties of microcapsule (Keller et al., 2006), and healing agent development (Jones et al., 2006; Mauldin et al., 2006; Caruso et al., 2007, 2008; Wilson et al., 2008, 2009; Blaiszik et al., 2009; Kryger et

al., 2010; McIlroy et al., 2010; Kingsbury et al., 2011). The research in this area made significant progress through the finding of a new catalyst-free healing agent chlorobenzene (Caruso et al., 2007, 2008) making this method cheaper and more practical.

1.2.3. Summary

The above literature review highlights strong potential of both tubular systems and microcapsules systems to create self-healing function in materials. Depending on the specific applications, each system exhibits different advantages and disadvantages. This is because the selection of container in an artificial self-healing system is closely relevant to the critical crack size at which the healing process is desired to perform. An overly large container, compared to the critical crack size, may be too stiff and strong to be ruptured timely. An overly small container may be too weak to prevent a premature rupture of the container, which also means a premature activation of the self-healing system.

For polymers and composites, which are mostly used in medicine, aerospace and especially in electronic industries, the critical crack size is at micro size and hence, the container system should be at micro size, also. Observations from literature show that SHM with tubular system, i.e. using hollow fibers, has the following advantages: high healing efficiency; refillable healing agent; reinforcing containers; possible development to a more advanced network of hollow glass fibers; and fast healing time. However, some obstacles against effective implementation are also obvious. Firstly, because the diameter

of tubes is in the micro-scale, filling the tubes with liquid healing agent is difficult due to large surface tension. Secondly, in self-healing systems using 2-part epoxies, there is high probability that two components of the epoxy do not interact and mix together and hence do not meet the minimum volume/weight ratio to activate the healing process. Thirdly, the hollow glass tubes may create initial weak planes at the matrix-container interfaces if they are stiffer than the host material. These weak planes may initiate or attract cracks and cause delamination as can be seen in Figure 1.6e. Fourthly, the total weight of the new composite may increase due to the presence of the healing system; as such, fibre system is only adopted for applications involving impact loading. To overcome this last limitation, micro-vascular system for SHM are currently being investigated (Williams et al., 2007, 2008 a, b, c; Toohey et al., 2007, 2009; Wu et al., 2007; Huang et al., 2007; Aragon et al., 2008; Lorente and Bejan, 2009 and Hansen et al., 2009). However, the first three limitations of glass fibers system are still present in micro-vascular system.

The literature review also points out the strong potential of SHM using microcapsules approach in polymer composites. Besides recovering the fracture toughness from damage, the fatigue life of the material may be extended as microcrack propagation are retarded or arrested. The recent researches also show that this approach is suitable for components under low-velocity loading and torsional fatigue loading. Compared to the approach using glass fibers, the microcapsules approach has the following advantages:

(a) Manufacturing process of SHM using micro-encapsulated healing agent is easier than that of hollow glass fiber containing healing agent.

(b) Microcapsules can be distributed uniformly in host polymer.

(c) The self weight of the overall composite will not be much affected since density of microcapsule is about 1000kg/m^3, close to the density of the polymer matrix (1160 kg/m^3).

(d) The nearly perfect bonding between capsule and host polymer means that initial crack planes are unlikely to be introduced into the system by the self-healing system.

(e) Lastly, since the microcapsule is soft compared to the host material, it can attract propagating cracks which helps the self healing system to function effectively.

However, embedding microcapsule into host material, if substantial, will reduce the initial stiffness and strength of the composite element. Therefore, optimization to achieve best healing performance while keeping the stiffness and strength is within acceptable range is necessary. Nevertheless, SHM using microcapsules exhibits elegant promise for brittle polymer matrix composites.

Although microcapsule system shows a better capability to create self-healing polymer composites, tubular system is a more approachable method for applications in civil engineering area. In civil engineering applications using mortar and concrete, because of the size of the structures, the high density and the brittleness in tensile of the material, micro cracks appear everywhere in the structure even under the structure's self-weight load. In those cases, healing microcracks is neither important nor possible. Instead, healing macro cracks, which point out mature damages in the structure, is more desirable. As a result, macro size should be the size of the container in self-healing units.

In addition, tubular system has the following advantages compared to the microcapsule system:

(a) Casting concrete will create more harmful factors to self-healing units such as heat generated and aggregate impact that will easily rupture microcapsule healing units. Finding a protection method to protect hollow tubes from the above harmful factors is much easier than finding that to protect the microcapsules.

(b) Since the zone of critical damage in a structural member in civil engineering is large and predictable, there is no need for the uniform distribution ability of the microcapsule system. Instead, the concentration of healing agent offered by tubular system is more appreciated.

(c) The amount of healing agent that can be contained in a microcapsule is too limited compared to the critical crack size. This means a large number of microcapsules are required to heal one macro crack; resulting much higher cost compared to tubular system, where the macro hollow tubes are commercialized product with much lower cost.

With the above reason, it is not surprising that there is very limited research on self-healing cementitious materials using microcapsule approach. Although the most of the experiments conducted in literature used mortar and at small scale (less than 500mm length), good literature results, in terms of recovered strength and stiffness, demonstrate a prospective outcome when this approach is implemented in practical concrete applications.

1.3.   OBJECTIVES AND SCOPES

The literature review has demonstrated that SHM using microcapsule has great potential to achieve self-healing concept for polymer composites. The outcomes are based on experiments and researchers are still trying to find ways to enhance its performance and utilize its full potential. To achieve, this purpose, it may be optimal to perform theoretical and numerical studies of these self-healing systems to complement the experimental effort.

For microcapsule based SHM, detailed understanding of the underlying mechanisms and ability to predict its macro-behaviour as the parameter changes will provide the necessary information to speed up the development of this new class of smart material. For instance, with a candidate chemical to be used as a healing agent, it is possible to perform numerical simulation to estimate the maximum healing efficiency in terms of recovered fracture toughness and the extent of material stiffness that has to be sacrificed to attain the desired healing efficiency. Limited experiments using the simulated optimal solution can be performed as verification before decisions on the suitability of using the above chemical as healing agent of SHM can be concluded.

The literature also reveals effort of researchers in extending the idea of self-healing concept in concrete. Actually, this extension is very important to make full use the idea of artificial self-healing as concrete is a widely used material in the world. Additionally, as a building material, concrete is closely related to human and any collapse of concrete structures may cause significant effect to human society.

It is shown that researchers are still finding ways to implement the self-healing concept in concrete based on some preliminary studies with two variable parameters, namely, (i) type of host materials, e.g. mortar or ECC; (ii) type of healing agent, e.g. alkali-silica solution, methyl methacrylate, superglue cyanoacrylates, polyurethane or bacteria. These two parameters are important and are the basic components to create self-healing functionality in materials. Until now, most of experiments are still proof-of-concept test using lab-scale beam elements made of mortar or mortar composites. In fact, an implementation self-healing concept on concrete elements at structural scale is more difficult because of some issues such as aggregate impact on the healing units and effect of heat generation. Also, most of experiments in literature investigated self-healing with beam element, where hollow tubes are embedded horizontally to make use of gravity and capillary force. The plausibility of implementation of self-healing concept in other structural elements such as column and slab is still questionable.

Based on the above review, the objectives of the current study are (i) to develop a numerical model to predict the macro behaviour of self-healing composites and (ii) to extend the idea of self-healing to concrete materials.

Multiscale modeling approach will be used to develop the numerical model for self-healing composites. In this approach, a microscale model is constructed to capture constitutive mechanical properties of the composites. These properties will be fed as input into another model at macro scale to model the structural behavior of self-healing composite. The application of self-healing concept in concrete will be focused on concrete structural members at real-scale. Three basic structural elements will be investigated namely, beam, column and slab.

The scope of this study includes the following:

- *Linear and non-linear behavior of Representative Volume Element (RVE)*. RVE concept has been used intensively in recent years to predict material properties of composites. While the effectiveness of this approach in predicting linear properties of composites is strongly confirmed, the use of RVE in predicting non-linear behavior of quasi-brittle composites is still questionable. Moreover, the use of single-particle RVE (SP-RVE) and multiple-particles RVE in literature is still unclear and depends much on the author. This step is to provide a unique point of view on RVE concept in both linear and non-linear mechanical behavior.

- *Numerical model of material properties of microcapsule based SHM*. Based on the result of the previous step, a numerical model will be developed to capture basic material properties of microcapsule based SHM. In this step, the healing effect will be simulated.

- *Macro-level simulations to capture structural behavior of self-healing beam using SHM.* A macro-level model which uses effective homogenized element will be proposed to model structural behavior of a self-healing beam made of SHM. This model use the material properties of SHM predicted in step 2 as inputs. The output will be the behavior of the self-healing beam before and after being healed. Simulation with self-healing beam using tubular system will also be conducted to compare healing effects offered by the two systems.

- *Application in civil engineering*. This step provides some first investigations on implementation of self-healing function in reinforced concrete. Firstly, preliminary

studies will be carried on to select appropriate healing agent and container. Next, an effective method to protect self-healing units during casting process will be investigated. Finally, the protected self-healing units will be embedded in three basic structural reinforced concrete members namely, beam, column and slab to find the healing efficiency.

1.4.   ORGANIZATION OF THESIS

Approaches to model mechanicals behaviors of composites are presented in Chapter 2. Theoretical, classic numerical and multiscale approaches, both theoretical modeling and numerical modeling using RVE concept, are reviewed. Advantages and limits of RVE approach are also presented.

The plausibility of RVE approach for modeling the mechanical properties of quasi-brittle materials is investigated in detail in Chapter 3. A unique answer on the use of SP-RVE and MP-RVE as well as on the existence of RVE for non-linear modeling quasi-brittle materials will be discussed and verified with published experimental data.

Chapter 4 is to develop a numerical model to simulate self-healing materials with capsulated system. Remarks on published experiments are first discussed to provide some basic information of the model. Then, numerical simulation of material properties of microcapsule based SHM using RVE concept is performed. These material properties will be used at macro level to simulate structural behavior of SHM.

The implementation of self-healing concept for civil engineering applications via developing self-healing concrete is examined in Chapter 6. The selection of components of self-healing unit comprising of healing agent, container and protection method is studied. Then, self-healing units are embedded inside reinforced concrete structural members to create self-healing members. Experiment set up and result of the implementation is presented and discussed.

Finally, in Chapter 6, the conclusions and contributions of the study are presented while the recommendations for future works are outlined.

CHAPTER 2:

APPROACHES TO MODEL MECHANICAL BEHAVIORS OF COMPOSITES

2.1.   INTRODUCTION

Predicting mechanical behaviors of composites is a multi-scale modeling problem, in which different length scale models and links between these models are need to be taken into account. With the help of more and more powerful computational tools, this problem has been being studied intensively over the past few decades. Basically, there are two strategies to tackle the multi-scale modeling problem, namely, hierarchical approach and homogenization approach.

2.2.   HIERARCHICAL APPROACH

2.2.1. Overall strategy

In hierarchical approach, the mechanical response of composites is simultaneously modeled at different length scale levels, typically at the micro and macro scale for conventional composites as shown in Figure 2.1. Element deformations are computed at the larger scale, which will then serve as applied kinematic boundary

conditions at the smaller length scale. Stress and strain are consequently computed in the smaller length scale and the averaged values are sent back to the larger length scale.
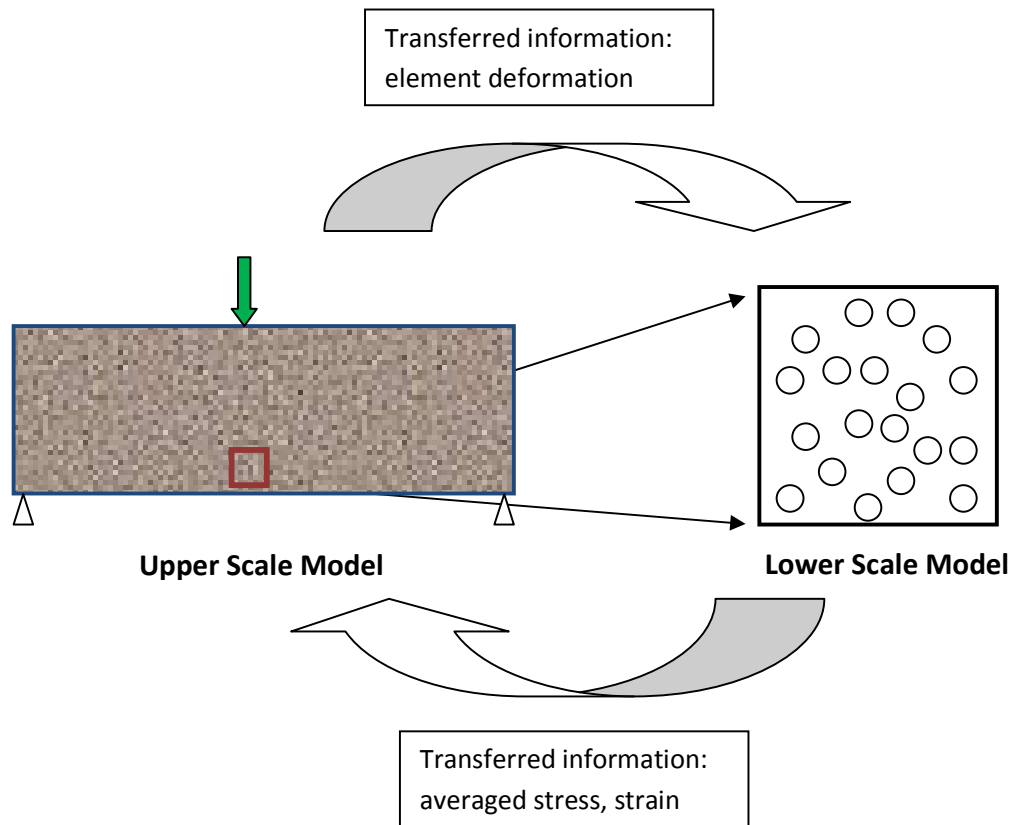
Figure 2.1: Schematic diagram of hierarchical approach
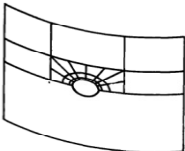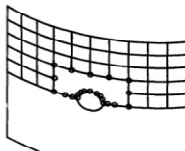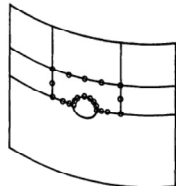
2.2.2. Computational models

2.2.2.1. Global – local analysis models

In 1971, Mote C.D. (1971) pioneered the work of multi-scale modeling using hierarchical approach by introducing the global – local analysis concept which is a combination of the Rayleigh – Ritz method for global estimation and the finite element

method for local solution. This technique was then developed by different researchers (Delves and Hall, 1979; Delves and Philips, 1980; Noor, 1986) with the generalized concept as follows: The global solution is obtained by using either classical variational methods, e.g. Rayleigh – Ritz, weighted residual approaches, or using discretized continuum methods, e.g. finite element method or boundary element method, or a combination of both variational approach and discretized continuum method such as global element method. Meanwhile, local analysis at critical positions is obtained by using either conventional discretized continuum methods or special discretized continuum methods. Table 2.1 is an example of global – local analysis used by Noor (1986) to analyze the post buckling response of a laminated composite cylindrical panel with a central circular hole.

Table 2.1: Global – local analysis approach for a laminated composite panel (Noor, 1986)

Global analysis	Global elements	Conventional finite element	Global elements
Local analysis	Conventional (or special) finite elements	Boundary elements	Boundary elements
Illustration			

The idea of using finite element methods for both global and local analysis was investigated in detail by Wilkins (1983) and Hirai et al. (1985). In their study, the global

solution is obtained using coarse mesh and local stress distribution at a specific position is obtained using a refined model, in which the nodal displacements obtained from the global model is applied as kinematic boundary conditions. Inter-element compatibility can be achieved by using transition elements or super-elements.

2.2.2.2. Superposition based models

To improve the accuracy of the solution when overlaying a local mesh on a global mesh, superposition based models have been developed with the main idea of decomposing the overall solution into global and local effects. The method is volunteered by Belytschko et al. (1990) by superimposing the spectral approximation of the classical finite element solution over a spectral patch that is placed over a critical region in the global model. The method is further developed by Fish (1992) into the more commonly known s-version of the finite element method. The idea of s-version is to improve the quality of the solution for a local region that is incorporated in a global problem by superimposing additional meshes of higher order element at the local region. The author then applied this approach to analyze the deformation of laminated composite shells (Fish et al., 1996, 1997a).

Takano et al. (1999) derived a finite element formulation for the case where the meshes in global and local regions are generated individually and the boundary of elements in each level does not need to coincide as shown in Figure 2.2a. Afterwards, the authors used the technique to develop a four-level hierarchical finite element model in three-dimensional analysis to simulate damage propagation in woven and knitted fabric composite materials and structures as illustrated in Figure 2.2b.
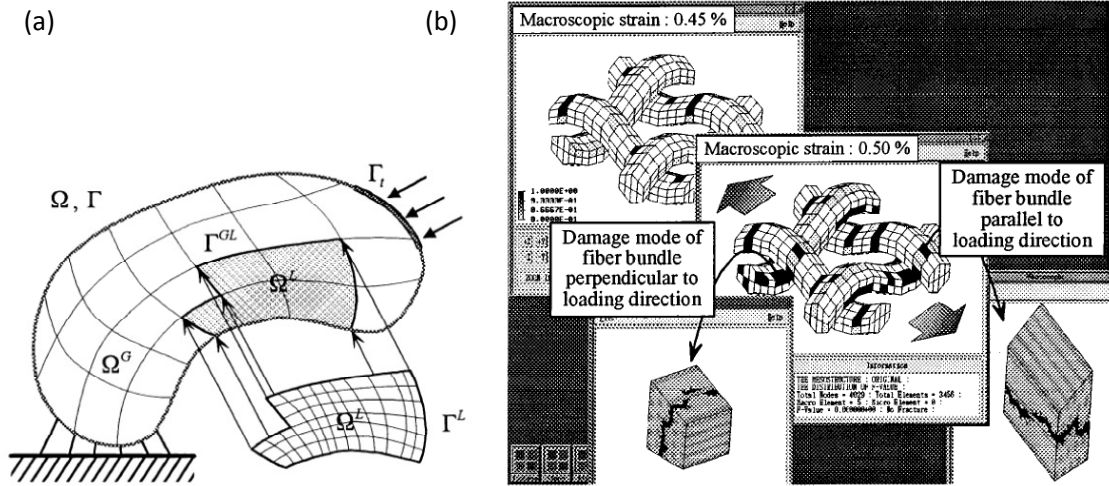
Figure 2.2: Hierarchical modeling of woven composites (Takano et al., 1999):
(a) global-local FEM technique; (b) multi-scale modelling

2.2.2.3. Macro-micro hierarchical model

Mishnaevsky et al. (1999) used macro-micro hierarchical model to simulate a compact tension test on WC/Co hard metal containing 16% volume fraction of cobalt. In this model, a realistic micro-structure just in front of the crack tip was reconstructed based on SEM images and embedded in a macro-model of the compact tension specimen as shown in Figure 2.3a. While damage propagation was simulated in the micro-modeling domain (Figure 2.3b-e) using element elimination technique, material in macro-modeling domain was simulated as linear elastic (Figure 2.3a) using effective properties of the composite. To generate the finite element mesh for the real micro-structure in front of the crack tip easily, multiphase finite element technique was used. The idea of the multiphase finite element technique is that material properties of different material phases in a

composite are assigned at each integration point of the element. As a result, geometrical boundaries of the generated elements do not necessarily coincide with the geometrical boundaries of each material phase that is observed in the SEM images. The approach was also used by Mishnaevsky et al. (2003a,b) to simulate crack initiation and growth in tool steels.
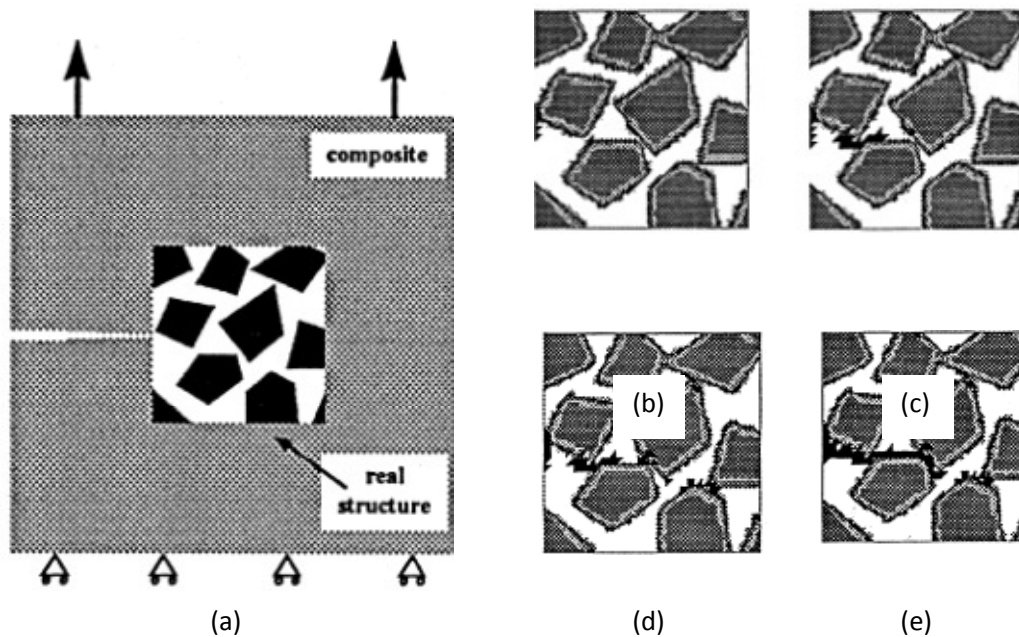
Figure 2.3: Hierarchical modeling of WC/Co hard metal (Mishnaevsky et al., 1999): (a) model; (b) damage initiation and propagation

2.2.2.4. Domain decomposition model

Zohdi et al., (2001) developed the domain decomposition model in which a large scale micro-mechanical model is decomposed into a set of subdomains. All subdomains are non-overlapping and decoupled by applying a kinematically admissible solution on the global model to form separately solvable problems. Then, all subdomains are solved

with the exact inhomogeneity contained within their boundaries. Finally, the solution for the global problem is found by assembling results obtained from the subdomains.

2.2.2.5. Multi-level finite element models

Feyel and Chaboche (2000) proposed the multi-level finite element model (FE^2), in which the micro behavior of the composites is taken into account at the level of Gauss point of elements in the macro-model. The algorithm consists of four steps. Firstly, macro analysis is performed to find the macro-field strain. Next, localization process based on quasi-periodic theory is applied to find the microscopic strain. This microscopic strain is used as an input to a representative volume element model to find the output of microscopic stress. Finally, the microscopic stress field is homogenized to become the macroscopic stress. The homogenized macroscopic stress is assigned as the output at the Gauss points of elements in the macro-model.

Gitman (2006) extended the Feyel and Chaboche model to the Coupled-Volume approach, in which the macro-level and the micro/meso-level sizes are uniquely linked. The size link is established based on the number of integration points in an element in the macro-model. If there is only one integration point per macro-level element, then the macro-level element equals the meso/micro-level representative volume element. In the case that more than one integration point is used for the macro-level elements, the tributary region belonging to each integration point equals to the size of the representative volume element. The main idea of the coupled-volume approach is illustrated in Figure 2.4 for the application of uni-directional tensile test of a composite bar.
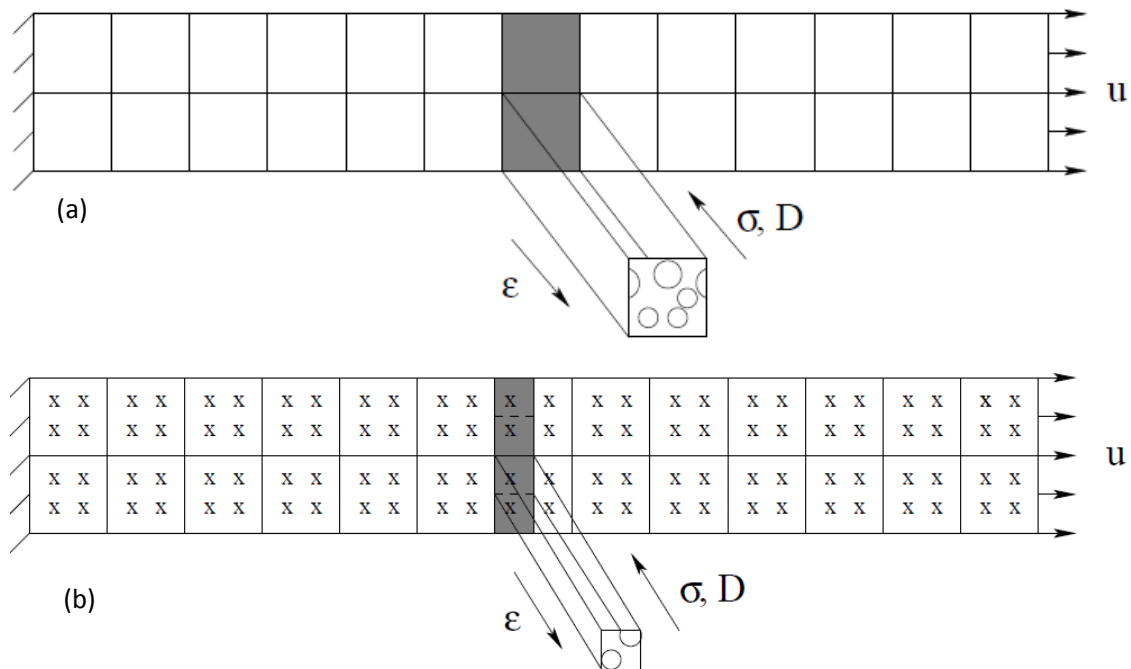
Figure 2.4: Schematic of Coupled-Volume approach (Gitman, 2006): (a) macro element with single interaction point; (b) macro element multiple integration points.

2.2.2.6. Concurrent multi-level model

Ghosh and Raghavan (2004a,b, 2005, 2007) have developed the concurrent multi-level hierarchical model to simulate linear behavior and damage development in composites. As can be seen in Figure 2.5, a concurrent multi-level model consists of three levels namely, (i) level-0: pure macroscopic computational level; (ii) level-1: intermediate computational subdomain; (iii) level-2: pure microscopic computational level. Level-1 acts as a link to switch from level-0 and level-2 and hence, consists of both micro and macro analysis.
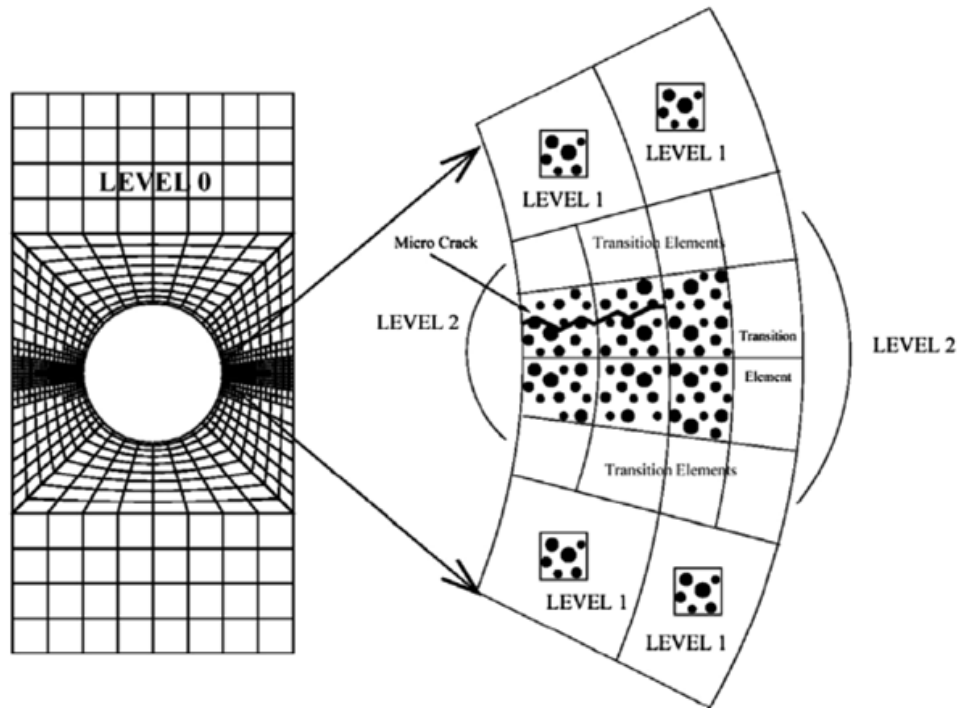
Figure 2.5: Schematic of concurrent multi-level model (Ghosh and Raghavan, 2007)

The macroscopic analysis at level-1 is performed using continuum damage mechanics to evaluate macroscopic variables, such as field displacement, which will then be fed into the level-1 microscopic analysis with periodic boundary condition to determine the effective average stress and strain fields to be relayed back to the level-1 macroscopic analysis. Adaptive mesh refinement strategy is applied to macroscopic models in both level-0 and level-1 to improve the convergence of the solution through mesh enhancement.

In level-2, microscopic analysis is performed without any periodic boundary condition being applied. The level-2 elements are constructed using the exact local micro-structure, which is normally found by analyzing SEM photographs. Similar to the microscopic computation performed at level-1, Voronoi cell FEM is applied to perform

the level-2 analysis. To facilitate a smooth transition between elements in level-2 and in the other two levels, a layer of transition elements is introduced.

2.2.3. Advantages and disadvantages of hierarchical approach

The first, and foremost, advantage of hierarchical approach is in its ability to simulate the relationship between an evolving damage at micro-scale and the overall behavior of a structure at macro-scale. This advantage is a result of the overall strategy of the approach: the lower scale and upper scale models are simulated and solved simultaneously. In this approach, different scale models interact intensively via the transfer of data, such as stress, strain and deformation. Hence, interaction or coupling between different scale levels is the critical problem that has to be solved to assure accuracy of the models. This is both a challenge and an advantage of the approach. It is a challenge because of the difficulties, in both theoretical and experimental efforts, to link the classical theories at the different length scales such as continuum mechanics, micromechanics and molecular mechanics. However, modeling such links between different scale models is also the advantage of hierarchical approach compared to homogenization approach, in which all local effects are smeared out in the macro-model.

The greatest disadvantage of hierarchical approach is in the complication of the model, which comes with a very high computational cost. Because of this disadvantage, most researches using the hierarchical approach are limited to the analysis of simple composite structures (Zohdi, 2001; Ghosh and Raghavan, 2005).

2.3.   HOMOGENIZATION APPROACH

2.3.1. Overall strategy

The basic concept of the homogenization approach is to find an equivalent homogeneous medium that can represent, in terms of mechanical behavior, a real heterogeneous material, shown in Figure 2.6.

Real macro problem

Homoaenization

Microscopic analysis

Real heterogeneous material   **Equivalent homogeneous medium**

Effective propertie

Modeling macro problem
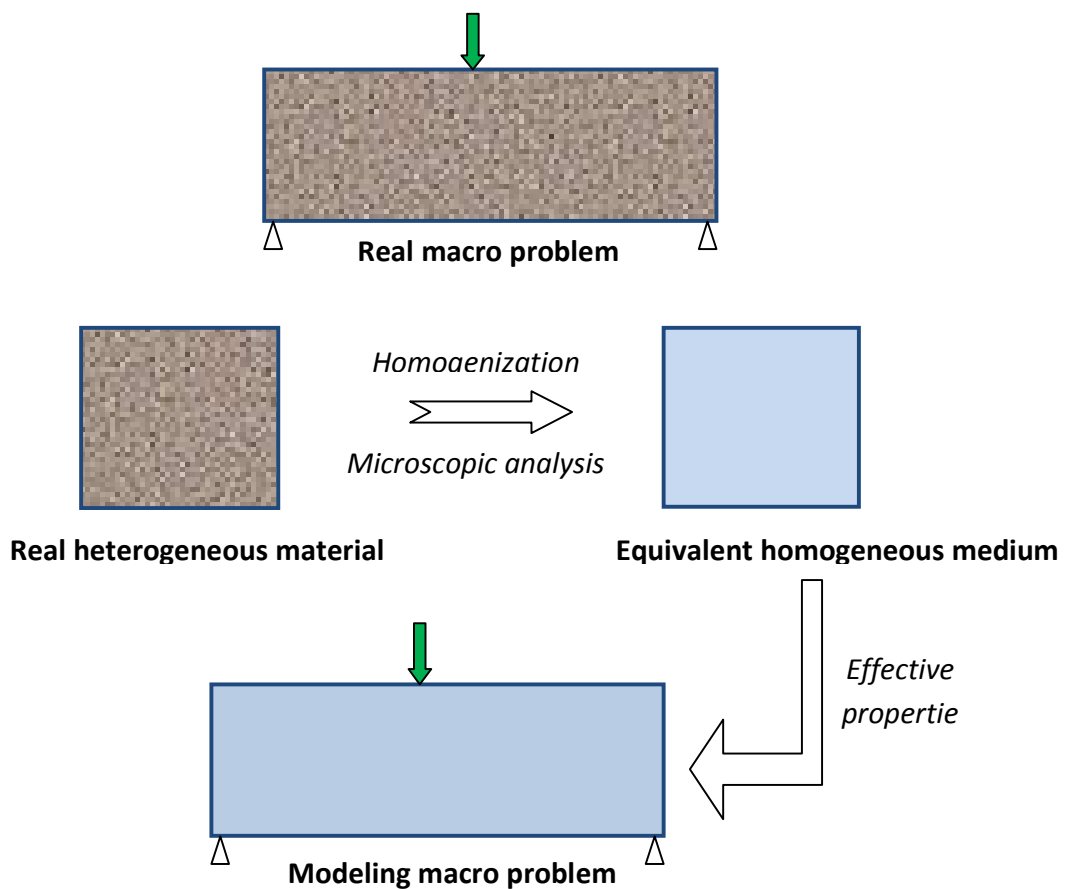
Figure 2.6: Schematic diagram of homogenization approach

Material properties of the equivalent homogeneous medium are called effective properties and these properties are often determined on the basis of the analysis of the micro-structure that takes into account the heterogeneity of the material. Finding the

effective properties of the heterogeneous materials, which is also called the homogenization process, is the first and most important step in this approach because it determines the accuracy of the whole model and, moreover, it reveals the underlying micro-mechanisms of the macro behavior such as particle clustering and interface debonding failure. Once the effective properties of the composite are found, it is fed into the macro-model as material inputs to simulate the overall behavior of a composite structure using either classical theories, e.g. beam theory and shell theory, or direct numerical approaches, e.g. finite element method or boundary element method.

Since the analysis of the equivalent homogeneous medium is identical to the conventional structural analysis of homogeneous material, the review in this Section is purely on homogenization techniques to find effective properties of composite materials.

2.3.2. Theoretical models

2.3.2.1. Voigt's and Reuss' models

Predicting the effective properties of composite materials, which is in fact the homogenization of a heterogeneous material, is one of the classical but very important problems in solid mechanics. This problem has been examined decades ago; starting from the use of Voigt's model (Voigt, 1889), in which the strain was assumed to be uniform throughout the material, and Reuss' model (Reuss, 1929) in which all phases in the material carry the same stress. Based on these assumptions, the effective Young's modulus of a heterogeneous material is predicted using Equation (2.1a), for Voigt's model, or Equation (2.1b), for Reuss's model.

$$E_{eff} = E_m(1-f) + E_i f \tag{2.1a}$$

$$E_{eff} = \frac{E_i E_m}{E_m(1-f) + E_i f} \tag{2.1b}$$

where E is Young's modulus and f is the volume fraction of particles and subscripts *eff*, *m,* and *i* denote composite, matrix and inclusion respectively.

Although neither Voigt's model nor Reuss' model are correct due to the non-equilibrium or incompatibility at the boundaries of the phases, Hill (Hill, 1964) showed that they form the upper bound (Voigt's estimation) and lower bound (Reuss' estimation) of the true effective elastic modulus of composites.

2.3.2.2. Dilute distribution model

Eshelby (Eshelby, 1957) considered stress and strain fields in an infinite medium containing an ellipsoidal inclusion that is changing its shape and size (undergoes a "transformation"). He has shown that a uniform strain ε_t, called as unconstrained strain or eigenstrain, acting on an homogeneous ellipsoidal inclusion will result in a uniform strain state ε_c, called as constrained strain, on the inclusion if it is embedded in an infinite linear elastic medium. The relationship between ε_t and ε_c can be expressed by:

$$\varepsilon_c = S\varepsilon_t \tag{2.2}$$

where S is the Eshelby tensor and depends on the material properties of the matrix and shape of the inclusion.

Based on the above result, Eshelby (Eshelby, 1957) proposed an equivalent inclusion model or dilute distribution (DD) model for the case when a small volume fraction of inclusion is used to reinforce a host material. In that case, the effective bulk modulus and shear modulus of the composite can be predicted as following:

$$K_{eff} = K_m \left[1 - f \left(\frac{K_m}{k_m - k_i} - S_1 \right)^{-1} \right] \tag{2.3a}$$

$$G_{eff} = G_m \left[1 - f \left(\frac{G_m}{G_m - G_i} - S_2 \right)^{-1} \right] \tag{2.3b}$$

with

$$S_1 = \frac{3K_m}{3K_m + 4G_m} \tag{2.3c}$$

$$S_2 = \frac{6(K_m + 2G_m)}{5(3K_m + 4G_m)} \tag{2.3d}$$

where K and G are the bulk and shear modulus respectively, f is the volume fraction of particles and subscripts eff, m, and i denote composite, matrix and inclusion respectively.

2.3.2.3. Hashin-Strikman bounds (Composite sphere assemblage model)

Following the micromechanics-based pioneering work by Eshelby (Eshelby, 1957), there have been a lot of analytical solutions relating to composites over the last

five decades. In 1962, Hashin and Shtrikman (Hashin and Shtrikman, 1962) have developed the composite sphere assemblage (CSA) model from DD model by limiting the infinite matrix in DD model to a finite region that can be determined with volume fraction of the inclusions, as shown in Figure 2.7.
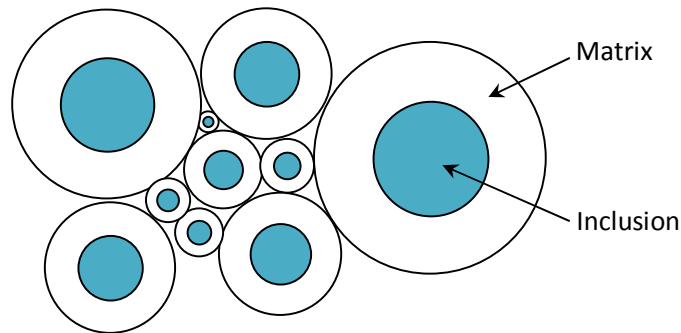
Figure 2.7: Schematic diagram of CSA model

The authors have derived the variational principle for nonhomogeneous linear elasticity and used this principle to derive the analytical solution for the CSA model that provides bounds for effective elastic properties of heterogeneous materials as expressed in Equations (2.4a, b, c, d). The predicted value band formed by Hashin – Shtrikman bound is much narrower than that formed by Reuss and Voigt bounds. As a result, Hashin - Shtrikman bound is the most widely used estimation to provide a rough estimate for effective modulus of composites.

$$K_{-} = K_m + \cfrac{f}{\cfrac{1}{K_i - K_m} + \cfrac{3(1-f)}{3K_m + 4G_m}} \qquad (2.4a)$$

$$K_{+} = K_i + \cfrac{1 - f}{\cfrac{1}{K_m - K_i} + \cfrac{3f}{3K_i + 4G_i}} \tag{2.4b}$$

$$G_{-} = G_m + \cfrac{f}{\cfrac{1}{G_i - G_m} + \cfrac{6(K_m + 2G_m)(1 - f)}{5G_m(3K_m + 4G_m)}} \tag{2.4c}$$

$$G_{+} = G_i + \cfrac{1 - f}{\cfrac{1}{G_m - G_i} + \cfrac{6(K_i + 2G_i)f}{5G_i(3K_i + 4G_i)}} \tag{2.4d}$$

where the subscripts – and + denote lower and upper bounds, respectively.

2.3.2.4. Self-consistent and generalized self-consistent models

Beside the Hashin-Strikman bounds, two other widely used models developed from DD model are self-consistent (SC) model and generalized self-consistent (GSC) model. The self-consistent (SC) model (Hill, 1965; Budiansky, 1965; Hori and Nemat-Nasser, 1993) solves the similar problem of Eshelby but for high concentration of inclusion by substituting the infinite medium matrix properties by effective properties of the whole composite which has to be determined from iterations. Using SC model, the effective linear properties of composite were found by solving the set of Equations (2.5)

$$\frac{K_{eff}}{K_m} = 1 + f\left(\frac{K_i}{K} - 1\right)\left[1 + \left(\frac{K_i}{K_{eff}} - 1\right)S_1^{eff}\right]^{-1} \tag{2.5a}$$

$$\frac{G_{eff}}{G_m} = 1 + f\left(\frac{G_i}{G} - 1\right)\left[1 + \left(\frac{G_i}{G_{eff}} - 1\right)S_2^{eff}\right]^{-1} \tag{2.5b}$$

with

$$S_1^{eff} = \frac{3K_{eff}}{3K_{eff} + 4G_{eff}} \tag{2.5c}$$

$$S_2^{eff} = \frac{6(K_{eff} + 2G_{eff})}{5(3K_{eff} + 4G_{eff})} \tag{2.5d}$$

The generalized self-consistent (GSC) model (Chrsitensen, 1990; Huang and Hu, 1995) is an extension of the SC model where the matrix in the vicinity of the inclusion is simulated as a separate phase, as illustrated in Figure 2.8.
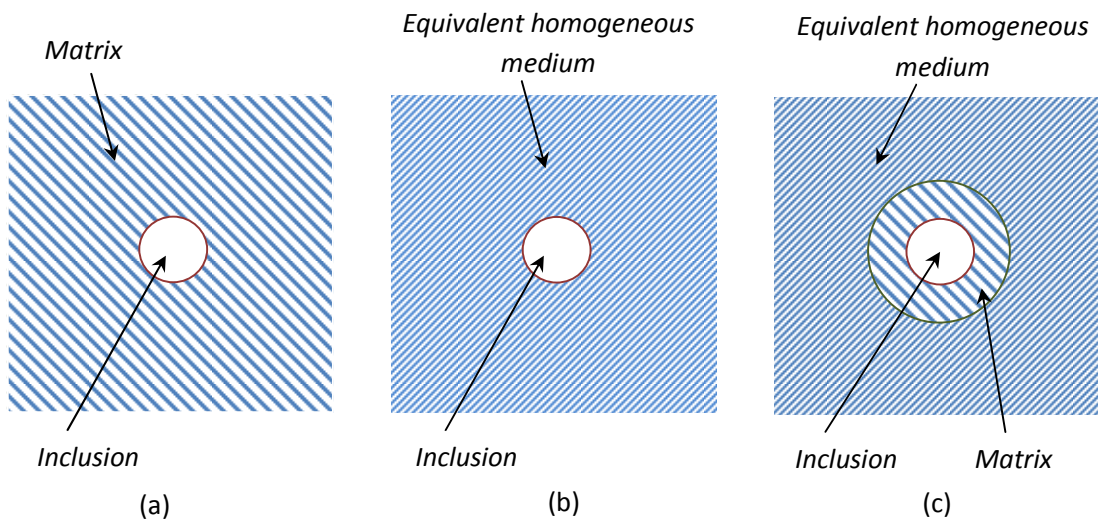
Figure 2.8: Schematic of theoretical models to homogenize composites. (a) DD: inclusion in an infinite matrix; (b) SC: inclusion in an infinite medium that have effective stiffness of the whole composite; and (c) GSC: inclusion surrounded by matrix in an infinite medium that has effective stiffness of the whole composite

The main differences between DD, SC and GSC models lie in the assumed interactions between inclusion and matrix as well as between inclusions themselves. In

the DD model which is more suitable for small volume fraction of inclusions, interactions between inclusions are negligible as they are far apart that the matrix surrounding each inclusion may be considered as an infinite medium. When the number of inclusions is large, interactions between them become more significant and the surrounding matrix is replaced by a material that has the effective properties of the entire composite. The SC model does not pay special attention to the detailed stress and strain in the matrix near the inclusion. This is addressed in the GSC model by embedding an outer layer of matrix surrounding the inclusion. However, the solving for the sets of equations in GSC model is so much complicated compared to other analytical models that GSC is less widely used as other models.

2.3.2.5. Mori-Tanaka model

Another well-known model that uses Eshelby's tensor is Mori-Tanaka (MT) model (Taya and Chou, 1981; Weng, 1984, 1990; Benveniste, 1987), which is similar to the DD model, except that it imposes an additional condition to account for the effect of multiple inclusions by combining the Eshelby's theory with the effective field concept and the condition that, the effective Young's modulus of the composite takes on the value of the Young's modulus of the inclusion when the volume fraction of the inclusion approaches 1. The problem is solved by introducing a strain concentration tensor which relates the strain in the matrix to the strain in the inclusion. Christensen and Lo (1979) and Tan *et al.* (2005) noted that the Mori–Tanaka model shares the same expression for effective bulk modulus with the GSC model. As commented by many authors such as

Bohm (1998) and Mishnaevsky (2007), the prediction of effective bulk modulus and shear modulus for spherical inclusion and aligned fiber reinforcement composites using MT model, as expressed by Equations (2.6a) and (2.6b), is very close to the experimental results. That can explain why the MT model is one of the most widely used models to predict the effective elastic properties of composites.

$$K_{eff} = K_m + \frac{f(K_i - K_m)}{1 + \frac{(1-f)(K_i - K_m)}{K_m + \frac{4}{3}G_m}} \tag{2.6a}$$

$$G_{eff} = G_m + \frac{f(G_i - K_m)}{1 + \frac{(1-f)(G_i - G_m)}{G_m + \frac{G_m(9K_m + 8G_m)}{(6K_m + 2G_m)}}} \tag{2.6b}$$

2.3.3. Numerical approach using RVE concept

All the analytical models reviewed in Section 2.3.2 are developed from Eshelby's solution where they can approximately represent detailed stress and strain fields in the matrix and inclusions by their volume-averaged value. However, such models are limited by the assumptions made in the original Eshelby's equivalent inclusion model, that is, materials are linear elastic and their deformations are small. Furthermore, it is difficult to incorporate damage mechanisms such as interface debonding and matrix/particle cracking. Also, the prediction of post-cracking nonlinear properties of composite materials cannot be accurately handled by this class of model.

With the help of computers, numerical techniques such as FE and discrete element (DE) methods have been used to develop more refined material models for composites. These approaches offer many advantages such as:

(a) Inclusions of arbitrary shapes can be modeled;

(b) Inelastic or time dependent properties can be incorporated to the model easily;

(c) Imperfect bond between inclusion and matrix can be taken into account; and

(d) Composites comprising three or more phases can be considered.

The increased complexity of the problem due to refinements in the material and geometrical details would inevitably escalate the computational cost enormously, especially for heterogenous micro-structure. To overcome this limitation, *the representative volume element (RVE) concept* is commonly adopted (Drugan and Willis, 1996; Sun and Vaidya, 1996; Gusev, 1997; Michel et al., 1999; Gitman et al., 2007; Kim and Lee, 2009; Pelissou et al., 2009).

The first definition of a RVE was stated by Hashin (Hashin, 1963) as follows: "*A RVE is a model of the material to be used to determine the corresponding effective properties for the homogenized macroscopic model. The RVE should be large enough to contain sufficient information about the microstructure in order to be representative; however it should be much smaller than the macroscopic body*". Since then, a number of modified versions on the definition of a RVE have been made by other authors (Hashin, 1983; Drugan and Willis, 1996; van Mier, 1997 and Evasque, 2000). In general, in all definitions of RVE, it is

treated as "super element" that either (i) represent statistically the micro-structure of the composite, or (ii) provide accurate prediction on the macroscopic constitutive response of the composite. Figure 2.9 shows the different types of RVE models built based on either of these two requirements in which the former is exhibited by RVEs under Scheme C while the latter is exhibited by RVEs under Schemes A and B.

In Scheme A, the actual micro-structure is assumed to be equivalent, in terms of mean response, to another micro-structure with uniformly distributed particles. The equivalent micro-structure is, in fact, a periodic structure where the smallest "material period" is a square unit cell with a single particle located at the center of the cell and its edge length equals to the distance between the particles. By applying appropriate periodic boundary conditions so that a unit cell is replicable to the entire material domain, the overall behavior of the equivalent micro-structure can be represented by that of the unit cell, also known as the RVE. The position and size of window can be varied by defining the "material period", thus different types of RVEs can be constructed as illustrated by RVEs A1, A2 and A3 in Figure 2.9. The construction of a RVE under Scheme B is similar to that under Scheme A, except the smallest "material period" is now a unit cell containing two or more randomly dispersed particles. Due to this randomness, multiple realizations with different arrangements of particles are possible. Each of the realization can be analyzed and the results are averaged over all realizations considered, to obtain the mechanical response of the actual composite. In Scheme C, the RVEs are constructed based on images of the actual micro-structure and periodicity is not considered. It should be noted that the volume fraction of particles in RVEs under Schemes A and B are

defined to be the same as that of the real composite, but this is not necessary true for the

case of RVEs under Scheme C.
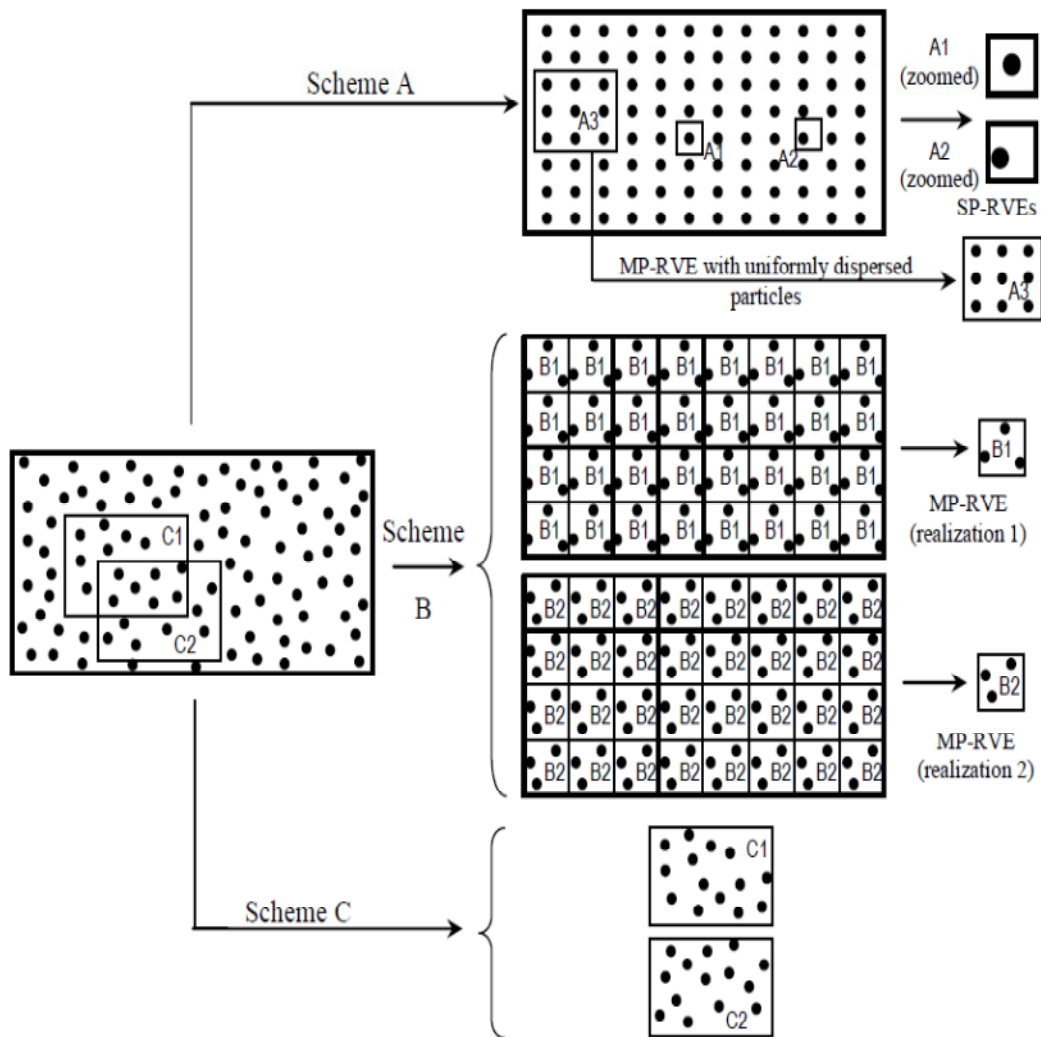
Figure 2.9: Schemes to define RVE: SP-RVE with periodic boundary conditions (Scheme A), MP-RVE with periodic boundary conditions (Scheme B), images from real micro-structure without periodic boundary conditions (Scheme C)

2.3.3.1. Single-particle RVE approach

As shown in Figure 2.9, a SP-RVE can be either symmetric or asymmetric. But, the latter type is rarely used in literature. There are two ways to construct a symmetric SP-RVE namely, (a) embedding a particle at the center of a cylindrical matrix to form a cylindrical cell; or (b) embedding a particle at the center of a cubic matrix to form a cubic cell. Figure 2.10 illustrates both cylindrical and cubic models, in which the 3D cylindrical cell can be simplified to a 2D axisymmetric cell as in the studies of Kuna and Sun (1996) and Sovik (1996). Although the cylindrical cell model can be simplified to save on the computational time, this model is much less popular than the cubic model because the cylindrical cells cannot populate the material space without overlapping.
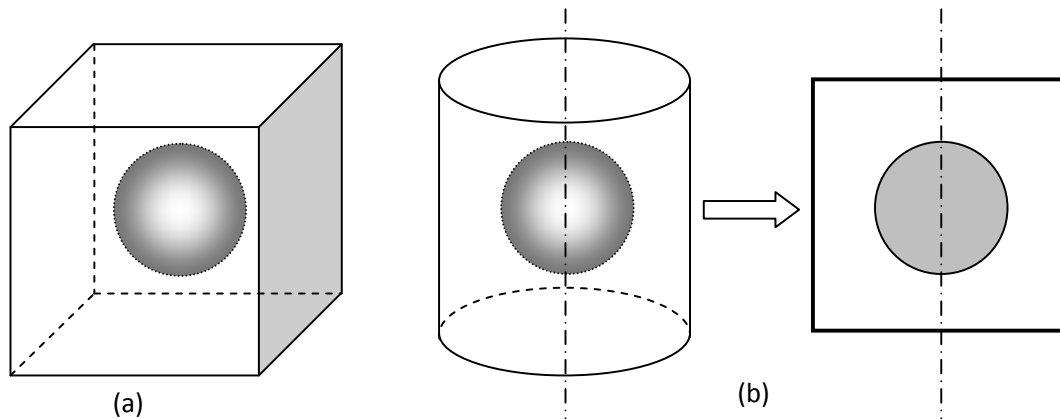
Figure 2.10: SP-RVE models: (a) cubic cell; (b) cylindrical cell and the simplified axisymmetric cell

The SP-RVE approach is commonly used to study the linear elastic behavior of composites. In 1995, Sun and Vaidya (Sun and Vaidya, 1995) adopted this approach for the study of fiber reinforced composites. Chen and Mai (1998) used the SP-RVE

approach to study the elastic properties of rubber reinforced composites. The approach was also applied to study glass, boron and aluminum fiber composites (Xia et al., 2002).

By coupling with micro damage models to account for inclusion failure, inclusion debonding or matrix failure, the SP-RVE approach has been used to analyze the effect of micro-cracks on the overall mechanical behavior of composites. Llorca and colleagues (Llorca et al., 1991) studied the effect of nucleation in the matrix on the deformation of Al/SiC composites using axisymmetric cylindrical cell with reinforcements in spherical, ellipsoidal shapes. Bao (1992) used a three-phase damage SP-RVE model to investigate the effect of particle failure and interfacial bonding on the strength and creep resistance of different composite systems. Michel (1993) used SP-RVE approach to study the effect of particle cracking and debonding on the mechanical behavior of Al/SiC composite and presented the effective stress-strain curves for different particle shapes and for different damage mechanisms. Kuna and Sun (1996, 1997) studied the void growth in ductile materials using both cylindrical and cubic cells. The authors showed that the arrangement of voids strongly affect the failure response. Steglich and Brocks (1997) combined micro-damage models, such as void nucleation, particle cracking and particle-matrix debonding, to analyze the behavior of nodular iron and Al/Al$_3$Ti composite.

2.3.3.2. Multiple-particle RVE approach

Similar to SP-RVE approach, MP-RVE approach is used to study both linear and non-linear behavior of composite materials. Segurado and Llorca (2002) used 3D MP-RVE containing 30 non-overlapping spherical particles to predict elastic properties of

epoxy matrix composites. Three types of particles were investigated in this study including rigid spheres, spherical voids and glass spheres. The simulation results were used to compare and assess the accuracy of analytical models such as Mori-Tanaka model and self-consistent model. Kari et al. (Kari et al., 2007) applied 3D MP-RVE approach to study effect of size of particles on effective linear properties of particulate reinforced composite. Results of the study, in which up to 60% volume fraction of randomly distributed spherical particles was simulated, showed good agreement with analytical models.

Various researchers applied MP-RVE approach to simulate elasto-plastic behavior of composites. Galli et al. (2008) numerically simulated elasto-plastic behavior of metal matrix composites and which agreed well with the experimental data. A comprehensive study on the elasto-plastic behavior of heterogeneous material systems by numerical simulation was conducted by Llorca and colleagues (Segurado et al., 2003; Segurado and Llorca, 2006; Pierard et al., 2007a, b), in which effects of particle size, particle shape and particle clustering on the overall behavior of composites were investigated.

Recently, MP-RVE approach has been extended to study problems involving hyperelastic matrix or reinforcements. Yvonnet and He (Yvonnet and He, 2007) coupled the Mooney-Rivlin and Neo-Hookean material models for matrix modeling and MP-RVE approach to study porous hyperelastic media. Danielsson et al. (2007) developed a numerical tool with MP-RVE concept to model the elasto-viscoplastic deformation of rubber toughened glassy polymers.

For the micro-damage problem in composites, Sluis et al. (1999) applied MP-RVE with uniformly distributed pores to study strain softening in porous polycarbonate plate. Segurado and Llorca (2005) incorporated interfacial zone with cohesive element model to examine the effect of interface decohesion on the mechanical behavior of a composite system comprising of stiff spherical particles embedded in a ductile matrix. The model used 35 spherical particles dispersed in both clustered and non-clustered manner, as shown in Figure 2.11.
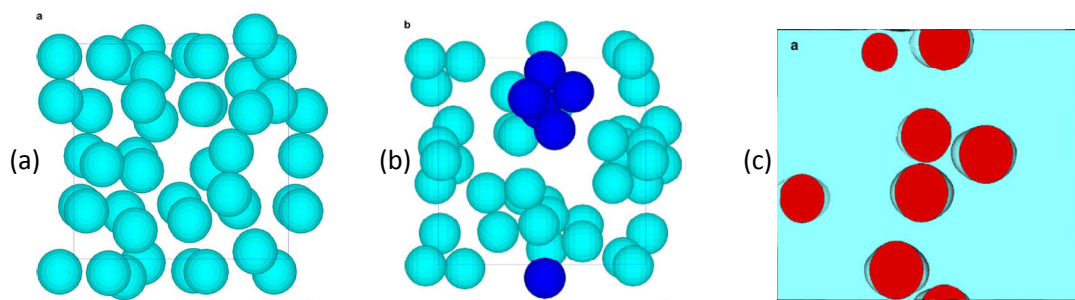
Figure 2.11: Interface decohesion modeling with MP-RVE approach (Segurado and Llorca, 2005): (a) randomly distributed particles; (b) clustered particles; (c) result from simulation.

2.3.3.3. Image based RVE approach

In image based RVE approach, RVEs is constructed based on the statistical analysis of the real micro-structure as illustrated in Scheme C in Figure 2.12. Generally, there are 3 steps in this method. Firstly, digital images of the micro-structure of material are analyzed to define the size of RVEs and to provide geometric conditions of all material phases contained in the RVEs. After that, finite element mesh is generated and material properties are assigned to each element according to the constructed geometric

conditions in step 1. Finally, numerical analysis is carried out to investigate micro-mechanics of the composite. This approach was first proposed by Hollister and colleagues in 1993 (Hollister and Reimer, 1993; Hollister and Kikuchi, 1994) to model porous micro-structure in human bone.

Depending on the geometries of reinforcements, either 2D or 3D image based RVE can be applied. The 2D approach is often used for long fibrous composites while the 3D approach is normally adopted to examine short fibrous composites or particulate composites. Examples of using the 2D image based RVE are studies done by Grufman and Ellyin (2006, 2007), in which damage analysis of fibrous composite was carried out on RVEs constructed based on the actual position and diameter of fibers extracted from micro-graphs of cross-ply laminate. Instances of using 3D image based RVE can be found in researches by Terada et al. (1997) for metal fiber reinforced MMC, and by Takano et al. (2003) for porous ceramics.

Since all micro-graphs are in 2D, construction of a 3D image based RVE will be more complex than the corresponding 2D approach. To overcome the uncoupling between 2D images and 3D analysis, the so-called serial sectioning technique has been developed. Figure 2.12 shows the 4-step procedure to construct a 3D image based RVE namely, (i) section processing; (ii) cross-sectional images; (iii) image processing and (iv) voxel meshing, which has been discussed by Takano et al. (2003).
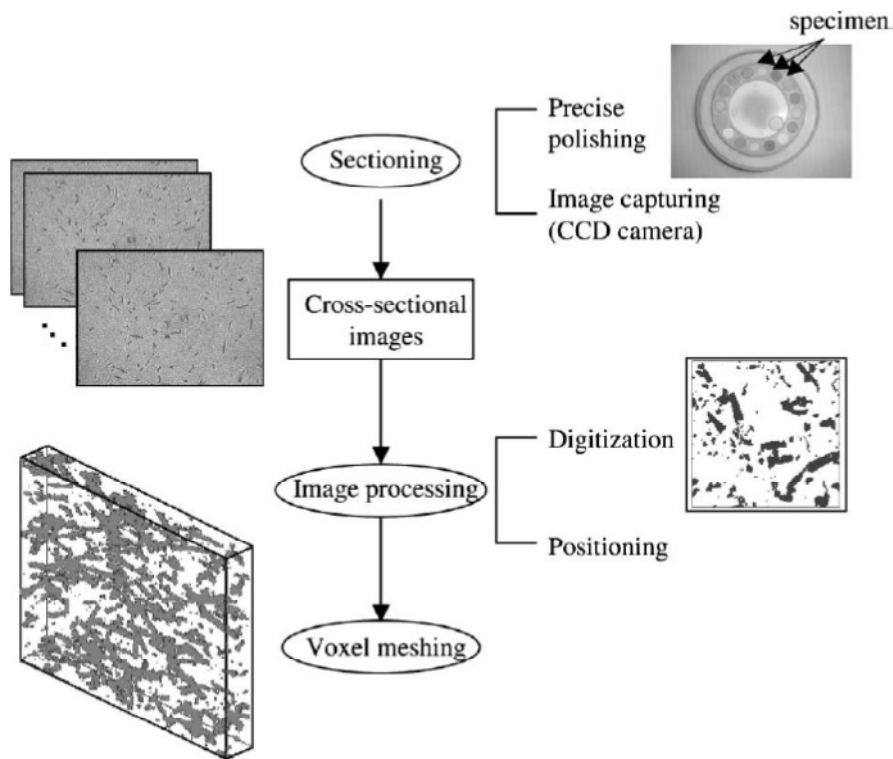
Figure 2.12: 3D image based RVE (Takano et al., 2003)

2.3.4. Remarks on homogenization approach

2.3.4.1. Comparison between analytical models and RVE approach

Analytical models are first attempts made by researchers in homogenization approach. In the beginning, when the interest of research is in the linear elastic behavior of composites and when the computational tools are not developed fast enough to solve complex numerical problems, these analytical models proved to be useful and reliable for the prediction of elastic properties of composite materials. They formed the foundations for micro-mechanics such as Hill condition (Hill, 1964), Eshelby tensor (Eshelby, 1953)

54

and Mori-Tanaka theory (Mori and Tanaka, 1973). However, when the interest of study extends beyond the prediction of linear elastic properties of composites, the limitations of analytical models become more obvious, such as the low accuracy in modeling post-failure behavior; difficulty in incorporating damage models such as interface debonding and particle cracking; and difficulty to use for hyperelastic materials with large deformation.

With the rise of computer speed, numerical models using RVE approach becomes more popular, especially for damage and large deformation analysis. Among the three approaches, the image based RVE method, which adopt the concept of RVE based on the equivalency in the geometrical statistics of micro-structure, is the least effective approach due to its requirements on section preparation and image processing. Also, the computational cost of image based RVE approach is much higher than those of SP-RVE and MP-RVE because the size of the image based RVE is relatively large to statistically represent the micro-structure of the composites. Compared to MP-RVE approach, SP-RVE approach is simpler with the focus of modeling in the matrix-particle interactions only. Hence, the computational cost of SP-RVE approach is much cheaper than that of MP-RVE approach, but SP-RVE approach is only valid when inter-particle interactions are negligible, such as composites with low volume fraction and non clustering inclusions. On the other hand, MP-RVE approach sacrifices computational effort by fully taking into account interactions between all material phases in the composites to achieve a more realistic model with more accurate prediction.

2.3.4.2. Advantages and limitations of homogenization approach

The advantage of the homogenization approach, compared to hierarchical approach, is at much lower computational cost as mechanical response of composites are modeled sequentially at different scales, which reduces the size of the problem, and laws of scaling is not fully modeled. In recent years, efforts have been made to explore the law of scaling that allow to use a variable found at a lower scale model to an upper scale model with a modification function but still not successful yet. As a result, at the moment, only size independent properties, such as elastic modulus and fracture energy, are able to be carried from the lower scale model to the upper scale model. Also, since the law of scaling is not understood in depth yet, only single mode of damage, mostly mode 1, is considered in homogenization approach.

2.4.   SUMMARY

This chapter reviews on two commonly used multi-scale models namely, hierarchical approach and homogenization approach. These two approaches come from two different points of view and hence, serve different purposes. The hierarchical approach is adopted by researchers who are studying the structured response but are also interested in the micro-mechanical behavior in the lower length scales. As a result, lower level models are tied tightly to the macro-model in the hierarchical approach.

The homogenization approach, on the other hand, is favored by researchers focusing on effects of constituents and micro-structural arrangement on material properties. Indeed, this approach shares the same concept with the conventional approach

of using experiment at lab-scale to find out mechanical properties of materials. The only difference is that in homogenization approach, experiments are conducted numerically at micro-scale.

Among models in homogenization approach, SP-RVE and MP-RVE are two most widely used approaches in homogenization approach. The MP-RVE approach is more accurate with both particle-matrix and particle-particle interactions fully modeled. Nevertheless, the high computational cost makes this approach less favored for problems with negligible inter-particle contact such as composites with low volume fraction of particles. For those cases, SP-RVE is a better candidate due to the validity of sacrificing the inter-particle interactions for a much lower computational cost.

In the light of the above reviews with the consideration of making use of published experimental data, homogenization approach using SP-RVE and MP-RVE approaches is chosen for the study involving micro-capsule based self-healing materials.

THIS PAGE IS INTENTIONALLY LEFT BLANK

CHAPTER 3:

RVE APPROACH FOR MODELING THE MECHANICAL PROPERTIES OF QUASI-BRITTLE COMPOSITES

3.1.   INTRODUCTION

As reviewed in Chapter 2, RVE concept is the most widely used to date, among homogenization methods to model the mechanical responses, both linear and non-linear, of heterogeneous materials. It is notable that the term RVE approach used in this Chapter onwards refers to single-particle and multiple-particle RVE approaches instead of image-based RVE approach, which is not used in this project for its limitations.

For the prediction of linear elastic properties, good agreement with the experimental data was achieved even at high volume fraction of inclusions indicating that multi-particle RVE is a powerful approach for developing micromechanics-based models of material behaviour. Although, the computational time for the repeated runs can be enormous that the choice between single-particle RVE approach and multiple-particle RVE approach should depend on the specific application. Unfortunately, in many researches, the use of SP-RVE or MP-RVE approaches is based on personal judgment of the researchers leading to an unwell-defined criterion for the approach to use. For example, Chen and Mai (Chen and Mai, 1998) used SP-RVE approach for rubber

reinforced composite with volume fraction of rubber particles varying from a low 0.209%

to a high 26.18%; Sun and Vaidya (Sun and Vaidya, 1996) and Xia et al. (Xia et al.,

2003) used SP-RVE approach for fiber composite with very high volume fraction of fiber

from 47% to 60%. On the other hand, Segurado et al. (Segurado et al., 2003) and Kari et

al. (Kari et al., 2007) applied the MP-RVE approach in their studies for volume fraction

of inclusion ranging from 10% to 60%.

In the past 15 years, the RVE concept has been extended to predict the pre-

ultimate non-linear response of composites, as in studies by Gonzalez et al. (Gonzalez et

al., 2004), Segurado and Llorca (Segurado and Llorca, 2005), Pierard et al. (Pierard et al.,

2007a, b), Muliana and Kim (Muliana and Kim, 2007), and Sharma and Socrate (Sharma

and Socrate, 2009). In these studies, the effective properties were predicted either from

multiple realizations of a fixed size RVE with random particles placement (Gonzalez et

al., 2004; Segurado and Llorca, 2005; Sharma and Socrate, 2009), or from single

realization of a fixed size RVE with assumed regular arrangement of the particles

(Muliana and Kim, 2007). Although the numerical results agree with the experimental

data in terms of stress-strain behaviour up to the ultimate strength, these studies did not

consider the effect of the RVE size on the strain hardening behaviour. In addition, the

number of realizations may be too few in some cases to provide reliable representation

for the results obtained.

The effect of size of a multi-particle RVE on the nonlinear behavior of

composites for a fixed volume fraction of inclusions was examined in depth by Gitman et

al. (Gitman et al., 2007), and Pelissou et al. (Pelissou et al., 2009). While the ability of

RVE to predict the linear elastic and strain hardening phenomena of composites has been

60

established in their studies, the use of the RVE concept to predict the strain softening

phenomenon of quasi-brittle composites remains debatable. Gitman et al. (Gitman et al.,

2007) questioned the existence of such a RVE based on their results which showed size

dependence on the strain softening behavior. On the contrary, Pelissou et al. (Pelissou et

al., 2009) carried out studies on quasibrittle composites, comprising of perfectly brittle

inclusions embedded in a strain hardening metal matrix using multiple sizes of RVE and

concluded that the predicted stress-strain diagram of a composite does not depend on the

size of the RVE, provided that the number of realizations considered is sufficient.

The reviews show that there is no consensus on the use of SP-RVE or MP-RVE

approaches, and the existence of RVE for quasibrittle material is still unresolved. Hence,

there is a rise of the two key questions for RVE approach:

(i) What are the advantages and disadvantages of single-particle and multi-particle

RVEs, and under what circumstances should they be applied?

(ii) Is there any size effect in the effective stress-strain curve predicted using RVE

concept? What is the reason for the differing views on the size effect in the effective

stress-strain curve of RVEs in the literature? Is there a size-independent damage

parameter which can be predicted with the RVE approach that can be applied to quasi-

brittle composites?

These 2 questions are addressed in this Chapter via the simulation of the material

properties of porous epoxy, which were found experimentally by El-Hadek and Tippur

(El-Hadek and Tippur, 2002). The porous epoxy is used since this system is similar to the

micro-capsule based self healing material in the sense that both systems comprise of a
very soft phase surrounded by a quasi-brittle medium.

The organization of this Chapter is as follows: Section 3.2 presents the published
experimental data and the numerical set up in which the periodic boundary conditions of
a RVE are explained. Simulated results for linear and non-linear behavior of a RVE are
shown in Section 3.3 and form the basis for answering the above two questions.
Comparisons between the predictions obtained from RVE approaches and theoretical
models are also presented in this Section. Section 3.4 shows the consistency of the RVE
concept in terms of fracture energy, which will be used as an alternative measurement in
damage analysis. The summary is given in Section 3.5.

3.2.   EXPERIMENTAL DATA AND NUMERICAL SET UP

3.2.1. Experimental data

El-Hadek and Tippur (El-Hadek and Tippur, 2002) carried out experimental tests
to determine the mechanical properties of two-phase composites which comprises
randomly distributed spherical pores in epoxy matrix. The voids, which are considered as
a material phase with all mechanical properties having zero magnitudes, were introduced
into the matrix by dispersing micro-balloons with an average diameter of 60 µm. The
mechanical properties of the composite with volume fraction of voids f varying from 5%
to 15% were obtained experimentally and shown in Table 3.1. This range of f seems to
have little effect on the Poisson's ratio where an average value of 0.35 was reported for
both pure and porous epoxies.

Table 3.1: Mechanical properties of porous epoxy

Volume fraction of voids f (%)	Young's modulus (GPa)	Tensile strength (MPa)	Fracture toughness (MPa.m$^{1/2}$)
0	3.08	53.0	1.20
5	2.63	46.8	1.10
10	2.38	42.5	0.98
15	2.17	39.8	0.95
20	1.94	36.1	0.89

3.2.2. Numerical set up

3.2.2.1. RVE generation

Both SP-RVE and MP-RVE approaches are adopted in this study to simulate the mechanical behavior of the above porous epoxy using a commercial finite element package ABAQUS version 6.7.2 with user subroutines. Three-dimensional simulations are carried out. The relationship between volume fraction of inclusions (or voids), size of a cubic RVE and diameter of the spherical inclusions is given by:

$$f = \frac{n.V_{inc}}{V} = \frac{n.\frac{4}{3}\pi\frac{D^3}{8}}{a^3} \tag{3.1}$$

where n is number of inclusions (or voids) in the RVE; V is the volume of the RVE; V_{inc} is the volume of each inclusion; a is the edge length of the RVE and D is the diameter of inclusion, which is taken as 60 µm, corresponding to that in the experiment by El-Hadek and Tippur (El-Hadek and Tippur, 2002).

For the SP-RVE approach where $n = 1$, the size of the RVEs will change depending on the volume fraction of inclusions assumed. Two types of SP-RVE with

different configuration for the inclusion are considered; SP-RVE type A contains one

inclusion at the center of the RVE and the other, denoted as SP-RVE type B, which has

the inclusion randomly placed within the RVE. In the latter, if the inclusion is intersected

by the RVE edges for 2D or surfaces for 3D representation, the segment of the inclusion

that falls outside the RVE domain will appear in the opposite edge or surface. For SP-

RVE type A, one realization is needed as the position of the inclusion is fixed while three

realizations are considered for SP-RVE type B due to the random position of the

inclusion.

For specific volume fraction of inclusions and a given fixed inclusion diameter,

the size of the SP-RVE is determined using Equation (3.1) with $n = 1$, while the size of

the MP-RVE can be correspondingly varied depending on the number of inclusions

considered for the RVE. To study the effect of size of RVE, three different sizes of the

RVEs are considered at each volume fraction of inclusion, namely, a = 250μm, 300μm,

and 350μm, and labeled as MP-RVE types C, D and E respectively. At each of the four

volume fraction of inclusions considered in this study, nine realizations are generated for

each RVE size, namely f = 5%, 10%, 15% and 20% as shown in Table 3.1. A larger

number of realizations are being considered to account for the greater variability in the

position of the inclusions in a larger RVE domain. The number of inclusions is calculated

using Equation (3.1), where f, D and a are known parameters, and the positions of

inclusions are also randomly generated based on equal likelihood of inclusions appearing

anywhere in the RVE domain subjected to the constraint that the inclusion do not

intersect each other. Typical realizations of generated sets are depicted in Figure 3.1.
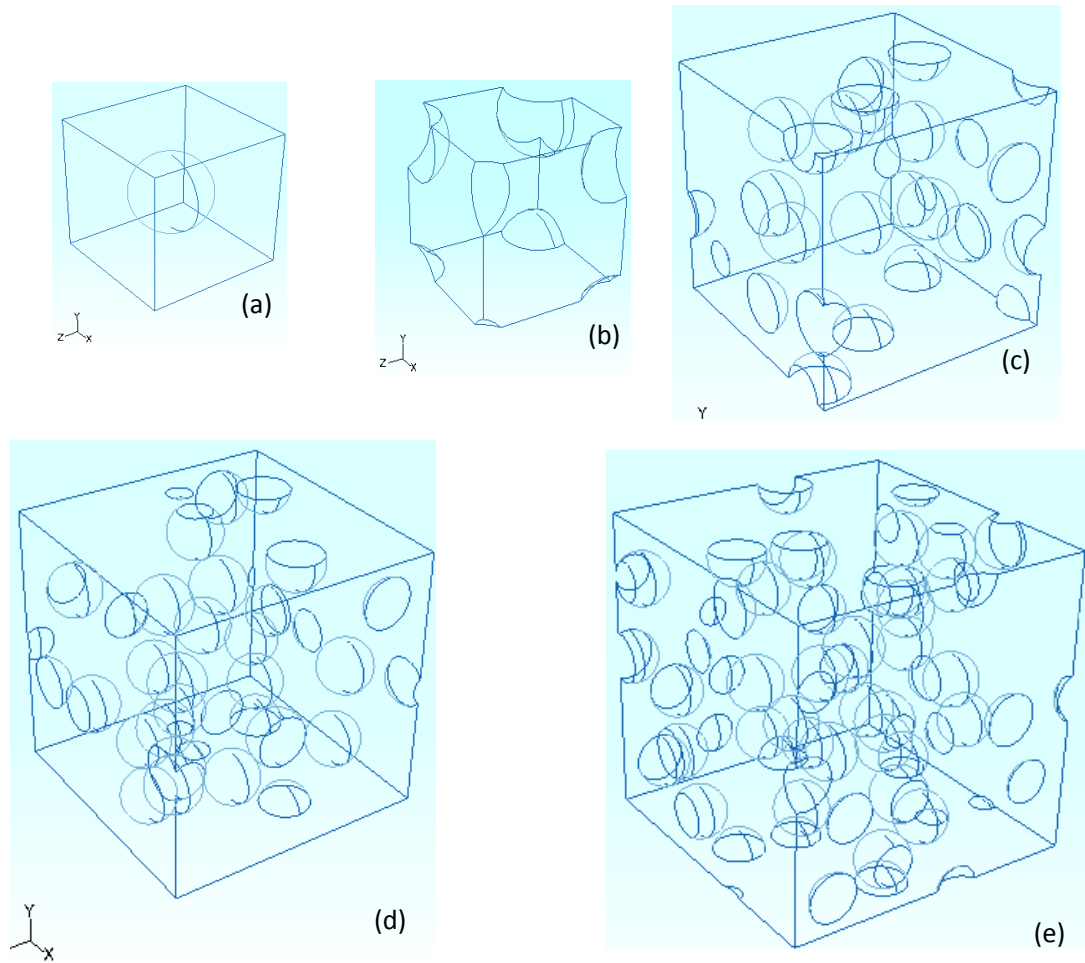
Figure 3.1: Typical RVEs at volume fraction f = 5%. (a) SP-RVE type A; (b) SP-RVE type B; (c) MP-RVE type C with a = 250µm; (d) MP-RVE type D with a = 300µm; (e) MP-RVE type E with a = 350 µm.

3.2.2.2. Periodicities of a RVE

As a RVE is a replica unit cell that is representative of the actual composite, The periodicity of these repeating cells must be satisfied, requiring the compatibility of the deformation, stresses and strains on opposite surfaces for the 3D (or opposite edges for 2D) model of a RVE. Figure 3.2a illustrates the repeatability of a 2D RVE under pure shear load. To enforce compatibility, two periodic conditions must be applied on a RVE,

namely, the *periodic material condition* and *periodic boundary condition*. The term periodicity of material include the case where the inclusions are cut at the cell border with the removed portions re-appearing on the opposite surface of the RVE to maintain periodicity as demonstrated in Figure 3.2b. In other words, the inclusion is able to penetrate through the sample borders.
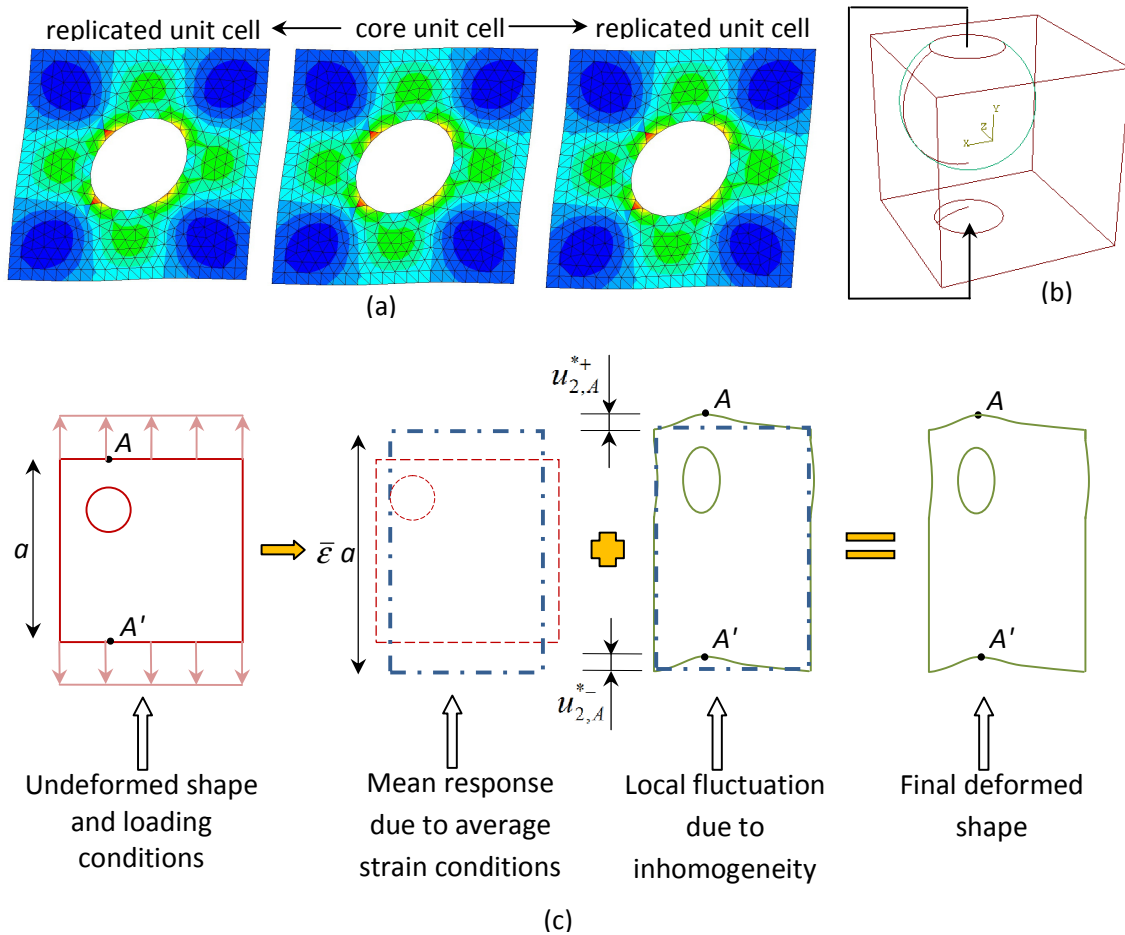
Figure 3.2: Periodicities of RVE: (a) repeatability of a 2D RVE; (b) periodic material condition of a 3D RVE; (c) major concept of periodic boundary conditions for RVE

The idea of periodic boundary conditions, depicted in Figure 3.2c, is to decompose the final deformation into the mean response and the local fluctuation due to inhomogeneity. Mathematically, the periodic boundary conditions of RVE was expressed by Suquet (Suquet, 1983) using tensor notation as

$$u_i = \bar{\varepsilon}_{ik} x_k + u_i^* \qquad \text{with } i, k = 1, 2, 3 \tag{3.2}$$

where u_i are displacement components of a node on the boundary faces; $\bar{\varepsilon}_{ik}$ are the average strains; x_k are the coordinates of the node; u_i^*, which is known as the local fluctuation due to inhomogeneity, is the periodic part of u_i.

The displacements of an arbitrary node u_i^+ on one boundary surface and of its complementary node u_i^- on the opposite surface are:

$$u_i^+ = \bar{\varepsilon}_{ik} x_k^+ + u_i^{*+} \tag{3.2a}$$

$$u_i^- = \bar{\varepsilon}_{ik} x_k^- + u_i^{*-} \tag{3.2b}$$

Because of periodic boundary conditions:

$$u_i^{*+} = u_i^{*-} \tag{3.3}$$

Hence,

$$u_i^+ - u_i^- = \bar{\varepsilon}_{ik} (x_k^+ - x_k^-) = \bar{\varepsilon}_{ik} a = const. \tag{3.4}$$

Equation (3.4) is introduced in the numerical model to enforce periodic boundary condition for the RVE.

3.2.2.3. Material constitutive law

The smeared crack concept (Bazant and Oh, 1983; Guzina et al., 1995) is used in the analysis, with the input parameters being the material properties of the matrix which include Young's modulus, E_m, Poisson's ratio, v_m, tensile strength, $\sigma_{f,m}$, and fracture energy, $G_{f,m}$. Values of these inputs, except for $G_{f,m}$, are given in row 1 of Table 3.1 corresponding to $f = 0\%$. For simplicity, the constitutive law of the epoxy is approximated by a bi-linear stress-displacement curve as shown in Figure 3.3, assuming that damage is dominated by tensile response only; in the figure w and w_0 represent the crack opening displacement and maximum crack opening displacement respectively.
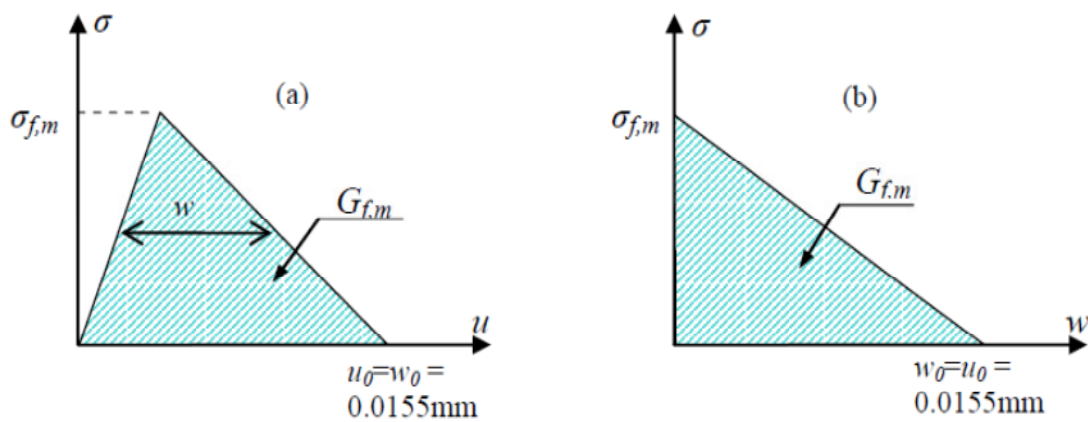
Figure 3.3: Constitutive law for epoxy expressed in terms of stress versus: (a) displacement; (b) crack opening displacement.

The stress-displacement (instead of the stress-strain) constitutive relation is used to reduce mesh size-dependence (Crisfield, 1986). The fracture energy, which is the area under the stress-displacement curve in Figure 3.3, is simply estimated from fracture

toughness K_{IC} under plane strain condition in the experiment (Bazant and Planas, 1998)

as:

$$G_f = \frac{(1-\nu^2)K_{IC}^2}{E} = \frac{(1-0.35^2)1.2^2}{3075} = 4.109x10^{-4}\,\text{MPa.m} \qquad (3.5)$$

The term fracture energy, G_f, is defined here as the energy required to create a unit area

of crack (Bazant, 1998). This term differs from that used by Pelissou et al. (Pelisou et al.,

2009), which carries the meaning of energy dissipated by a unit volume of material.

A full description of a smeared crack model requires three parameters, namely

strength, fracture energy and the shape of the softening curve. In the current study, the

simple bi-linear stress-displacement curve, first proposed by Hillerborg et al. (Hillerborg

et al., 1976), is chosen because there is no experimental data on the actual softening

behavior of the epoxy. In addition, the focus in the current simulations is on the strength

and the fracture energy of the porous epoxy, rather than to compare the detailed softening

curve of this material.

3.2.2.4. Loading condition and other numerical issues

All the RVEs are discretized using 4-node tetrahedral elements with reasonably

fine mesh, typically an average of 800 000 elements are used for RVEs of size a = 350

μm, to maintain accuracy of stresses obtained. The RVEs are subjected to displacement-

controlled uniform traction on two opposite faces. Whilst the specimens used in the

experiment by El-Hadek and Tippur (El-Hadek and Tippur, 2002) has an existing single

notch, the fracture energy measured corresponds to the propagation of a single crack and

the RVE approach can only be valid if the crack localizes into a single crack plane. This

is automatically true for the case of SP-RVEs where the critical plane is well-defined. For

MP-RVEs, there is more than one likely surface for the cracks to form due to the random

location of the inclusions but the number of cracks that can form remains singular as the

cracks localizes as soon as it is formed when under tensile action.

From the load-displacement response of the RVE, the average stress is computed

based on the cross sectional area, a x a, while the average strain is the ratio of the applied

displacement over the edge length, a, of the RVE. From the average stress and strain, the

effective Young's modulus of the composite is estimated. Finally, the effective fracture

energy, $G_{f,eff}$, which is the area under the average stress – displacement curve of the RVE,

is converted to the effective fracture toughness, $K_{IC,eff}$, using Equation (3.5).

3.3.   HOMOGENIZED STRESS-STRAIN CURVE OF RVE

3.3.1. Prediction of elastic response

3.3.1.1. Results from numerical simulations using RVE approach

Table 3.2 compares the elastic properties of porous epoxy based on the

predictions from RVE models with the experimental test results (El-Hadek and Tippur,

2002). The latter reported a single value of Poisson's ratio of 0.35 for all volume

fractions of voids with a variation of ±0.01 (presumably the precision of the experiment).

The results from the RVE models show that there is a slight decrease in Poisson's ratio

with an increase in the volume fraction of voids, from 0.350 for f = 0% to 0.336 for f =

20% in the case of MP-RVE type E. This trend also agrees well with the findings by
Segurado and Llorca (Segurado and Llorca, 2002) for spherical particle reinforced
composites.

Table 3.2: Prediction of elastic properties of porous epoxy using RVE approach

Properties	Vol% of voids	SP-RVE		MP-RVE			Reported results
		Type A	Type B	Type C	Type D	Type E	
Poisson's ratio	0	0.350	0.350	0.350	0.350	0.350	0.35±0.01
	5	0.344	0.341	0.343	0.345	0.345	
	10	0.336	0.334	0.341	0.339	0.341	
	15	0.327	0.324	0.336	0.335	0.338	
	20	0.322	0.320	0.334	0.336	0.336	
Effective Young's modulus (GPa)	0	3.08	3.08	3.08	3.08	3.08	3.08
	5	2.80 (+6.5%)	2.81 (+6.8%)	2.80 (+6.5%)	2.80 (+6.5%)	2.79 (+6.1%)	2.63
	10	2.56 (+7.4%)	2.56 (+7.6%)	2.55 (+7.1%)	2.54 (+6.7%)	2.52 (+5.9%)	2.38
	15	2.34 (+7.8%)	2.34 (+7.8%)	2.32 (+6.9%)	2.30 (+6.0%)	2.27 (+4.6%)	2.17
	20	2.15 (+10.8%)	2.15 (+10.8%)	2.08 (+7.2%)	2.07 (+6.7%)	2.05 (+5.7%)	1.94

numbers in parenthesis denote the % error as compared to experimental values

The Young's moduli predicted from the RVE models are presented in Table 3.2
and the numbers in parenthesis denote the percentage error in prediction as compared to
the experimental values. The two types of SP-RVE in this study are identical in the
physical sense as they can be obtained by placing the same size window at different
positions on a domain with uniformly distributed inclusions. Therefore, the material
properties predicted from SP-RVE types A and B should be the same as shown in Table
3.2. The accuracy of SP-RVE does not depend on the number of realizations generated,
but depends only on the volume fraction of inclusion f.

The predictions from the RVE models correctly follow the trend of diminishing

Young's modulus with increase in the volume fraction of voids as shown in Figure 3.4,

with the most accurate prediction from MP-RVE type E which has the largest domain

amongst the MP-RVEs, whilst the least accurate prediction are from the SP-RVE models

where the prediction error increases with volume fraction of inclusion. However for the

MP-RVE models, the error is relatively constant, ranging from 5 to 7%, indicating the

necessity to take the randomness in particle placement into account, especially at high

volume fraction of voids.
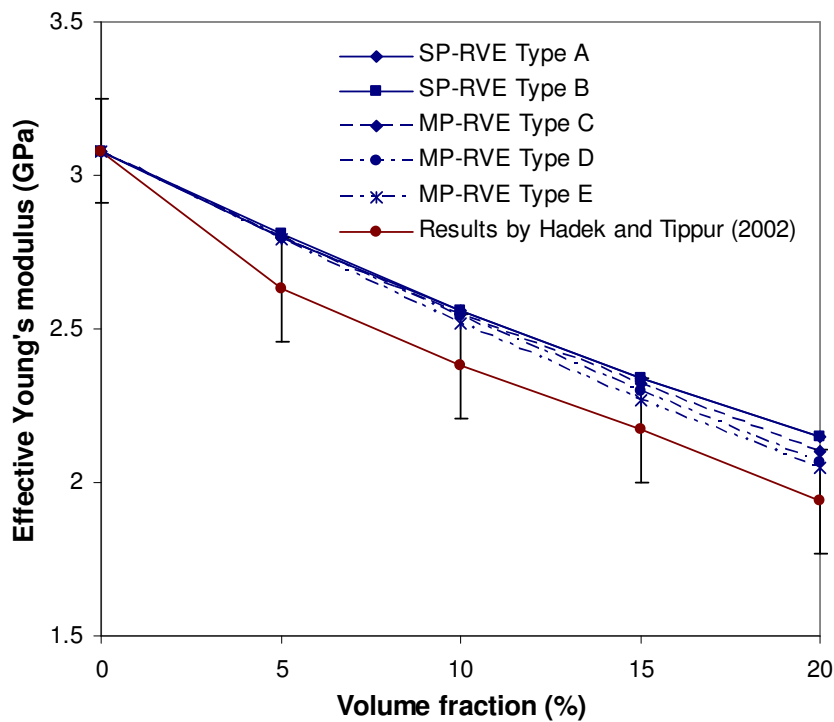
Figure 3.4: Effective Young's modulus obtained from RVE approaches and experiments

The higher discrepancy at higher f for SP-RVE model is due to the fact that a

single inclusion is enclosed by the surrounding matrix in a RVE and the full interaction

with neighbouring inclusions are not included. The prescribed periodic boundary

conditions do account for part of the influence of the surrounding inclusions by enforcing

compatibility, as shown in Figure 3.5.
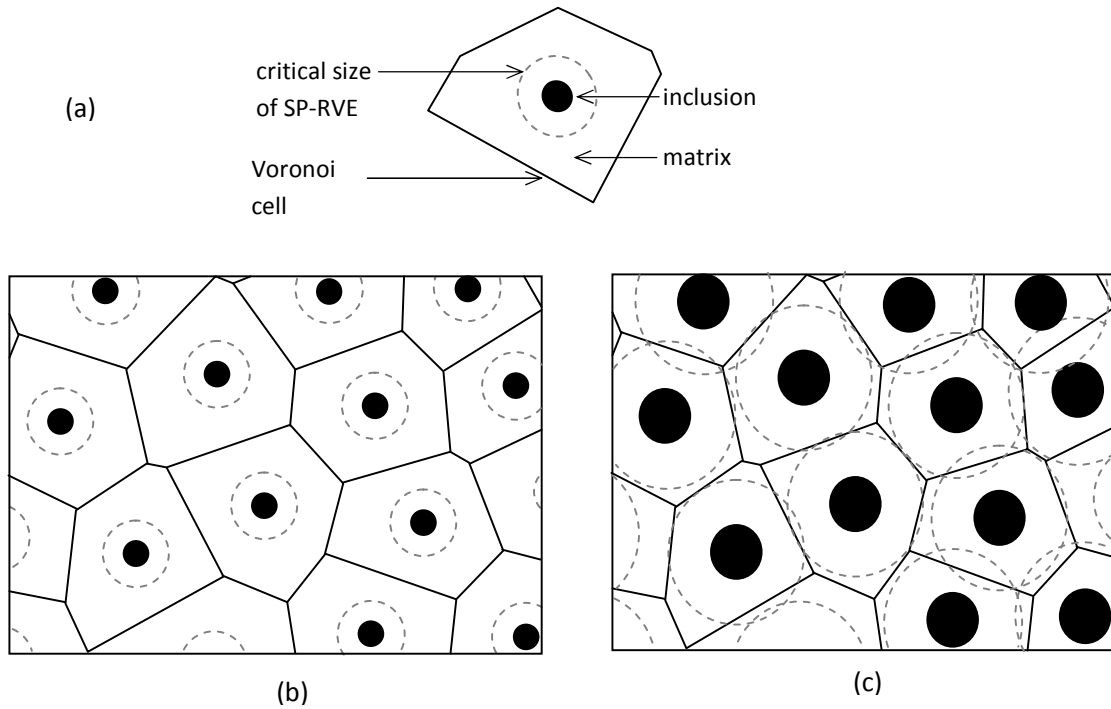
Figure 3.5: (a) Description of a Voronoi cell; (b) Non-overlapping boundaries for critical size of
SP-RVE in composite with low volume fraction of inclusions; (c) Overlapping
boundaries for critical size of SP-RVE in composite with high volume fraction of
inclusions.

By dividing the micro-structure of a bi-phasic composite into domains using

Voronoi cells, the distance between inclusions would be larger for low f. Hence the

presence of inclusion would have lesser effect on the "boundary" stresses as illustrated in

Figure 3.5b. At high f, the critical size of the SP-RVE extends beyond the boundaries of

the Voronoi cells which overlap each other as shown in Figure 3.5c. This implies that

there is significant influence of the inclusion on the boundary stresses of a Voronoi cell
which explains why the SP-RVE model is not accurate for such situations.

The MP-RVE approach accounts for the interaction between inclusions to a
greater extent and hence will be valid for cases with higher f as well as for studies on the
effect of clusters on the macroscopic response of non-homogeneous materials. Larger
MPE-RVE adopted will yield better results, as shown in Figure 3.4. To minimize the
error between the actual micro-structure and the generated microstructure for the RVE,
simulations with multiple random realizations for different arrangements of inclusions
can be performed. Thus the MP-RVE approach can be expected to provide better
predictions than those by SP-RVE approach.

However, generating and simulating multiple realizations can be computationally
costly. For the problems where the interaction between particles is negligible, such as
studies to determine the elastic behavior or the effect of interfacial zone on composites
with low f, the SP-RVE approach is able to provide sufficient accuracy at low
computational cost. For instance, the elastic behavior of porous epoxy with 15% of voids
or less in this study can be predicted accurately with an error of less than 10% using SP-
RVE A, where the total computational time is less than half an hour; while it took more
than three hours to complete 1 realization using MP-RVE on the same computer, with no
significant improvement in accuracy.

This leads to the practical question of the critical volume fraction for which the
SP-RVE approach can be applied for elastic analysis. Drugan and Willis (Drugan and
Willis, 1996) adopted a nonlocal constitutive model at micro-scale to solve the

homogenization problem for elastic composites theoretically and provided an estimate for

the minimum size of the SP-RVE. They derived the minimum size for bi-phasic

composites as

$$a_{\min} = 2\pi r \left| \frac{3f(1-f)^2(2-f)(D_1 + 2D_2)}{5\alpha(1+2f)(3K_L + 4G_L)} \right|^{1/2} \tag{3.6}$$

where

$$D_1 = 8K\delta G(3K+4G)\frac{5(3K+4G)[2\delta G(3K+8G)-21\delta KG]-12(1-f)\delta K\delta G(3K+G)}{21(1-f)\delta K+3K+4G)[5G(3K+4G)+6(1-f)\delta G(K+2G)]^2} \tag{3.6a}$$

$$D_2 = \frac{-20G(\delta G)^2(3K+4G)(3K+8G)}{7[5G(3K+4G)+6(1-f)\delta G(K+2G)]^2} \tag{3.6b}$$

$$K_L = \frac{K(3K_1+4G)+4fG(K_1-K)}{3K_1+4G-3f(K_1-K)} \tag{3.6c}$$

$$G_L = G\frac{G(9K+8G)(1-f)+3KG_1(2+3f)+4GG_1(3+2f)}{5G(3K+4G)+6(1-f)(G_1-G)(K+2G)} \tag{3.6d}$$

in which K and G are the bulk and shear modulus, respectively, of the matrix; K_1 and G_1

are the bulk and shear modulus, respectively, of the particles; δK is the difference

between the bulk modulus of the matrix and the particles; δG is the difference between

the shear modulus of the matrix and the particles; and α is the level of accuracy.

Recall that Equation (3.1) gives the relationship between f and a/D even for the extreme case where the inclusions are void. Hence, to find the minimum a for the porous material, Equation (3.1) is plotted as a solid curve in Figure 3.6. By plotting Equation (3.6) for 10% error in Figure 3.6, the intersection of both curves gives the critical volume fraction beyond which the SP-RVE may no longer be accurate.
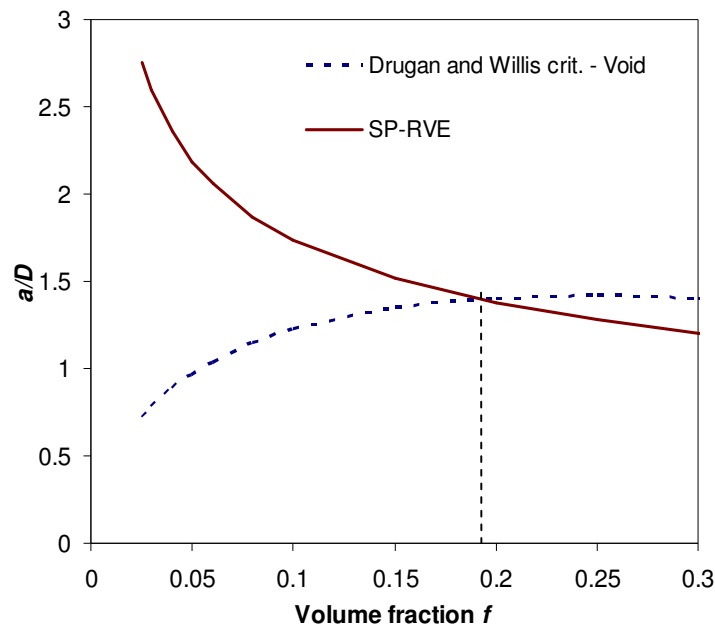
Figure 3.6: Finding critical volume fraction for SP-RVE approach using Drugan and Willis criterion

It can be seen from Figure 3.6 that when f exceeds the critical value of 19%, the prediction error may exceed 10% which agrees with the results of the current study shown in Table 3.2, where the predictions from the SP-RVE model differ from the reported experimental data by 10.7% at $f = 20\%$. Above the critical volume fraction, the MP-RVE model is expected to give much better prediction than the SP-RVE model and this is evident in the 5.8% error in prediction obtained for MP-RVE type E.

3.3.1.2. Comparison of the predictions from RVE approach and theoretical

models

The effective Young's modulus of porous epoxy based on RVE approaches, theoretical models and experimental tests are compared in Table 3.3, in which the % error of predicted values compared to experimental values are shown in parenthesis. Graphically, the comparison is displayed in Figure 3.7.

Table 3.3: Measured and predicted Young's modulus of porous epoxy

Vol% of voids	Test results	SP-RVE approach	MP-RVE approach	Voigt model	Dilute Distribution model	Self – Consistent model	Mori – Tanaka model
0	3.08	3.08	3.08	3.08	3.08	3.08	3.08
5	2.63	2.80(+6.5%)	2.79(+6.1%)	2.92(+11.1%)	2.77(+5.1%)	2.77(+5.2%)	2.82(+7.2%)
10	2.38	2.56(+7.4%)	2.52(+5.9%)	2.77(+16.3%)	2.46(+3.2%)	2.46(+3.4%)	2.58(+8.5%)
15	2.17	2.34(+7.8%)	2.27(+4.6%)	2.62(+20.5%)	2.14(-1.5%)	2.15(-1.0%)	2.36(+8.7%)
20	1.94	2.14(+10.8%)	2.05(+5.7%)	2.46(+27.0%)	1.82(-6.4%)	1.84(-5.1%)	2.16(+11.4%)

numbers in parenthesis denote the % error as compared to experimental values

The predictions from theoretical models are obtained using Equations (2.1) to (2.6) in Chapter 2 with two following remarks. Firstly, the Reuss' model and Hashin-Strikman upper bound is inapplicable for this case, i.e. particles are void with zero G and K which makes the formulae unidentified. This illustrates one of limits of these models. Secondly, the predictions using Mori-Tanaka model is identical to those using Hashin-Strikman lower bound, which is also stated by Mishnaevsky (Mishnaevsky, 2007).
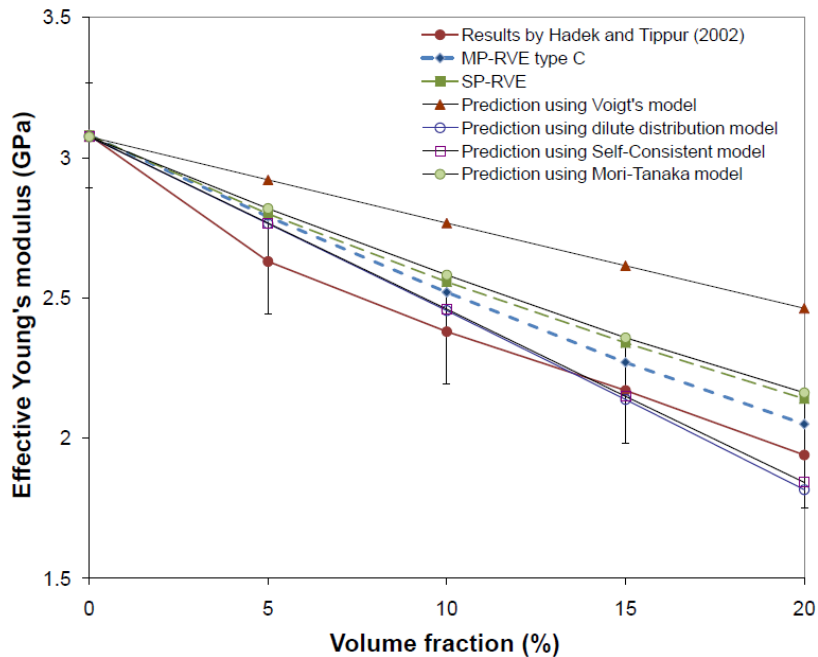
Figure 3.7: Measured and predicted Young's modulus of porous epoxy using theoretical models
and RVE approaches

As can be seen, the theoretical models and the RVE models fit experimental data
well. Similar to the predictions using RVE approaches, the effective Young's modulus
obtained from theoretical models exhibit a gradual decrease in effective Young's
modulus with an increase in the volume fraction of pores. With regard to accuracy of the
different models, it is shown that Voigt's model is the most inaccurate model, as
predicted, while DD and SC models gave the two most accurate set of predictions. The
results obtained from the more popularly used Mori-Tanaka model are similar to those
using the single particle RVE approach with level of accuracy at about 90%. Actually,
each theoretical model may give excellent prediction of the Young's modulus for some
types of composite material but may not give perfect fit for others. The statistical
variations in the size and distribution of the pores have not been reported in the

experiments and thus could not be modeled. Otherwise, it may be possible to explain the

deviation of the results.

Although MP-RVE approach does not provide the best fitted values, its

predictions are at about 6% of error and independent on the volume fraction of pores. On

the other hand, the error in predictions from SP-RVE approach and all theoretical models

including of DD and SC models keep increasing when the void contents getting more and

more. This trend is because in all of these models, the interactions between particles are

only partially modeled. As discussed in previous Section, the significance of this error

increases with the raise in volume fraction of particles, which leads to a more

considerable contribution of interactions between particles to the effective mechanical

response of the composite.

3.3.2. Prediction of inelastic response

Since the composite considered here is quasi-brittle, the strain-hardening response

is negligible. Therefore, only strength and strain-softening response will be investigated.

The numerical predicted strengths are compared against the reported experimental

strengths in Table 3.4. As can be seen, the accuracy is similar to that exhibited for the

Young's modulus in Table 3.2, probably due to the fact that the ultimate-stress is the limit

of the elasticity regime in this case with negligible strain hardening. The results also seem

to indicate that the accuracy of the SP-RVE approach diminishes when the voids content

is increased due to the effect of clustering at high f as discussed in Section 3.1.

Table 3.4: Prediction of strength of porous epoxy using RVE approach

Properties	Vol% of voids	SP-RVE	MP-RVE			Reported results
			Type C	Type D	Type E	
Strength (MPa)	0	53.0	53.0	53.0	53.0	53.0
	5	45.3 (-3.2%)	44.8 (-4.1%)	45.1 (-3.6%)	44.4 (-5.1%)	46.8
	10	39.4 (-7.3%)	39.2 (-7.7%)	39.9 (-6.1%)	40.0 (-5.8%)	42.5
	15	35.9 (-9.9%)	36.8 (-7.7%)	37.1 (-6.8%)	37.8 (-5.1%)	39.8
	20	31.6 (-12.5%)	33.1 (-8.3%)	33.9 (-6.1%)	34.2 (-5.3%)	36.1

numbers in parenthesis denote the % error as compared to experimental values

The strain-softening responses of all the RVEs considered are shown, as a part of the stress-strain curves, in Figure 3.8, where the stress-strain relationship of epoxy with 5% of voids predicted using SP-RVE type A, and typical realizations of SP-RVE type B and MP-RVE types C, D and E for the three sizes of 250μm, 300μm and 350μm are presented.
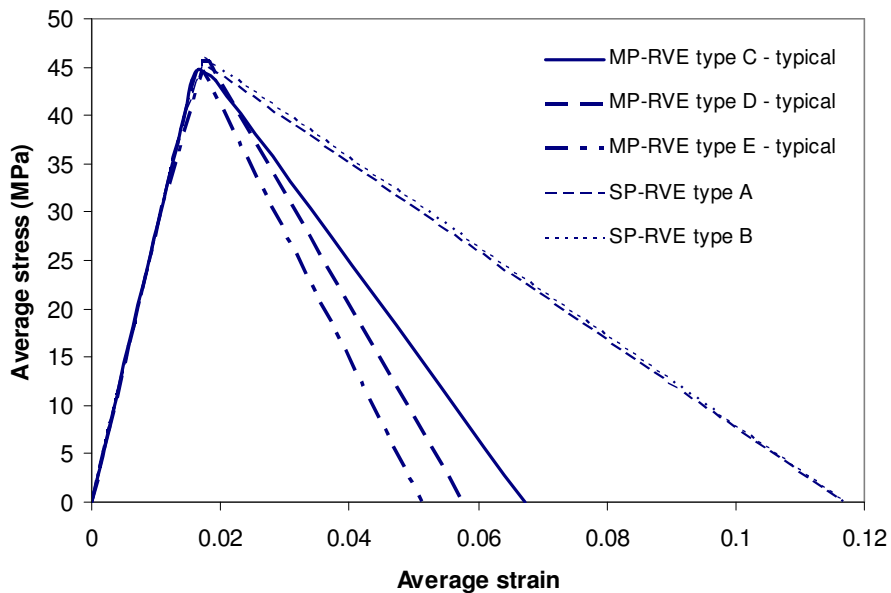
Figure 3.8: Stress-strain curves obtained by RVEs at f = 5%

As be shown, the stress-strain curves of SP-RVE types A and B are almost indistinguishable, including the strain softening segment, confirming that the two types of SP-RVEs are physically identical. This is due to the enforcement of periodic boundary conditions where all field variables on one edge/surface of a RVE are repeated on the opposite edge/surface. Continuity of stress and deformation states between opposite edges/surfaces cancel out the effects of free surfaces with regards to damage evolution.

Unlike the pre-peak regime, the post-peak softening curve characterizing the damage behavior shows obvious size dependence where an increase in the size of the RVE leads to a steeper strain softening slope, accompanied by a corresponding decrease in ultimate strain and this trend agrees with the findings by Gitman et al. (Gitman et al., 2007) which is shown in Figure 3.9a. The size dependence of the stress-strain curve from RVE predictions suggests that there may not be a suitable volume element that can provide a representative stress-strain curve for quasibrittle composites which, in general, exhibit strong strain softening behavior.

In contrast, Pelissou et al. (Pelissou et al., 2009) performed numerical studies on a bi-phasic composite comprising brittle Zirconium hydrides inclusions embedded in elasto-plastic Zircaloy metal matrix and pointed out that the fracture energy density, which is the area under the stress-strain curve, will converge with an increase in the size of the RVE. Since the linear elastic and strain hardening regimes are reported to be non-varying with the size of the RVE, as shown in Figure 3.9b, the convergence of the area under the stress-strain curve also confirms the convergence of the entire stress-strain curve, including the softening regime.
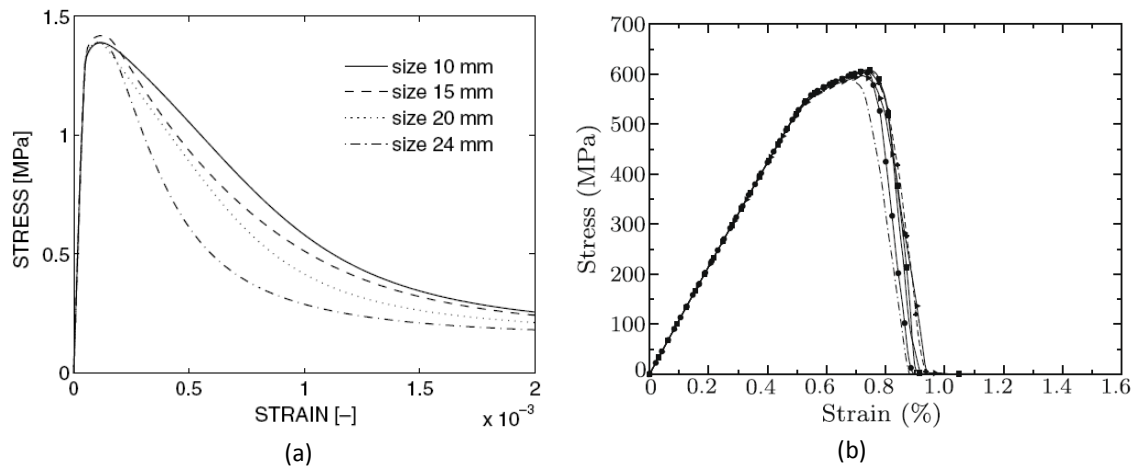
Figure 3.9: Predicted stress-strain behavior of composites containing 30% of inclusion using RVE
of different sizes: (a) brittle interface and matrix with perfectly elastic inclusions
showing strong size dependence on RVE, after Gitman et al. (Gitman et al., 2007) (b)
elasto-plastic matrix with perfectly brittle inclusions showing size independence on
RVE, after Pelissou et al. (Pelissou et al., 2009).

Although there is no report on the crack pattern in the study by Pelissou et al.
(Pelissou et al., 2009), it can be expected that for the brittle inclusions having a much
lower ultimate strain than the surrounding elasto-plastic matrix, the damage will be
extensive and spreads throughout the RVE involving almost all the inclusions instead of
localizing at a major crack. Hence, Pelissou et al. (Pelissou et al., 2009) reported that the
stress-strain curve is independent on the size of the RVE, which can only be true if the
number of cracks scales with the size of the RVE. This could be possible at low volume
fraction of the brittle phase whereby at the onset of crack formation, the stresses can be
distributed to the uncracked regions through the elasto-plastic matrix but at high volume
fraction of the brittle phase, this may be almost impossible due to loss of continuity of the
matrix.

In general, a quasi-brittle bi-phasic composite may comprise two quasi-brittle phases or one quasi-brittle phase and one elasto-plastic phase. Consider an idealized model of a bi-phasic material under tension being represented by a chain of bundles shown in Figure 3.10a where each bundle represents a cross-section of the RVE and the number of bundles is a function of the minimum crack spacing, the squares representing the inclusions and the circles representing the matrix.
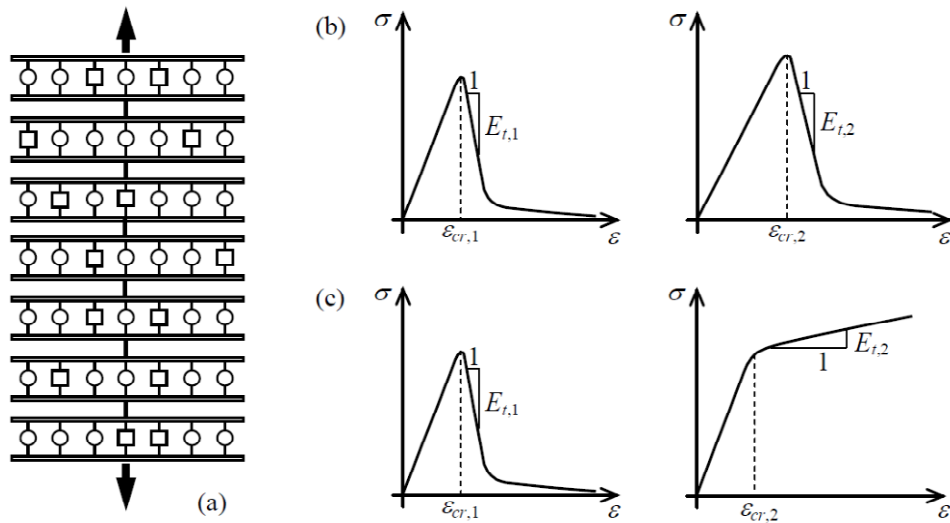
Figure 3.10: (a) Idealized fiber bundle model for describing load distribution in a RVE for a bi-phasic composite; (b) stress-strain curves for brittle phases 1 and 2; (c) stress-strain curves brittle phase 1 and elasto-plastic phase 2.

Under tensile action, the average stress σ_{avg} can be expressed as

$$\sigma_{avg} = \sigma_1 V_1 + \sigma_2 V_2 = (E_{t,1} V_1 + E_{t,2} V_2)\varepsilon_{avg} \tag{3.7}$$

where V_1, V_2 are the volume fractions, and $E_{t,1}$, $E_{t,2}$ are the corresponding tangent moduli for phases 1 and 2 respectively.

When the average strain ε_{avg} across the critical cross section exceeds the cracking strain of the more brittle phase, damage will start to localize with accumulation of inelastic strain while the remaining sections unload provided that $\delta\sigma_{avg}/\delta\varepsilon_{avg} < 0$, which leads to the following criterion:

$$(E_{t,2} - E_{t,1})V_1 > E_{t,2} \tag{3.8}$$

Since V_1 must lie between 0 and 1, the inequality in Equation (3.8) can be satisfied for the following cases:

<u>(a) Both phases are brittle</u>

Consider a bi-phasic composite comprising phases 1 and 2, with phase 1 being the more brittle phase having the lower cracking strain $\varepsilon_{1,cr}$ as shown in Figure 3.10b. When phase 1 of the critical section goes into softening, characterized by a negative instantaneous stiffness on the stress strain curve i.e. $E_{t,1} < 0$, localization will occur if the volume fraction V_1 satisfies the following inequality:

$$V_1 > \frac{E_{t,2}}{E_{t,2} - E_{t,1}} \tag{3.9}$$

Though the volume fraction of brittle phase 1 may not satisfy the inequality in Equation (3.9) when phase 1 becomes damaged, the composite will inevitably softens when ε_{avg} exceeds the cracking strain $\varepsilon_{cr,1}$ $\varepsilon_{cr,2}$ of both phases 1 and 2, thus always satisfying the inequality in Equation (3.9).

<u>(b) One phase is brittle while the other is elasto-plastic</u>

When phase 1 is brittle while phase 2 is elasto-plastic, it is still possible for the composite to behave in a quasi-brittle manner with localization of damage if the volume fraction of the brittle phase 1 satisfies the inequality in Equation (3.9). Since the tangent modulus of elasto-plastic phase 2 is always positive as shown in Figure 3.10c, this would only be possible if the tangent modulus of phase 1 is negative, thus implying damage and softening in the brittle phase.

The localization of the damage in a critical section while the rest of the RVE unloads, would lead to a softening in the homogenized stress-strain behaviour of the composite, thus implying a size dependence on the average stress-strain curve (Bazant and Planas, 1998).

From the above arguments, it can be concluded that quasi-brittle composites, in general, experiences strong damage localization, resulting in the formation of a single major crack in the RVE when subjected to tensile action. While the size effect on the homogenized stress-strain curve in the softening region leads to difficulty in the RVE approach for predicting the stress-strain behaviour, the energy to create a unit area of crack surface may be size invariant and suitable for characterizing the inelastic behaviour that involves fracture (Bazant and Planas, 1998).

3.4.   FRACTURE ENERGY PREDICTED USING RVE APPROACH

The fracture energy predicted using RVE approach is determined through the area under the simulated homogenized stress - displacement curve of the RVE and tabulated in Table 3.5. The fracture energy predicted from MP-RVEs type C, D and E are close to

one another implying independence of size on this parameter. As a result, the fracture

energy or stress-crack opening displacement is suitable for predicting the brittle

behaviour of composites, rather than the dissipated energy or stress-strain relationship

usually adopted, to avoid the size sensitivity of the RVE approach. The result reveals that

there is a trend of decreasing fracture energy with the increase in the degree of porosity;

and this trend is identical to the trend of the fracture toughness observed from the

reported experiments (El-Hadek and Tippur, 2002).

Table 3.5: Prediction of fracture energy and fracture toughness of porous epoxy using RVE
approach

Properties	Vol% of voids	SP-RVE	MP-RVE			Reported results
			Type C	Type D	Type E	
Fracture energy	0	4.109	4.109	4.109	4.109	
	5	3.511	3.980	3.778	3.919	
	10	3.055	3.812	3.843	3.769	
$(10^{-4}$ MPa.m)	15	2.706	3.894	3.808	3.914	
	20	2.491	3.752	3.718	3.627	
Fracture toughness	0	1.200	1.200	1.200	1.200	1.20
	5	1.056 (-4.0%)	1.125 (+2.3%)	1.095 (-0.5%)	1.116 (+1.5%)	1.10
	10	0.939 (-6.1%)	1.048 (+4.8%)	1.053 (+5.3%)	1.040 (+4.0%)	1.00
$(MPa.m^{1/2})$	15	0.842 (-12.3%)	1.009 (+5.1%)	0.998 (+4.0%)	1.007 (+4.9%)	0.96
	20	0.773 (-13.6%)	0.948 (+6.3%)	0.933 (+4.8%)	0.920 (+3.4%)	0.89

To assess the use of fracture energy as a size invariant measure to characterize the

fracture behaviour using the RVE approach, the fracture toughness of the porous epoxy

obtained from published experimental data are compared to those estimated from

numerical simulation, where the predicted fracture energy is converted into fracture

toughness using Equation (3.5). In deed the comparison will be more accurate if the

fracture energy extracted from literature is a direct measurement. The comparison in this

paper plays a role as a numerical example for the use of RVE approach to predict the damage behaviour of the composites with the assumptions that fracture energy can be treated as a material constant and the arrangement of micro-pores in the pre-defined damage zone creates an initial defect inside the RVE.

One concern that may be raised is the presence of the notch in the reported experiments while notch was absent in the current simulations using the RVE approach. As discussed by van Mier (van Mier, 1997) and Janssen et al. (Janssen et al, 2004), a notch has two main effects. Firstly, a notch confines the crack growth and ensures that there is only a single crack in the specimen, which is identical to having a single crack in the RVE in the current study. Secondly, a sharp crack tip will be detrimental to the fracture toughness since it will limit the plastic development of the crack. This effect may not happen in the experiments, where an initial notch of root radius 75μm, which is 2.5 times larger than the radius of the micro-pores, was used.. Although the notch's mouth was subsequently sharpened by "gently tapping-in a wedge" (El Hadek et al., 2002), the size of the newly-formed crack tip was probably large compared to the size of the micro-pores. As a result, the effect of stress concentration at the crack tip may not be so significant.

The comparison between the predicted fracture toughness and the experimental results is shown in Table 3.5, where the numbers in parenthesis denote the percentages of error. The fracture toughness decreases with increase in f for both the numerical simulation and the experiment as depicted in Figure 3.11, which is expected due to the zero resistance offered by the voids. The consistency in the predicted fracture toughness

using MP-RVEs type C, D and E shown in Figure 3.11 is a graphical presentation of the

size independence of the simulated fracture energy tabulated in Table 3.5.
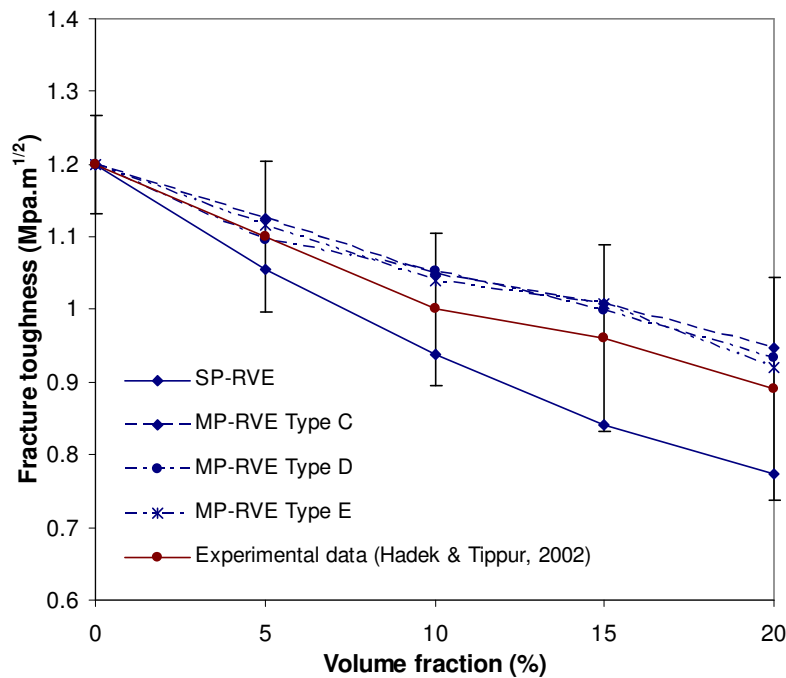
Figure 3.11: Effective fracture toughness obtained from RVE approaches and experiments

In terms of accuracy, the MP-RVE approach provides good predictions with less

than 6% error for f up to 20% and these errors do not show a clear trend with the size of

the RVE, thus supporting the use of RVE for material characterization in terms of the

effective fracture energy. At $f < 10\%$, the SP-RVE approach provides accurate prediction

of the fracture toughness with less than 7% error, albeit a lower bound estimate. The

lower estimation of fracture toughness for SP-RVE is due to the crack cutting across the

narrowest cross section of the RVE where the void projected area is largest and by virtue

of the imposed periodic boundary conditions, leads to a perfectly planar crack surface as

shown in Figure 3.12a. However in the MP-RVE models and in the actual composite, the

voids may not be aligned on a rectangular grid and hence the crack surface may not be

planar, exhibiting a "rough" and larger fracture surface as shown in Figure 3.12b. This

will naturally imply higher fracture toughness compared to that based on SP-RVE.
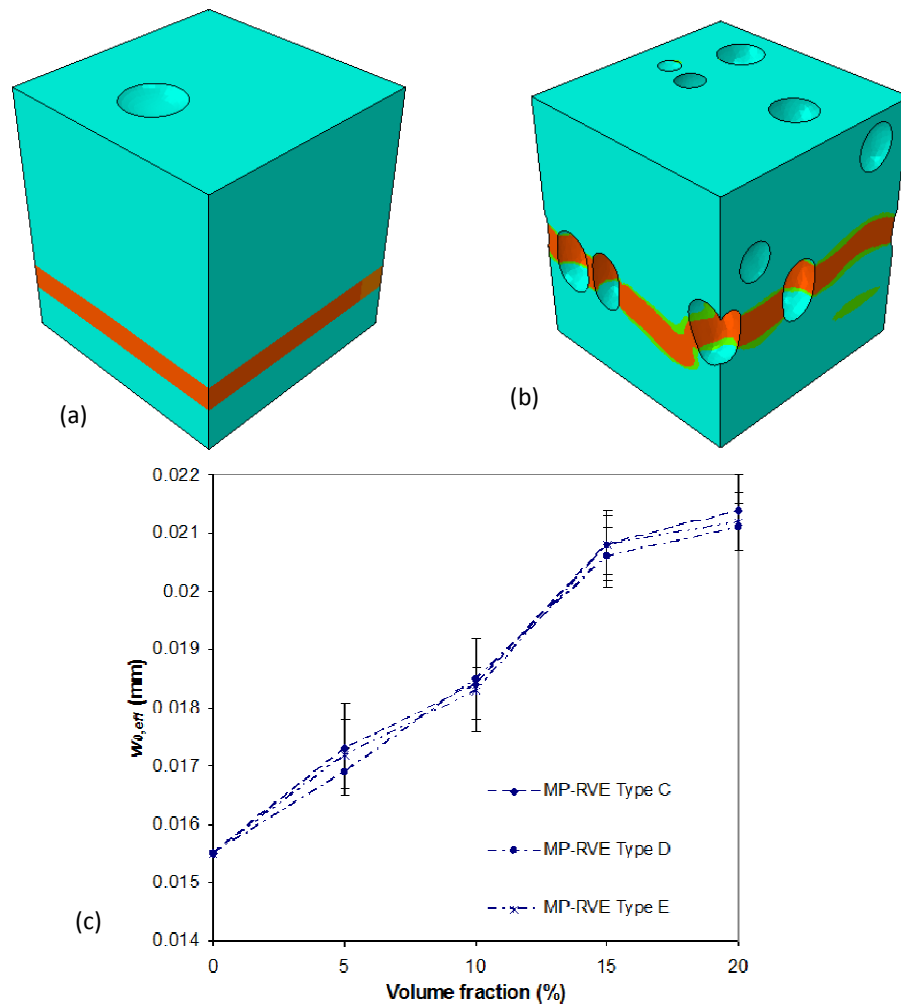
Figure 3.12: Simulation of cracks in porous epoxy using smeared crack model: (a) perfectly
planar crack surface for SP-RVE; (b) rough crack surface and tortuous crack path for
MP-RVE; (c) convergence of the effective maximum crack opening displacement at
all volume fraction of voids.

The above as well as Table 3.4 show that the error in the prediction of the fracture toughness and the strength does not have a clear trend with the size of RVE used. The usual description of the fracture behaviour is in terms of stress against crack opening displacement instead of stress against strain, as the latter suffers from size effect arising from damage localization. Therefore, the effective maximum crack opening displacement predicted from the MP-RVE models should not depend on the size of the RVE. This is substantiated by the results in Figure 3.12c which shows the variation of effective maximum crack opening displacement with respect to the volume fraction of voids for the three different sizes of the MP-RVEs.

In terms of efficiency, the SP-RVE approach performs much better at low *f*. For comparable level of accuracy of less than 6%, the total computational time for one realization takes only about 10 hours for the SP-RVE model while it takes about 48 hours for the MP-RVE model. As this study is only specific to porous composite, the critical volume fraction of inclusions for which the SP-RVE approach is accurate for predicting the fracture toughness of bi-phasic composites in general, remains to be determined.

3.5.   SUMMARY

The adequacy of both the SP-RVE and MP-RVE approaches to predict the mechanical behaviour of quasi-brittle composites are examined in this Chapter using porous epoxy as an example. The SP-RVE approach is computationally more efficient for composites containing low volume fraction of inclusions, about five times faster than that for the MP-RVE. Based on Drugan and Willis' criterion on minimum size of the RVE, it

is shown that for bi-phasic composites containing voids as inclusions when the volume
fraction of voids exceeds the critical value of 15%, the accuracy of prediction for the
elastic properties will exceed 10% for the SP-RVE approach while the MP-RVE
approach remains accurate even for higher volume fractions. Results from simulations
also reveal that the results from the SP-RVE model with proper periodic boundary
conditions imposed are invariant with the position of the particle as all realizations are
simply a unit cell of a structure with uniformly distributed particles.

Compared to theoretical models, the predictions of elastic properties of the porous
epoxy using SP-RVE approach is very close to the commonly used Mori-Tanaka model.
Similar to SP-RVE approach, all theoretical exhibit the trend of increasing the error of
prediction when the volume fraction of particles getting higher. This fact reconfirms the
powerfulness of MP-RVE approach for simulate material properties of composites
containing high volume fraction of reinforcements.

The smeared crack model is used to ascertain the suitability of the RVE approach
for studying the inelastic softening response. The strong localization of damage with the
formation of a single crack across the critical cross section indicates that the RVE may
not be suitable for predicting the inelastic stress-strain softening response of quasi-brittle
composites. It is shown that fracture energy or the fracture toughness (through the stress
versus crack opening displacement relationship) could be used as a size invariant
property to characterize the fracture resistance. As an example for the case of porous
epoxy, the fracture toughness predicted from the MP-RVE models compares well with
the experiment results for up to 20% volume fraction of voids investigated in this study
while the SP-RVE model should not be used for volume fractions greater than 10%.

In the current study, the MP-RVEs at the size of 250µm, i.e. MP-RVE type C, can

provide reasonable accurate predictions, at less than 10% of error, for the material

properties, both elastic and inelastic, of the epoxy containing 60µm diameter voids. This

means MP-RVE sizes that are at least 4 times larger than the size of inclusions might be

used to model the effective response of heterogeneous materials comprising of voids or

very soft inclusions surrounded by a quasi-brittle homogeneous medium.

CHAPTER 4

NUMERICAL SIMULATION OF SELF-HEALING MATERIALS WITH CAPSULATED SYSTEM

4.1.   INTRODUCTION

Until now, micro-capsule based self-healing materials is the most widely used and developed system for the class of self-healing materials using capsulated adhesive. Since the first well-known announcement of this type of self-healing composite, there have been numerous experimental studies to enhance the performance of micro-capsule based self-healing materials such as those on host matrix materials and healing agents (Kessler and White, 2001; Kessler et al., 2002, 2003; Brown et al., 2002; Jones et al., 2007; Mauldin et al., 2007 and Caruso et al., 2007) as well as those on effects of size and volume fraction of capsules on healing efficiency in terms of recovered fracture toughness (Brown et al., 2004 and Rule et al., 2007). The detailed reviews of the above researches are provided in Chapter 1.

On the other hand, the development of numerical models developed for micro-capsule based self-healing materials, and for all other types of self-healing composites as well, is very limited. Two numerical studies have been published by Keller et al.

(2006) to predict the elastic behaviour of capsules under micro-compressive test and by Remmers and de Borst (2007) to develop a multi-phase cohesive segments method to simulate the micro-capsule based self-healing materials. The former work is to characterise the Young's modulus of micro-capsule shell under compression by adopting the theoretical solution proposed by Wang et al. (2004) for the problem of fluid-filled membrane under compression; the latter work is an introduction of a two-dimensional method that may be used for crack propagation analysis of self-healing materials at micro-scale but has yet to be compared and verified with experiments.

In this chapter, homogenization approach is applied to develop a numerical model for micro-capsule based self-healing materials. Section 4.2 is a preliminary study to find the elastic properties of both capsule wall and capsulated fluid. The material properties of micro-capsule based self-healing material are modelled using the RVE concept with an appropriate model for micro-capsule based on results of the preliminary study and the observations from the published experiments and presented in Section 4.3. The effective material properties such as Young's modulus, strength, and healing efficiency are simulated and verified against published experimental data. Following that, the structural response of beam specimens made from the same self-healing materials is presented in Section 4.4. Studies on the effect of strength of healing agent and type of healing system are discussed in this section. A summary of this chapter is presented in Section 4.5.

4.2.   PRELIMINARY STUDIES ON ELASTIC RESPONSE OF MICRO-CAPSULES

4.2.1. Experimental results from micro-compression test

Micro-compression tests of microcapsule identical to those used in SHM (Kessler and White, 2001 and Brown et al., 2004) were carried out by Keller et al. (2006). There were 3 groups of capsules of different mean diameters, namely, 65±6 μm (group A), 187±15 μm (group B) and 213±12 μm (group C). The skin of the capsules were made of urea-formaldehyde (UF) which had a uniform wall thickness of 175 ± 33 nm, independent of the capsules diameter. The capsules were filled with dicyclopentadiene (DCPD) liquid monomer (the healing agent). Each single capsule was drawn by pipette and placed on the compression platen for groups A, B, C (dry test) or in immersion cell containing DCPD for group C (immersed test). The punch was lowered until it is in contact with the capsule and displacement controlled loading at rate of 5 μm/s was applied for the larger capsules in groups B and C. The loading rate of 2.5 μm/s was adopted for the smaller capsules in group A to ensure that the yield point and maximum strength can be determined from the test. Figure 4.1a shows the set-up of the experiments, in which the immersion cell was used only in the immersed test. The capsules were tested to failure and images of deformed capsules were captured during the test as shown in Figure 4.1b. Image 1 shows the initial state of the capsule before testing while image 2 shows the shape of the capsule at yield, which occurs at dimensionless displacement d/D of about 15%, where d is the vertical displacement at the top of the capsule and D the initial capsule diameter. Images 3 and 4 were captured just before and after the failure of the capsule, respectively. The diffusion of DCPD through the membrane may have severe consequences on the stresses acting on the capsule wall. To investigate the extent of diffusion, DCPD was

coloured using an oil-soluble dye. It was observed that, before application of the load,

there was no observable diffusion for groups A and B, which suggested that the

capsule wall was impermeable, whereas some diffusion is observed for group C in the

long term. As a result, immersed test was designed for capsules in group C to ensure

constant volume. From these experiments, the researchers obtained the force versus

dimensionless displacement curve of capsule up to a maximum d/D of 15%.

(a)   (b)
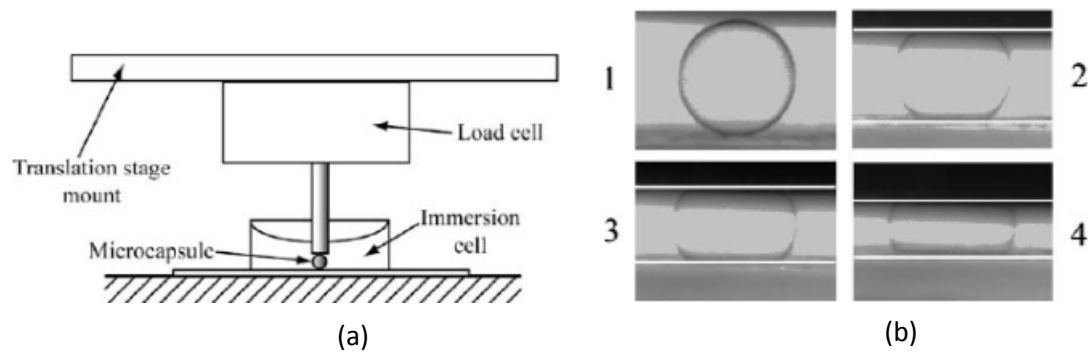
Figure 4.1: Dry and immersed compression test on the micro-capsule: (a) Schematic of tests
(immersion cell was only used in immersed test); (b) Deformed shape of micro-
capsule under compression (after Keller *et al.*, 2006).

Using analytical approach, proposed by Wang et al. (2004) to solve the

problem of fluid-filled membrane under compression, Keller et al. (2006) calibrated

the Young's modulus of the capsule wall with the mean values of 3.7±0.5, 3.6±0.4

and 3.9±0.7 for capsules in groups A, B, C, respectively. The slight variation of the

Young's modulus may be caused by the non-uniformity of the capsule wall due to

chemical and manufacturing problems. As their conclusion, the calibrated elastic

modulus of the wall is 3.7±0.2 GPa. The load versus dimensionless displacement

curves for specific capsules having diameter 223 μm in immersed test, 169 μm and 61

μm in dry tests, were reported.

4.2.2. Finite element model using bi-phasic materials

The above micro-compression experiments for 175nm thick capsules having diameters of 223 μm, 169 μm and 61 μm, will be numerically modelled and analyzed using the commercial FE package, ABAQUS 6.7 with the following basic assumptions:

a. The capsule is a perfect sphere and its volume is constant.

b. The material properties are time and strain invariant.

c. Perfect bonding is assumed for the interaction between the healing agent and the capsule wall. The punch is a rigid body and during compression, no slippage occurs between the punch and the capsule.

4.2.2.1. Boundary conditions and loading

Due to symmetry, only one eighth of the capsule was modeled. Geometric parameters include the capsule radius R and wall thickness t as illustrated in Figure 4.2. Symmetric conditions were applied on three symmetric planes, and the rigid punch was constrained from all degrees of freedom except the translation in the direction of compression (Y direction). Similar to the experiments, displacement-controlled loading was imposed. During the simulation, the contact between the punch and the capsule was determined by measuring the distance between them. The corresponding force applied on the capsule was calculated from the reaction of the capsule on the punch.

General contact model (Abaqus Theory Manual, 2007) between the capsule
wall and the punch is employed. In normal direction of contact surfaces, there is no
transfer of tensile stress is allowed across the interfaces. This condition is called "hard
contact" in Abaqus. In tangent direction of contact surfaces, smooth contact without
friction is applied.
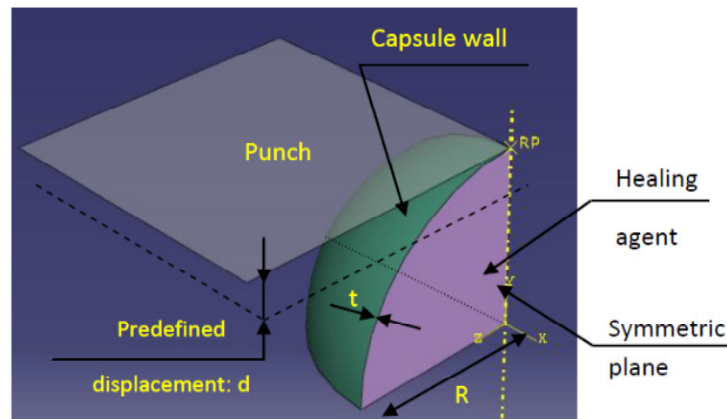
Figure 4.2: Finite element model of compressive test for micro capsules.

4.2.2.2. Material model and element type

An accurate representation of the capsule in the finite element model should
be a combination of fluid elements for healing agent and membrane elements for the
capsule wall due to its small thickness compared to the diameter of the capsule.
However, a coupled solid-liquid interaction problem with contact analysis is not easy
to solve with commercial FE packages such as ABAQUS and numerical difficulties in
solving the interactions between fluid elements and solid elements at the interface
would be encountered. As an alternative, a rubber-like material, which is
incompressible and can sustain large deformation, is being evaluated for modelling of
the healing agent. One such model is the Neo-Hookean material model, which is a
simple hyperelastic material model that is described only by its shear modulus G. It is

often used to model very soft materials that can sustain large deformation, such as the

modelling of biological cells (Zhou et al., 2005; Peters et al., 2005) and may be

appropriate for this purpose.

Neo-Hookean material model is described by its strain energy potential

(ABAQUS, 2007):

$$U = \frac{G}{2}(I_1 - 3) \tag{4.1}$$

where I_1 is the deviatoric strain invariant, defined as:

$$I_1 = \lambda_1^2 + \lambda_2^2 + \lambda_3^2 \tag{4.2}$$

with λ_1, λ_2, λ_3 are the principle stretches. As for the capsule wall, a linear elastic

material model is assumed, similar to that of Keller et al. (Keller et al., 2006).

In terms of element type, the membrane element would be more ideal for the

capsule wall since its thickness (0.175μm) is much smaller than the capsule diameter

(61μm to 223μm). However, the contact of the wall with the healing agent and the

punch is difficult to solve with the membrane element. To overcome this problem, the

fully integrated, quadrilateral shell element (S4) was used (ABAQUS, 2007). To

check the suitability of this element, the out of plane principal stress of the capsule

wall will be checked for zero stresses. As for the healing agent, the 8-node, fully

integrated C3D8H hybrid element for incompressible material (ABAQUS, 2007) was

adopted. The punch was modelled as a rigid object by constraining all the nodes to

have the same displacement. Convergence studies on mesh density and loading

increment were conducted to select the mesh size and loading rate.

4.2.2.3. Results and discussion

The model was used to match the experimental data (Keller et al., 2006) of 3 reported capsules with diameters are 61μm, 169μm and 223μm, respectively by varying the shear modulus of the self healing agent and the Young's modulus of the capsule wall. While the shear modulus should be identical for all 3 capsule groups, the Young's modulus of capsule wall can differ slightly between them due to the differences caused by chemical problems and manufacturing process. Figure 4.3a shows that the out of plane stress of the capsule wall is zero which confirms the membrane action (Keller and Sottos, 2006) with the use of S4 element for the capsule wall. signifies membrane behaviour and ascertains that using S4 element to model the capsule wall is appropriate.

The final results of the simulation are shown in Figure 4.3b-d. Overall, the FE model using neo-Hookean material for capsules under dry tests gave results within 10% off the experimental values, except the first 2 values for 61-micron diameter capsule due to the small displacement under low load. Nevertheless, the small deviation fall within the accuracy of the measuring equipment (Keller et al., 2006) which is 0.1mN.

Both the theoretical solution and the FE model give less accurate prediction for the compression test of the 223 micron diameter capsule, which was conducted under immersed condition. In fact, the conditions of the dry and immersed tests were not the same because of the pressure caused by external fluid surrounding the capsule in the immersed test. This was not measured in the experiments nor modelled in both theoretical and FE models the simulations and it would have reduced the surface tension to allow greater diffusion of the DCPD across the capsule wall which could

equilibrate the hydrostatic pressure across the capsule wall, leading to a smaller

stiffness at high *d/D* in the experiments and hence, the deviation from numerical

simulation results.
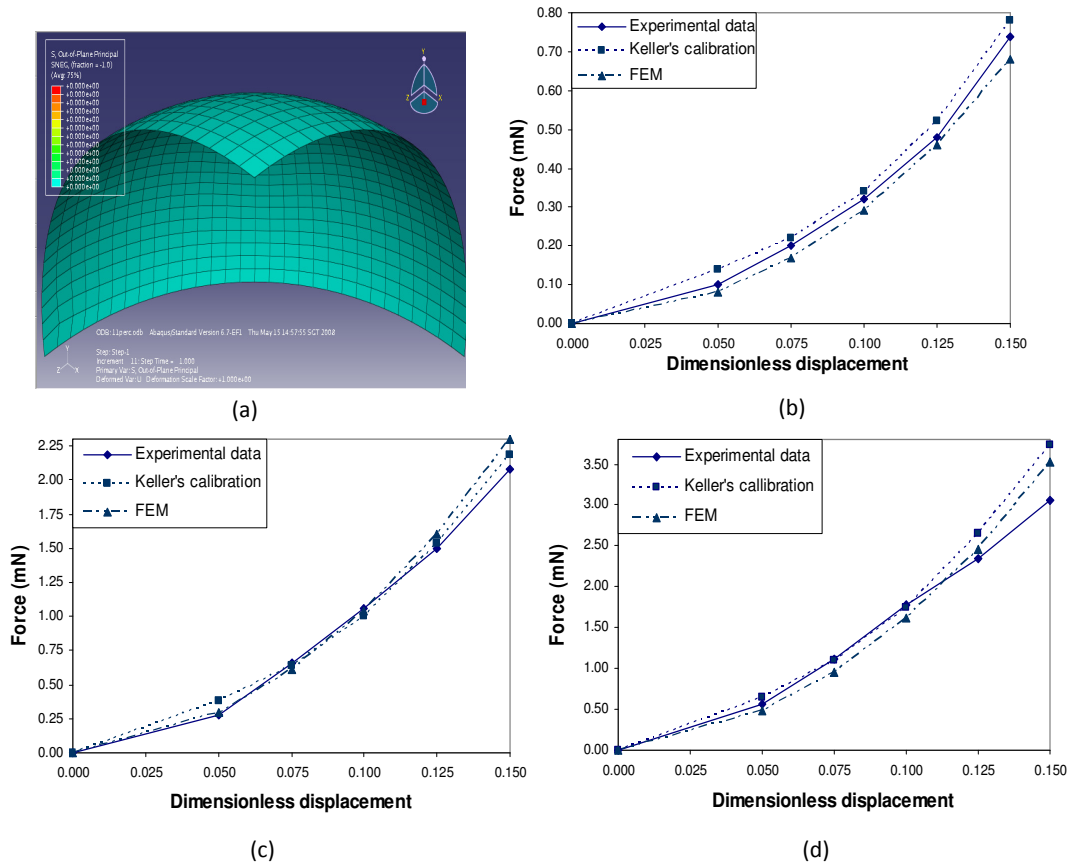
Figure 4.3: Results from FE simulation of micro-capsule under compression: (a) Zero out-of-plane stress at the wall; (b), (c), (d): force vs. dimensionless displacement for capsules with diameter of 61µm, 169µm and 223µm, respectively.

A possible source of deviation in the predicted numerical results is the

difference between the real and modelled healing agent. In reality, DCPD is a liquid

state healing agent, which would self-equilibrate the stress within itself to apply

uniform internal pressure on the capsule wall. The healing agent is however modelled

as a quasi-liquid which does not flow easily like a liquid and this may cause localised

stress concentration in the model of the healing agent. However, this difference is not

expected to create significant error because the encapsulation of the healing agent reduced the flowability of the fluid.

It has been demonstrated that the FE model using neo-Hookean material for healing agent and elastic material for the capsule wall can accurately predict the elastic response of the microcapsule in dry compression tests except at low loads where the sensitivity of the testing machine comes into question. The material properties of the capsule determined from this simulation are: shear modulus of the healing agent G_{HA} = 300 kPa and Young's modulus of the capsule wall $E_{capsule}$ = 3.7±0.2 GPa, which agrees with the reported data.

4.3.   NUMERICAL   SIMULATIONS   TO   CAPTURE   MATERIAL PROPERTIES OF MICRO-CAPSULE BASED SHM

4.3.1. Published experimental data and remarks

In 2004, Brown et al. (Brown et al., 2004) conducted experiments to determine four basic mechanical properties which included Young's modulus, E, strength, σ_f, fracture toughness K_{IC} and healing efficiency in terms of recovered fracture toughness, η, of the SHM using 180μm-diameter micro-capsules at volume fractions varying from 6% to 17%, as tabulated in Table 4.1. The specimens were cast using EPON® 828 epoxy resin (DGEBA) and 12 pph Ancamine® DETA (diethylenetriamine) curing agent with a prescribed volume fraction of micro-capsules.

Table 4.1: Mechanical properties of micro-capsule based SHM

Vol. fraction of capsules, f (%)	Young's modulus, E (GPa)	Tensile strength, σ_f (MPa)	Fracture toughness, K_{IC} (MPa.m$^{1/2}$)	Healing efficiency, η (%)
0	3.4±0.1	39±4	0.55±0.04	-
6	3.2±0.1	24±3	0.78±0.18	79±8
11	3.1±0.2	20±4	1.14±0.21	48±7
17	2.8±0.1	20±2	1.20±0.20	53±5

The test results showed monotonic decrease in both Young's modulus and tensile strength with an increase in volume fraction. In particular, the tensile strength drops to about 50% of the original host matrix when f is increased to 17%, resulting in a much weaker composite. On the other hand, a rise in the micro-capsule concentration leads to a rise in the fracture toughness for $f < 17\%$.

As commented by the authors (Brown et al., 2004), the trend in the material properties for a variation in f is similar to those obtained from the rubber modified composites, in which the addition of soft fillers will decrease the strength and stiffness while toughening the composites at low volume fraction of fillers, as reported in literature. DGEBA, which is the matrix for this SHM, is also commonly used in rubber toughened composites (Pearson and Yee, 1989; Chen and Jan, 1995; Bagheri et al., 2009). The shear modulus of encapsulated healing agent was found to be 300 kPa and is in the range of 200 kPa to 800 kPa, which is the shear modulus of rubber particles used in rubber toughened composites (Gent, 2001). The value of 300 kPa for shear modulus of rubber particles was also used by Guild and Kinloch (1995) in their numerical study to determine the elastic properties of rubber-modified epoxy polymers.

It is well-known that there are two major mechanisms that attribute to the fracture toughness of rubber modified system, namely cavitation and shear yielding in

the matrix (Bagheri and Pearson, 1996; Bagheri et al., 2009). In the former

mechanism, the embedded particles are debonded from the host matrix and cavitated

under the action of stress concentration near the crack tip. This mechanism can only

happen in composite systems with weak bonding between the particles and the matrix.

Therefore, this is not the case for SHM, in which the bonding between the micro-

capsules and the host epoxy has proved to be very strong (Brown et al., 2003). In fact,

if the micro-capsules do not bond well to the host matrix, the cracks will propagate

through the interface around the micro-capsules instead of rupturing through the

micro-capsules to release the healing agent. Therefore, weak bonding between micro-

capsules and host matrix is undesirable in self-healing composites and cavitation

could not be the reason for the improvement in fracture toughness of micro-capsule

based SHM.

In the latter mechanism, particles act as stress concentration points that

diverge the original crack path and create the shear yielding effect (Bagheri and

Pearson, 1996; Bagheri et al., 2009). The shear yielding effect, as claimed by Brown

et al. (Brown et al., 2004) after examining the SEM images of the fracture surfaces, is

believed to be the major reason for the toughening in micro-capsule based SHM. This

conclusion is totally consistent to that made by Pearson and Yee (1989) on the

toughening of composite systems with DGEBA based epoxies.

4.3.2. Numerical model

Adopting findings in Chapter 3, RVE approach is used to model mechanical

response of SHM using 180µm-diameter capsules proposed by Brown et al. (2004).

Mechanical responses of micro-capsules used in the simulating SHM are presented in Section 4.2. Material properties of the host matrix are stated in the first row of Table 4.1.

4.3.2.1. RVE generation

Three-dimensional finite element simulations using both single-particle RVE (SP-RVE) and multiple-particle RVE (MP-RVE) approaches were conducted for 3 volume fractions of 6%, 11% and 17%. While the size of the SP-RVE is varied based on the volume fraction being investigated using Equation (3.1), the size of the MP-RVE is kept at a constant size of 750µm, which is more than 4 times the size of the micro-capsule. At each of the 3 volume fractions of the MP-RVEs, 6 realizations with different micro-structure were generated to account for the randomly placed micro-capsules. The number of capsules in each MP-RVE is calculated using Equation (3.1) where volume fraction, f, diameter of inclusions, D, and size of RVE, a, are known parameters. The positions of inclusion are also randomly generated based on Random Sequential Adsorption (RSA) algorithm as followings. The first inclusion is generated randomly in the RVE domain. When the inclusion $(n+1)^{th}$ is added randomly into the domain containing n inclusions, intersections between n+1 inclusions are checked. If there is any inclusion intersection, the inclusion $(n+1)^{th}$ will be regenerated. The procedure to generate the inclusion $(n+1)^{th}$ is repeated until there is no any intersection between n+1 inclusions.

All RVEs are subjected to both periodic material conditions and periodic boundary conditions, which are identical to those in the study on porous epoxy presented in Chapter 3.

4.3.2.2. Material models

The matrix is modelled as a homogeneous material and its crack-softening behaviour is simulated using the smeared crack model, in which values for the inputs of Young's modulus and ultimate stress are given in row 1 of Table 4.1, corresponding to f=0%. The constitutive law of the matrix epoxy is approximated by a bi-linear stress-displacement curve with the maximum crack opening displacement of 4.03μm calculated using Equation (3.5).

In fact, as shown in Section 4.2, micro-capsules can be modelled as a Neo-Hookean core in an enclosed shell. However, incorporating such a model of capsules into RVE, especially MP-RVE, approach with damage will raise to a very expensive computational cost. Also, it may also encounter with difficulties due to the closely singular of stiffness matrix in Neo-Hookean material, whose Poison's ratio is very close to 0.5. In the current study, the fluid-filled micro-capsules is proposed to modelled as voids with the consideration that the micro-capsule is more than three orders of magnitude softer than the matrix, as determined in the preliminary study. This simplification can only be valid for the elastic response but cannot be extended to the post-elastic response due to the shear-yielding effect of the micro-capsule. The shear-yielding effect can be accounted for by introducing shear retention in the smeared crack model of the matrix. Researchers have found that the conventional shear retention model with constant shear retention factor, ρ, does not agree well with results from experiments (Kolmar et al., 1984; Rots and Blaauwendraad, 1989). The reason is because the shear retention model with constant ρ does not take into account the relationship between the reduction in shear resistance of a damaged area and its degree of damage. In reality, the effectiveness of a crack to transfer the shear stress

across the crack will decrease with increasing crack strain (de Borst R., 2002). To

overcome this, a shear retention model with variable ρ has been proposed (Rots and

Blaauwendraad, 1989) which is expressed mathematically as follows:

$$G_{cr} = \rho G \tag{4.3}$$

$$\rho = 1 - \frac{\varepsilon_{cr}}{\varepsilon_{max}} \qquad \text{for} \quad \varepsilon_{cr} \leq \varepsilon_{max} \tag{4.4a}$$

and $\quad \rho = 0 \qquad\qquad\qquad \text{for} \quad \varepsilon_{cr} > \varepsilon_{max} \tag{4.4b}$

where, G and G_{cr} are initial shear modulus and cracked shear modulus, respectively;

$\quad$ ρ is shear retention factor;

$\quad$ ε_{cr} is the direct strain across the crack;

$\quad$ ε_{max} is a user-defined parameter corresponding to the state when ρ is fully

$\quad\quad$ reduced to 0.

4.3.2.3. Loading condition and other numerical issues

All the RVEs are discretized using 4-node tetrahedral elements with

reasonably fine mesh, typically an average of 800 000 elements are used for MP-

RVEs to maintain ensure accuracy in the computed stresses. The RVEs are subjected

to displacement-controlled uniform traction on two opposite faces. The mechanical

properties of the virgin SHM, which include Young's modulus, strength and fracture

toughness, are calculated from the load-displacement response of the RVE following

the same procedure described in Chapter 3. The healed properties of the SHM are

subsequently investigated by replacing the damaged elements obtained from the

previous step with new elements that represent the cured healing agent.

4.3.3. Prediction of Young's modulus and strength

The effective Young's modulus obtained from simulations and from experiments (Brown et al., 2004) are plotted in Figure 4.4 and tabulated in Table 4.2 for comparison. The predictions from both SP-RVE and MP-RVE approaches follow the trend of diminishing Young's modulus with increase in the volume fraction of micro-capsules. Similar to the results presented in Chapter 3, the effective Young's modulus predicted from SP-RVE model is less accurate than that from MP-RVE model in comparison with experimental results. The SP-RVE approach provides good prediction with less than 10% of error for low volume fractions of $f = 6\%$ and 11% whereby the interactions between capsules is weak.

The volume fraction of 17% for the capsule can be considered as small based on Drugan and Willis' criterion and the deviation of the predicted E_{eff}, using SP-RVE model, from the experimental value is slightly higher than 10%, at 10.71%. This is because of the simplification of the capsules as voids which omit the small contribution of the capsules' liquid core on the overall response of the composite. For the same reason, the predicted elastic responses at all varying f, using both SP-RVE and MP-RVE approaches, is softer than those obtained in real experiments.

Table 4.2: Effective Young's modulus of micro-capsule based SHM

Properties	Vol. % of micro-capsules	Experimental data (Brown et al., 2004)		SP-RVE prediction			MP-RVE prediction		
		Mean	Standard deviation	Mean	Standard deviation	Error	Mean	Standard deviation	Error
Effective Young's modulus (GPa)	0	3.4	0.1	3.4	-	-	3.4	-	-
	6	3.2	0.1	3.1	0	-3.13%	3.1	0.01	-3.13%
	11	3.1	0.2	2.8	0	-9.68%	2.9	0.01	-6.45%
	17	2.8	0.1	2.5	0	-10.71%	2.6	0.01	-7.14%
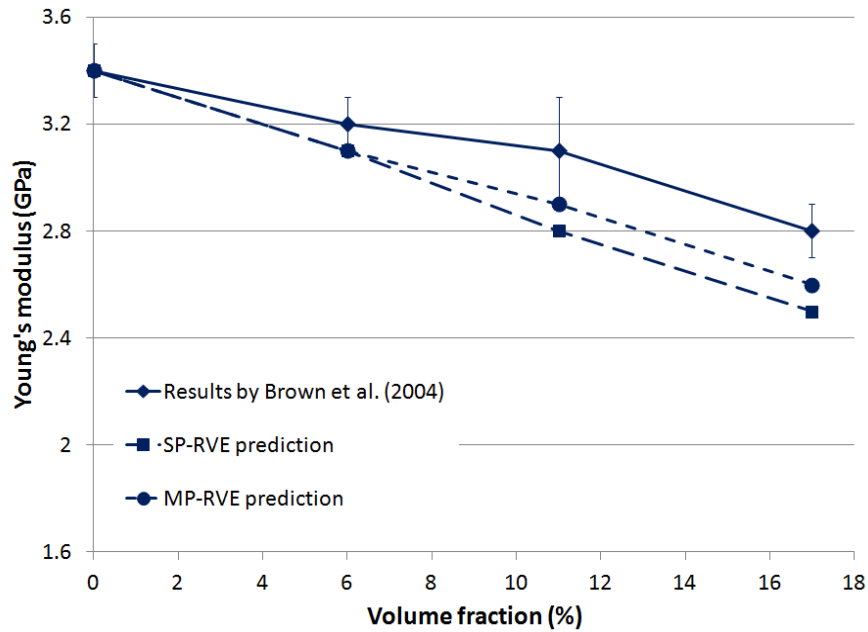
Figure 4.4: Effective Young's modulus obtained from RVE approaches and experiments

It is noticeable in Figure 4.4 that the predictions appear to be lines but in fact, it only reflects a small portion of a curve, which describes the relationship between effective Young's modulus and volume fraction. This pseudo-linear trend in the case of small volume fraction of inclusions is also reported for other theoretical models predictions (Wang et al. 1999).

The MP-RVE model fitted well with the experimental data with an error of less than 10% for volume fractions of micro-capsules less than 17%. This result suggests that the proposed simplified model for micro-capsule is adequate for the elastic properties of micro-capsule based SHM. In addition, the small standard deviations in the predicted Young's moduli using MP-RVE also implies that 6 realizations for each volume fraction of capsule are adequate for the selected size of the MP-RVE to provide accurate prediction of E_{eff}.

Figure 4.5 presents the comparison between the numerical predicted strengths and the reported experimental strengths. As expected, the predictions from RVE approaches exhibit trends of diminishing effective strength when the capsules content is increased, which is also observed from experiments. The reason for these trends, quite obviously, is because the introduction of much weaker particles into a host matrix will reduce the ultimate stress capacity of the host matrix.

In general, MP-RVE approach is able to provide better predicted values. However the effective strength predicted using SP-RVE approach is closer to the reported experimental value at f=11%, compared to the prediction using MP-RVE approach. On the other hand, the accuracy of the reported strength of SHM with 11% volume fraction of micro-capsules, is questionable as it is equal to the strength of SHM at f=17%.
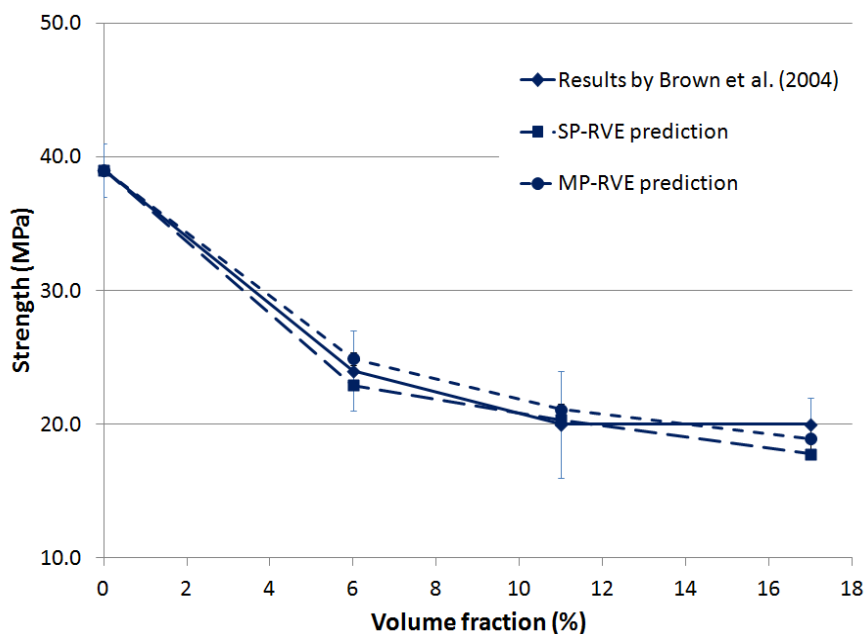
Figure 4.5: Effective strength obtained from RVE approaches and experiments

The mean and standard deviation of the experimental determination of SHM's

strength and their numerical predictions are tabulated in Table 4.3. The standard

deviation of the experimental $\sigma_{f,\ eff}$ at $f=11\%$ is higher than the corresponding values of

$\sigma_{f,\ eff}$ at $f=6\%$ and 17%, which suggests that the measurements in experiments with

11% of capsules is less reliable. This is likely the reason for a longer deviation of the

MP-RVE approach as compared to the SP-RVE approach at $f=11\%$.

Table 4.3: Effective strength of micro-capsule based SHM

Properties	Vol% of micro-capsules	Experimental data (Brown et al., 2004)		SP-RVE prediction			MP-RVE prediction		
		Mean	Std. dev.	Mean	Std. dev.	Error	Mean	Std. dev.	Error
Strength (MPa)	0	39	2	39.0	-	-	39	-	-
	6	24	3	22.9	0	-4.58%	24.9	0.49	3.75%
	11	20	4	20.3	0	1.65%	22.11	0.45	10.55%
	17	20	2	17.8	0	-11.10%	18.92	0.89	-5.40%

Table 4.3 shows that the prediction of effective strength using MP-RVE model

fits well with the experimental data with an accuracy of around 90% or above and

falls within the standard deviation of the experimental data. Again, this result

validates the assumption that there is negligible contribution of micro-capsules on the

overall strength of the SHM. Similar to the prediction of effective Young's modulus,

the standard deviation of the predicted strength using MP-RVEs are very small, which

shows that the number of realizations used in MP-RVE approach is sufficient.

4.3.4. Prediction of healing efficiency

Healing efficiency, η, is defined by Brown et al. (2004), as a ratio of the

recovered and the virgin fracture toughness.

$$\eta = \frac{K_{IC,healed}}{K_{IC,virgin}}$$

(4.5)

where $K_{IC,virgin}$ and $K_{IC,healed}$ are virgin and recovered fracture toughnesses, respectively, of SHM.

It is obvious from equation (4.5) that to provide a good prediction on healing efficiency, both $K_{IC,virgin}$ and $K_{IC,healed}$ have to be captured. As reported by Brown et al. (2004), crack reopened after healing and the layer of cured healing agent bore the re-applied stress. In other words, the recovered fracture toughness depends only on a single phasic material, namely, cured healing agent, which can be easily modelled.

On the other hands, predicting the fracture toughness of micro-capsule based SHM is much more complicated and required a detail study on toughening effect of micro-capsules, which is out of the scope of the present study the present study, the input for shear retention model ε_{max} is calibrated for different volume fraction of capsules.

4.3.4.1. Calibrating ε_{max} for virgin fracture toughness

In shear retention model with variable shear retention factor, the input is the maximum strain, ε_{max}, across the crack corresponding to the state when ρ is fully diminished, as shown in Equations 4.4. As the matrix toughening is attributed to the micro-capsules, the degree of shear yielding effect varies with the volume fraction of the micro-capsules, f, and therefore, the degree of shear retention also has to vary with f. In the current study, the input ε_{max} for each volume fraction of micro-capsules was varied to determine the best fit to the experimental values at all reported values of f. It

was noted that the shear retention model is only applicable for MP-RVEs, in which

the crack surface is non-planar and tortuous. For the case of SP-RVE, the crack,

cutting across the narrowest section of the RVE, is perfectly planar and perpendicular

to the applied load. As the result, there is no shear on the crack surface, which also

means no effect of shear retention.

Results of simulations with MP-RVEs show that values of ε_{max} to provide the

closest capture of fracture toughness are 0.3, 2.0 and 8.0 for SHM with f=6%, 11%

and 17%, respectively. Shear retention factors, when elements are fully damaged,

corresponding to ε_{max} = 0.3, 2.0 and 8.0 are 0.10, 0.77 and 0.85, respectively.

Kotsovos and Pavlovic (1995) believed that a reasonable shear retention factor to be

used in smeared crack model should not be larger than 0.5 to ascertain the physically

realistic of aggregate interlocking effect. However, the above comment is based on

the authors' observations and experiments on concrete, where aggregate interlock is

considered as the mean to transfer shear stress after cracking. For the polymers, cross-

links, instead of aggregate interlocking, play important role in stress transferring and

shear yielding effect (Kinloch et al., 1987; Pearson and Yee, 1989; and Bagheri et al.,

2009). Thus, comments on meaningful shear retention factor of Kotsovos and

Pavlovic (Kotsovos and Pavlovic, 1995) may not be correct for the current study.

The numerically simulated fracture toughness and its error compared to the

reported experimental data are tabulated in Table 4.4, in which the toughening

phenomenon of micro-capsule based SHM was captured, at the accuracy level of

95%, using MP-RVE approach. The confidence interval of fracture toughness

obtained through numerical simulations is smaller than that obtained through reported

experiments confirming the sufficiency of number of realizations used in this study.

Contradict to the results from both MP-RVE model and experimental data, the fracture toughness captured by SP-RVE approach, where shear retention is meaningless, exhibits a diminishing trend of K_{IC} as the content of micro-capsules increases. These results further confirm the role of shear retention to describe shear yielding effect in the proposed model for micro-capsules SHM.

Table 4.4: Effective fracture toughness of micro-capsule based SHM

Properties	Vol% of micro-capsules	Experimental data (Brown et al., 2004)		MP-RVE model		SP-RVE model	
		Mean	ε_{max}	Mean	Error	Mean	Error
Fracture toughness (MPa.m$^{1/2}$)	0	0.55	-	0.55	-	0.55	-
	6	0.78	0.3	0.75	-3.85%	0.41	-47.44%
	11	1.14	2.0	1.10	-3.51%	0.37	-67.54%
	17	1.20	8.0	1.18	-1.67%	0.32	-73.33%

The results of simulations and the reported experiments (Brown et al., 2004) reveal the fact that the toughening degree of SHM, through shear yielding effect, increases with a raise in capsules concentration. This result is also observed in rubber-modified systems (Becu et al., 1997; He et al., 1999). It is believed that inter-phase zone existing between soft particles and polymer matrix is a factor controlling the toughness of rubber-toughened epoxies (Chen and Jan, 1991; Bagheri and Pearson, 1995). Through experimental observations, those researchers claimed that ductile inter-phase between rubber inclusions and epoxy matrix improves plastic dilation around the particles leading to an increase in fracture energy of the composite (Chen and Jan, 1991; Bagheri and Pearson, 1995). The idea of inter-phase zone can also be used for a reasonable explanation of *brittle-to-tough* zone observed experimentally by Margolina and Wu (Margolina and Wu, 1988). As the content of the soft inclusions

increase, the total volume of inter-phase zones will also increase resulting in the raise

in fracture toughness of the composites, as can be seen with micro-capsule based

SHMs. It is recommended to conduct a further investigation in the future on effect of

shear yielding on toughening capability of micro-capsule based SHM.

4.3.4.2. Capturing healing effect

Since SP-RVEs are inadequate for the modelling of the fracture behaviour of

micro-capsule based SHM, only the MP-RVEs are used for the prediction of fracture

toughness recovery of SHM. Figure 4.6 demonstrates a three-step process carried out

on each MP-RVE model to simulate healing effect of SHM as following.

Step 1: Multiple realizations are carried out with MP-RVE models to

determine the fracture toughness before healing, which is named as virgin fracture

toughness, $K_{IC,virgin}$.

Step 2: Damaged elements, whose tensile strain in crack direction exceed the

maximum tensile strain, in fracture zone in each MP-RVE are identified and replaced

by new elements possessing material properties of healing agent. In other words, the

process of healing is not modelled by the curing of the healing agent in this study but

instead, the changes in state are tracked.

Step 3: Healed MP-RVEs are subjected to periodic boundary and loading

conditions that are identical with those in step 1 to characterize the recovered fracture

toughness, $K_{IC,healed}$. Healing efficiency, η, is calculated using equation 4.5.
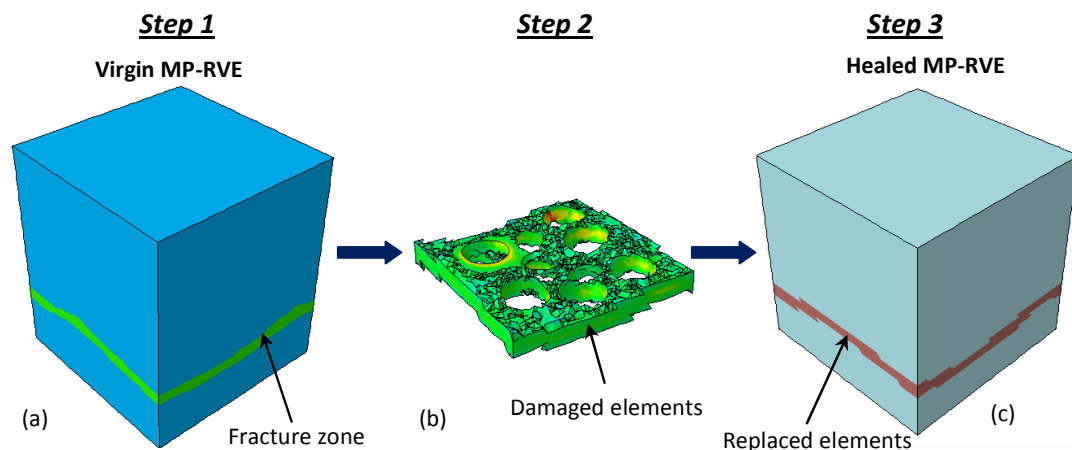
Figure 4.6: Steps to capture healing efficiency of micro-capsule based SHM: (a) Determine $K_{IC,virgin}$ from virgin MP-RVEs; (b) Identify damaged elements and replace them with new elements; (c) Determine $K_{IC,healed}$ from healed MP-RVEs to find healing efficiency η.

As discussed in Chapter 3, two material inputs for a bi-linear smeared crack model are strength, σ_f and maximum crack opening displacement w_{max} but these were not reported in literature. For this reason, we derive the material properties for hardened healing agent from results of a study carried out by Brown et al. (2002) to characterize the healing efficiency of micro-capsule based SHM using tapered double cantilever specimens shown in Figure 4.7.
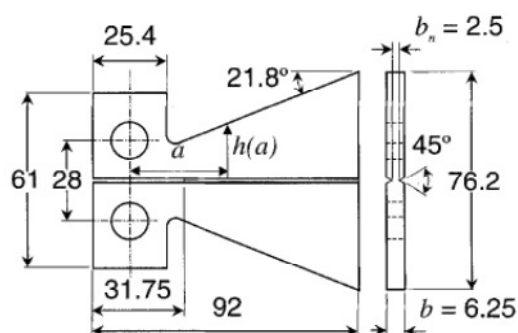
Figure 4.7: Tapered double cantilever beam K_{IC} characterization of micro-capsule based SHM (after Brown et al., 2002)

Only result for SHM with 6% vol. fraction of capsules was reported and it was
shown that the critical load of the specimen after healing was reduced to be 88% of its
critical load at virgin state. Taking note that the geometry of the virgin and the healed
specimens are exactly the same geometry and the critical load applied on a double
cantilever beam is linearly proportional to the average stress ahead the crack tip (J.M.
Whitney, 1985), the strength at the healed crack, $\sigma_{f,healed}$, can be estimated to be 88%
of that of the SHM when $f = 6\%$:

$$\sigma_{f,healed} = 0.88 \text{ x } 22 = 21 \text{ MPa} \tag{4.6}$$

By fitting the numerically predicted fracture toughness $K_{IC,healed}$ to the
experimental values obtained by Brown et al. (2004), we obtain a value of 6.0µm for
the maximum crack opening displacement $w_{max,HA}$. The fitting results are presented in
Table 4.5, in which the maximum error is less than 10%.

Table 4.5: Healed fracture toughness of micro-capsule based SHM

Vol% of micro-capsules	Calibrated $w_{max,HA}$ (µm)	Experimental data (Brown et al., 2004) (MPa.m$^{1/2}$)	Captured $K_{IC,healed}$ (MPa.m$^{1/2}$)	
		Mean	Mean	Error
0	4	-	0.00	
6	6	0.53	0.58	9.43%
11	8	0.55	0.60	9.09%
17	12	0.66	0.65	-1.52%

Figure 4.8 compares healing efficiency of micro-capsule based SHM obtained
from numerical simulations and from experiments. As be shown, maximum healing
efficiency of SHMs is about 80%, occurring at low concentration of capsules, $f=6\%$.
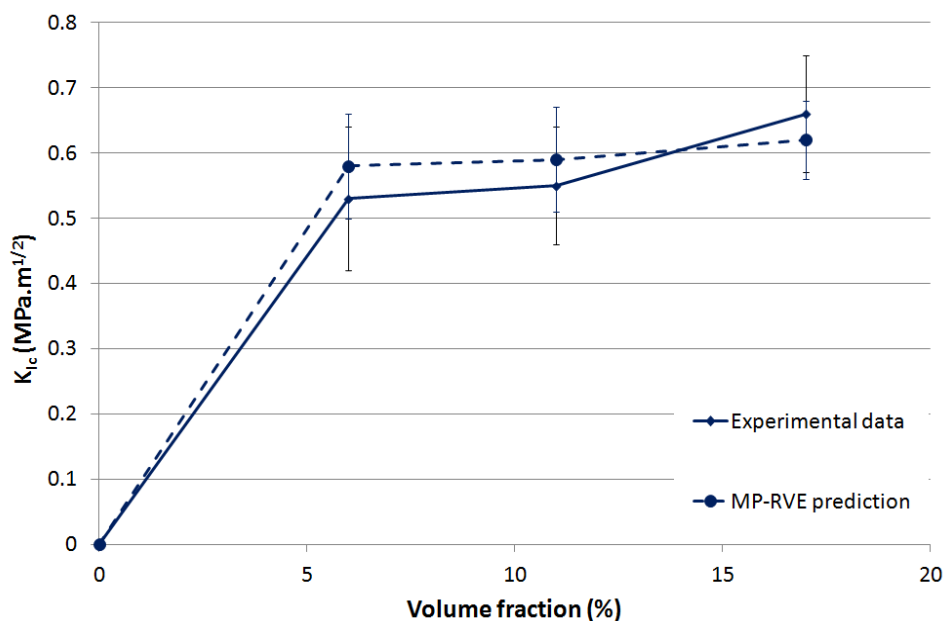
Figure 4.8: Healing efficiency of micro-capsule based SHM: numerical prediction versus experimental data

Recalling Equation 4.5, $K_{IC,virgin}$ is significantly contributed to η as virgin fracture toughness is the referenced to calculate healing efficiency. For the case of micro-capsule based SHM, there is a sharp increase of $K_{IC,virgin}$, at 46%, when volume fraction of capsules increases from 6% to 11%. Meanwhile, there is just a slight increase at only 4% when f rises from 6% to 11%. As a result, the healing efficiency drop rapidly from f=6% to f=11%. The increase rate of $K_{IC,virgin}(f$=17%) compared to $K_{IC,virgin}(f$=11%) is almost the same as the increase rate of $K_{IC,healed}(f$=17%) compared to $K_{IC,healed}(f$=11%), resulting a plateau in the η - f curve shown in Figure 4.8.

Since SHM with 6% volume fraction of capsule has higher strength and Young's modulus than both SHMs with f=11% or 17%, 6% volume fraction may be the optimum content of micro-capsule if Young's modulus, strength, and healing

efficiency are controlled parameters for optimized process of SHM. However, if fracture toughness is the priority parameter, f=17% is the most favourable solution because this volume fraction of capsules offers the highest value for both virgin and healed fracture toughness of SHMs. Those results are just preliminary observations from experiments and numerical simulations. Further study is recommended for a comprehensive optimized design for micro-capsule based SHM.

4.4.   NUMERICAL SIMULATION OF STRUCTURAL BEHAVIOUR OF SELF-HEALING BEAMS

The influence of healing effect on structural behaviour of a self-healing specimen is studied in this session using a self-healing beam subjected to a three-point bending test as a numerical example. The simulation is carried out firstly for the self-healing composite, proposed by Brown et al. (2004), using 6% volume fraction of 180μm-diameter microcapsules. It is noted that the strength of cured healing agent in SHM proposed by Brown et al. (2004) is lower than the strength of the host matrix. To investigate effect of the strength of healing agent, additional simulation with self-healing beam using healing agent possessing higher strength, compared to host matrix, is performed. Lastly, a simulation with self-healing beam using tubular system, where the healing is only activated for severe cracks, are considered to make comparison with self-healing beam using encapsulated system.

4.4.1. Numerical set up

The numerical model is set up in 2D using 8-node quadrilateral elements as shown in Figure 9a.
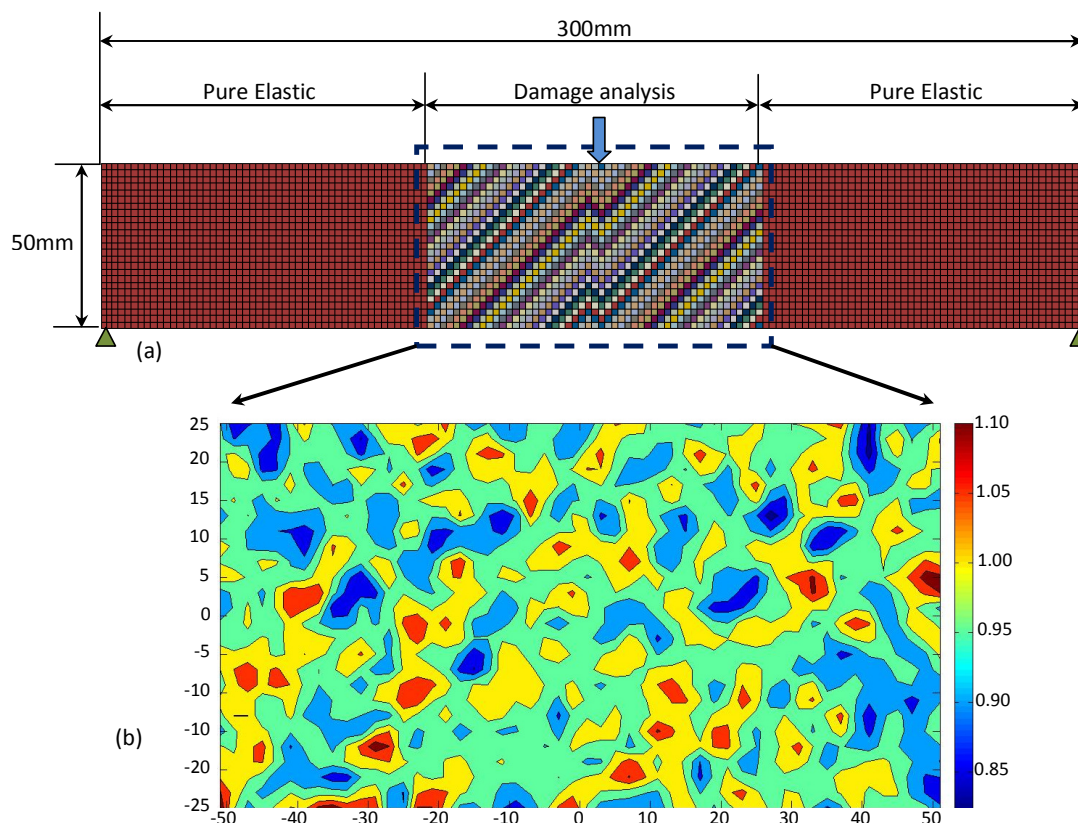
Figure 4.9: Numerical set up of self-healing beam: (a) 2D Beam model; (b) contour plot of normalized strength of elements in the critical zone.

The beam is divided into three equal parts, among which damage analysis using smeared crack model is applied only at the middle part to capture the fracture behaviour of the beam while the rest are modelled as pure elastic regions. Values for the inputs of Young's modulus, for all parts, and of fracture toughness, for the middle part, are the mean value of E_{eff} and $G_{f,eff}$, respectively, of SHM embedded with 6% vol. fraction of micro-capsules. To simulate the effect of inhomogeneity, each element in the middle part is assigned with a random strength generated from the normal distribution, whose mean and standard deviation are 24MPa and 3MPa, respectively. The strength assigned for each element is normalized by the mean value and plotted in Figure 4.9b.

Three series of simulations are carried out in this Section, namely simulations with reference beam, self-healing beam using capsulated system, and self-healing beam using tubular system. The simulations with reference beam are to provide information on structural behaviour of a beam that does not possess healing capability. The simulations with self-healing beams are to simulate effect of healing on structural behaviour of the beam. In the simulations with self-healing beam using capsulated system, all cracks are repaired, while in the simulations with self-healing beam using tubular system, only critical cracks, whose length is larger than a threshold value representing the location of self-healing units, are healed. Similar to Section 4.3.5, healing is simulated by replacing damaged elements with new elements possessing material properties of cured healing agent.

In all simulations, the beam is subjected to displacement control loading at its mid-point and the corresponding force is calculated as sum of reactions at the supports. For the sake of more obvious comparison between beams with and without healing effect, normalized force and normalized stiffness are used. The normalized reaction force is calculated as a ratio of reaction force to the beam's maximum load capacity, which is found from the simulation with reference beam; while the normalized stiffness is a fraction of the secant stiffness to the reference beam's initial stiffness.

4.4.2. Simulation with reference beam

The order of crack appearance in the reference beam is presented in Figure 4.10a-c. At first, there were 3 cracks named as Crack 1, Crack 2 and Crack 3. As can be seen in Figure 4.10b, Crack 1 and Crack 2 propagated from weak elements at the

bottom of the beam while a very weak element close to the bottom of the beam,
whose strength is only 78% of the average strength of the material, created a local
stress concentration that initiates the growth of Crack 3. Compared to the other two
cracks, Crack 2 is easier to evolve because both Crack 1 and Crack 3 are obstructed
by strong elements that lie near to the bottom of the beam. For this reason, at later
stages of the simulation, damage in the beam was localised at Crack 2, i.e. Crack 2
continued to develop while the rest closed up, as shown in Figure 4.10c.
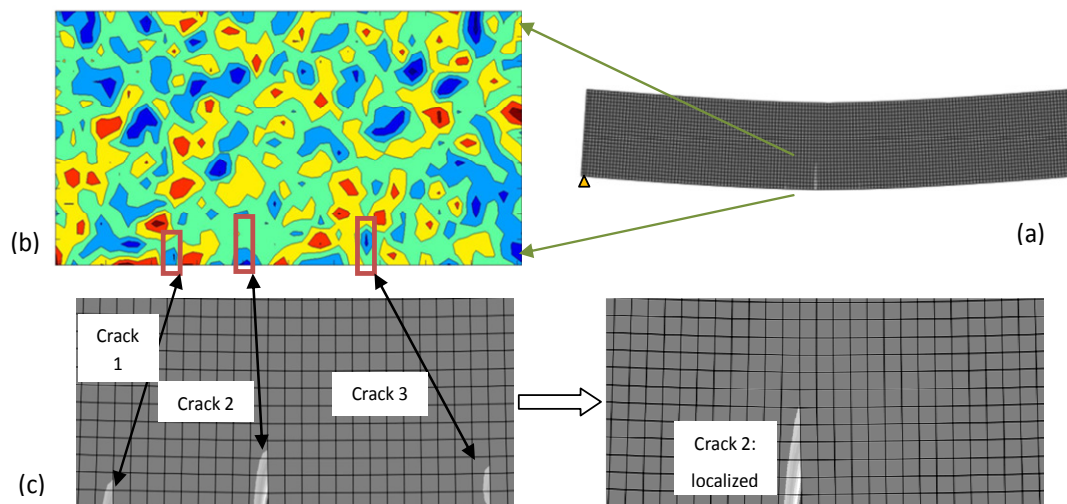
Figure 4.10: Results from simulation of reference beam: (a) deformed shape; (b) location of
cracks in strength contour map; (c) damage localization;

Figure 4.11a and 4.11b show normalized plots of the reaction force and secant
stiffness, respectively, of the reference beam as a function of the applied
displacement. It can be seen from Figure 4.11b that when the applied displacement
was 0.12mm, the beam's stiffness started to decrease, signifying damage initiation in
the beam. In the beginning, a number of small cracks were initiated and energy was

dissipated in all of these cracks resulting in a gradual decrease in secant stiffness.

When the applied displacement was 0.22mm, damage and the dissipation of energy

were localized in the growth of Crack 2. The evolving rate and also the beam damage

rate increased dramatically leading to a sudden dip in the secant stiffness of the beam.

The maximum load was attained at a displacement of 0.257mm with a corresponding

loss of 9.5% of the secant stiffness. At maximum displacement, the beam's

normalized secant stiffness and force were 0.855 and 0.958, respectively.
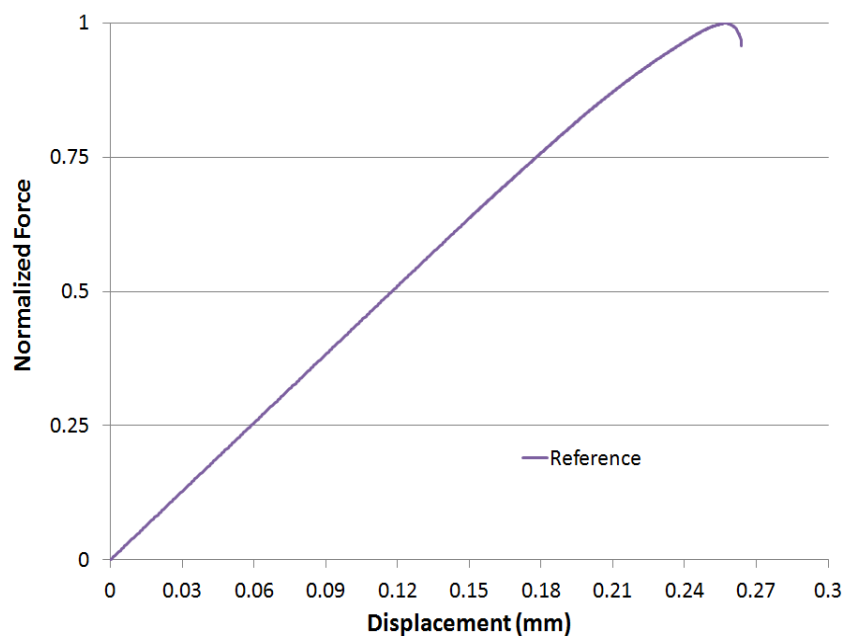
Figure 4.11a: Structural behaviour of reference beam - normalized force vs. displacement
             plot
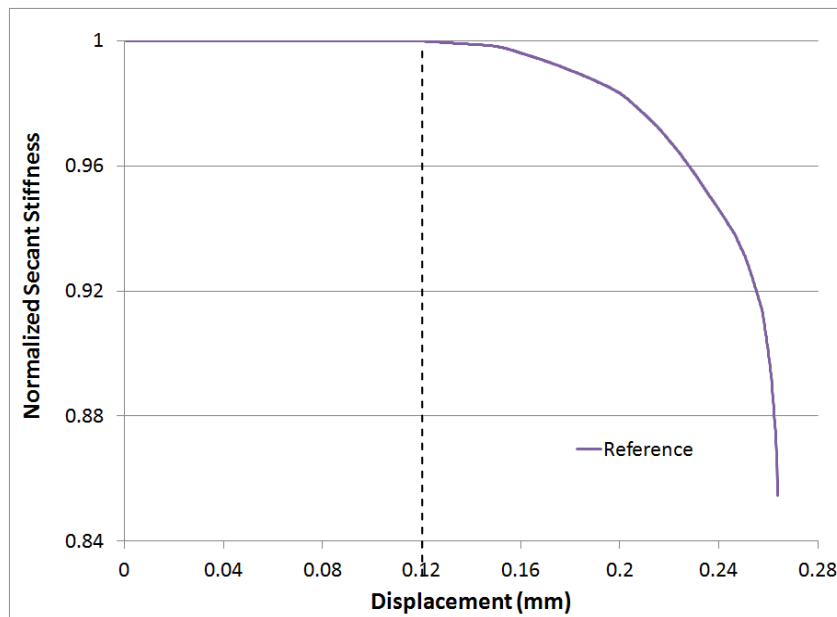
(b)

Figure 4.11b: Structural behaviour of reference beam - normalized secant stiffness vs.
displacement plot.

4.4.3. Simulation with self-healing beam using capsulated system

The loading procedure for self-healing beam using capsulated system is as
follows. First, the beam was loaded until a displacement of 0.26mm, at which the
localized crack propagated through one quarter of the beam depth, was applied. At
this stage, the beam was under softening regime and damage was localising in Crack
2, as described in Section 4.4.3, and its normalized stiffness was reduced to 0.9. Then,
the beam was unloaded and all damaged elements along Cracks 1, 2 and 3 were
replaced by healed elements, whose material-wise inputs are given by properties of
cured healing agent.

As estimated in Section 4.3.4, cured healing agent in the micro-capsule based
self-healing system that was first proposed by White et al. (2001) is weaker than the

surrounding matrix. Mending a crack with an adhesive weaker than the structure's material is not effective since a crack filled with a weaker material will re-introduce stress concentration and will reopen. Crack reopening in a self-healing structure is undesirable, especially when the healing is to restore strength, prevent/retard further crack growth or reduce permeability due to damage. For these purposes, healing agents possessing higher strength compared to the structure's material are more preferable (Dry, 1996).

In the current section, effects of healing cracks by strong and weak materials are compared through two types of micro-capsule based self-healing beams. The first beam, named as "capsulated system – low strength" beam or CS-LS beam, is to capture the healing effect of the micro-capsule based SHM proposed by White et al. (2001). In the simulation with CS-LS beam, strength of healed elements equals to 88% of the mean value of original elements' strength, as estimated in Section 4.6. The second beam, named as "capsulated system – high strength" beam or CS-HS beam, is to investigate the scenario where micro-capsule based system using high strength healing agent is used. In the simulation with CS-HS beam, strength of healed elements equals to 120% of the mean value of original elements' strength. For both beams, Young's modulus of the original elements and the healed elements are identical.

Figure 4.12 illustrates the critical zone of the Capsulated Based Self-Healing beams, where Cracks 1 and 3 did not reopen after healing, in both beams. For the CS-LS beam, Crack 2 reopened as expected. As shown in Figure 4.12a, a new Crack 2 was initiated at element 3765, which is an element neighbour to the original Crack 2 and is weaker than healed elements. Because the strength of element 3764 is much higher than that of healed elements, it becomes an obstacle for the crack development;

and thus, the new Crack 2 chose an easier path to propagate, namely reopening healed

elements.
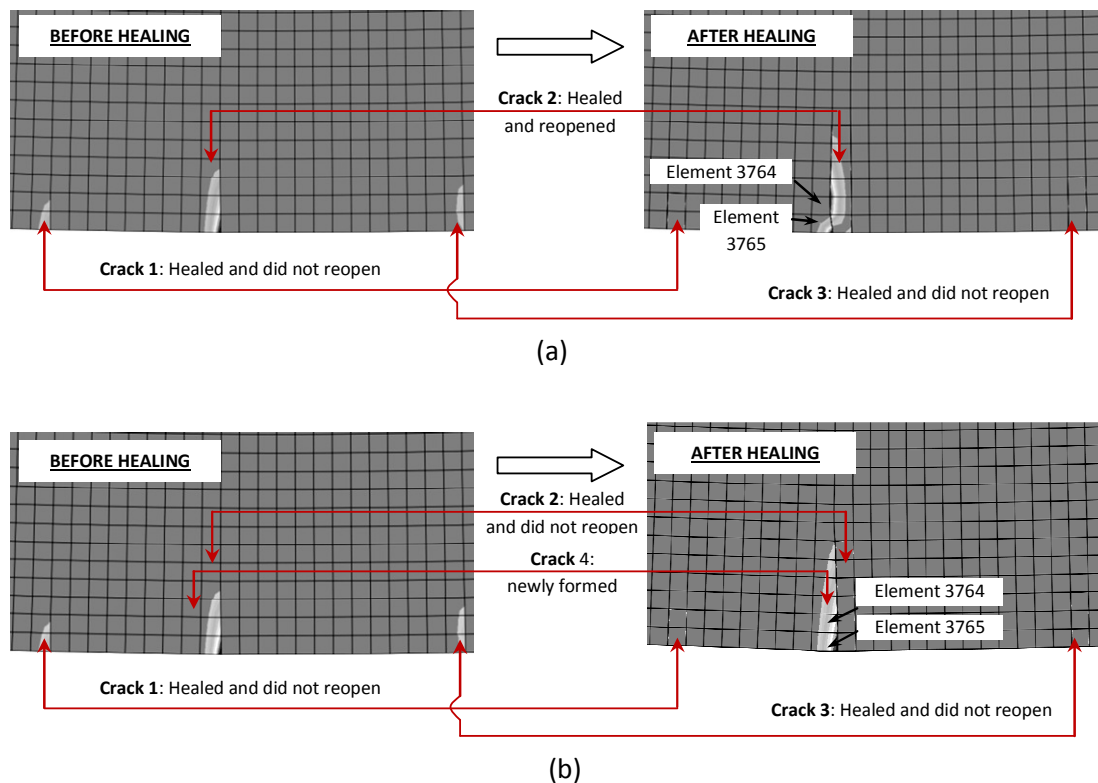
Figure 4.12: Before and after healing states at critical zone of self-healing beam using capsulated system: (a) CS-LS model; and (b) CS-HS model.

In contrast, there was no crack reopening in the simulation with CS-HS beam,

where a new crack was also initiated at element 3765. However, since the strength of

healed elements is larger than that of element 3674, the easier path for the crack

propagation becomes cracking through element 3674. Consequently, Crack 4 was

newly formed.

The effect of crack reopening on healing efficiency, in terms of recovered

beam's load capacity, as presented in Table 4.6. It is obvious that crack reopening in

the beam embedded with capsulated self-healing systems using low strength adhesive results in an inability to fully recover the beam's load capacity. On the contrary, when high strength adhesive is used to prevent crack reopening, the beam's load capacity after healing is increased. In the current numerical example, the CS-HS beam is able to recover to 102% the load capacity after healing.

Table 4.6: Results from simulations with CS-LS and CS-HS beams

Beams	Loading		Unloading		Reloading	
	Normalized load capacity	Normalized stiffness	Normalized load capacity	Normalized stiffness	Normalized load capacity	Normalized stiffness
CS-LS	1.00	1.00	-	0.90	0.85	0.97
CS-HS	1.00	1.00	-	0.90	1.02	0.97

The healing efficiencies of self-healing beams in CS-LS and CS-HS beams are also quantified using stiffness recovery as tabulated in Table 4.6. As the Young's moduli of healed elements in both simulations with Capsulated Based Self-Healing beams are identical, there is no difference in stiffness recovery of CS-LS and CS-HS beams. Results of the simulations show that after healing, initial stiffness of the self-healing beam is able to recover to 97% of its original stiffness.

4.4.4. Comparison with self-healing beam using tubular system

In the simulations in Section 4.4.3, all cracks are healed to simulate the scenario that micro-capsules are distributed in the whole critical zone and cracks at any length will rupture the capsules to release healing agent. That scenario is not true

for the case of self-healing structures using tubular system in civil engineering applications, where the tubes are concentrated at a certain location only. In those self-healing structures with tubular system, the healing is only activated for severe cracks, whose length is over the level where the tubes are embedded. To make comparison on the healing effect of the above two systems, simulations with self-healing beam using tubular system, named as TS-HS, are carried out in this Section. The loading procedure is identical to that for CS-HS beam with the assumption that healing system is activated only by cracks whose length is one quarter of the height of the beam. For this assumption, only Crack 2 was healed. The material properties of healed elements in simulations with CS-HS and TS-HS beams are the same, i.e. healed elements are stronger than original ones. Simulations of self-healing beam using tubular system with low strength healing agent are not carried out because it is predictable that Crack 2 will reopen and such a beam will behave similarly to the CS-LS beam.

As can be seen in Figure 4.13, during the reloading procedure, the healed Crack 2 did not open while the unhealed Cracks 1 and 3 reopened. Because elements 1472 and 3473 at the tips of Cracks 1 and 3, respectively, are much stronger than element 3765, a newly formed Crack 4 was initiated at element 3765 and then propagated upwards. At later steps of the simulation, damage in the beam was localised at Crack 4.
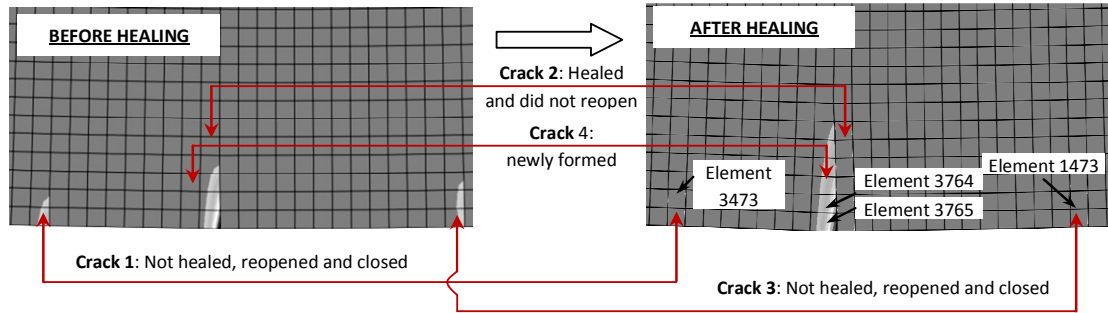
Figure 4.13: Cracks appearance in TS-HS beam for the first healing

Results from the simulations with CS-HS and TS-HS beams are tabulated in Table 4.7, where both beams are able to recover to 102% the beam's load capacity. As can be seen, the difference between healing effects in TS-HS beam and CS-HS beam is in the recovered stiffness. Because damaged elements in all the three Cracks 1, 2 and 3 were replaced by healed elements in simulation of the beam using capsulated self-healing system, the CS-HS beam is able to recover more, in terms of stiffness, than the TS-HS beam, where only damaged elements in Crack 2 were replaced.

Table 4.7: Results from simulations with CS-HS and TS-HS beams

Beams	Loading		Unloading		Reloading	
	Normalized load capacity	Normalized stiffness	Normalized load capacity	Normalized stiffness	Normalized load capacity	Normalized stiffness
CS-HS	1.00	1.00	-	0.90	1.02	0.97
TS-HS	1.00	1.00	-	0.90	1.02	0.95

A further investigation on the difference between two self-healing systems was conducted by simulating the second healing in CS-HS and TS-HS beams. The

loading procedure is as follows. After being healed the first time, two beams were reloaded until a displacement of 0.26mm was applied, at which Crack 4 propagated to one quarter of the height of the beam. Then, the beams were unloaded and damaged elements in Crack 4 were replaced by the healed ones. Finally, displacement at the mid-point of the beams was reapplied to model the second reloading procedure.

The difference in damage developments in CS-HS and TS-HS beams during the second healing test are shown in Figure 4.14a and b, respectively. After the second healing for Crack 4, the easiest path for the damage development in the beam is to continue from Crack 3; and that is the path of damage to evolution in TS-HS beam. However, this path was pre-prevented in the capsulated self-healing beam as Crack 3 was healed during the first healing. As a result, for the CS-HS beam, damage was evolved through a newly formed Crack 5, which required higher energy compared to the reopening Crack 3 path. Because a higher energy is required to develop the damage in the CS-HS beam, its maximum load capacity after the second healing is higher than that of the TS-HS beam. This is evidenced by Figure 4.14c, where the recovered maximum load capacity of the CS-HS and TS-HS beams are 106.4% and 103.5%, respectively.

Figure 4.14d shows that both self-healing beams are able to recover stiffness after healing and the healing efficiency, in terms of stiffness recovery, of the CS-HS beam is higher than that of the TS-HS beam. The main reason is because capsulated self-healing system is able to heal all cracks while only severe cracks are healed if tubular self-healing system is used. Actually, this result is only correct in an ideal scenario where there is no constraint on the limit of healing agent ready to flow to the cracks.

(a)

(b)

(c)
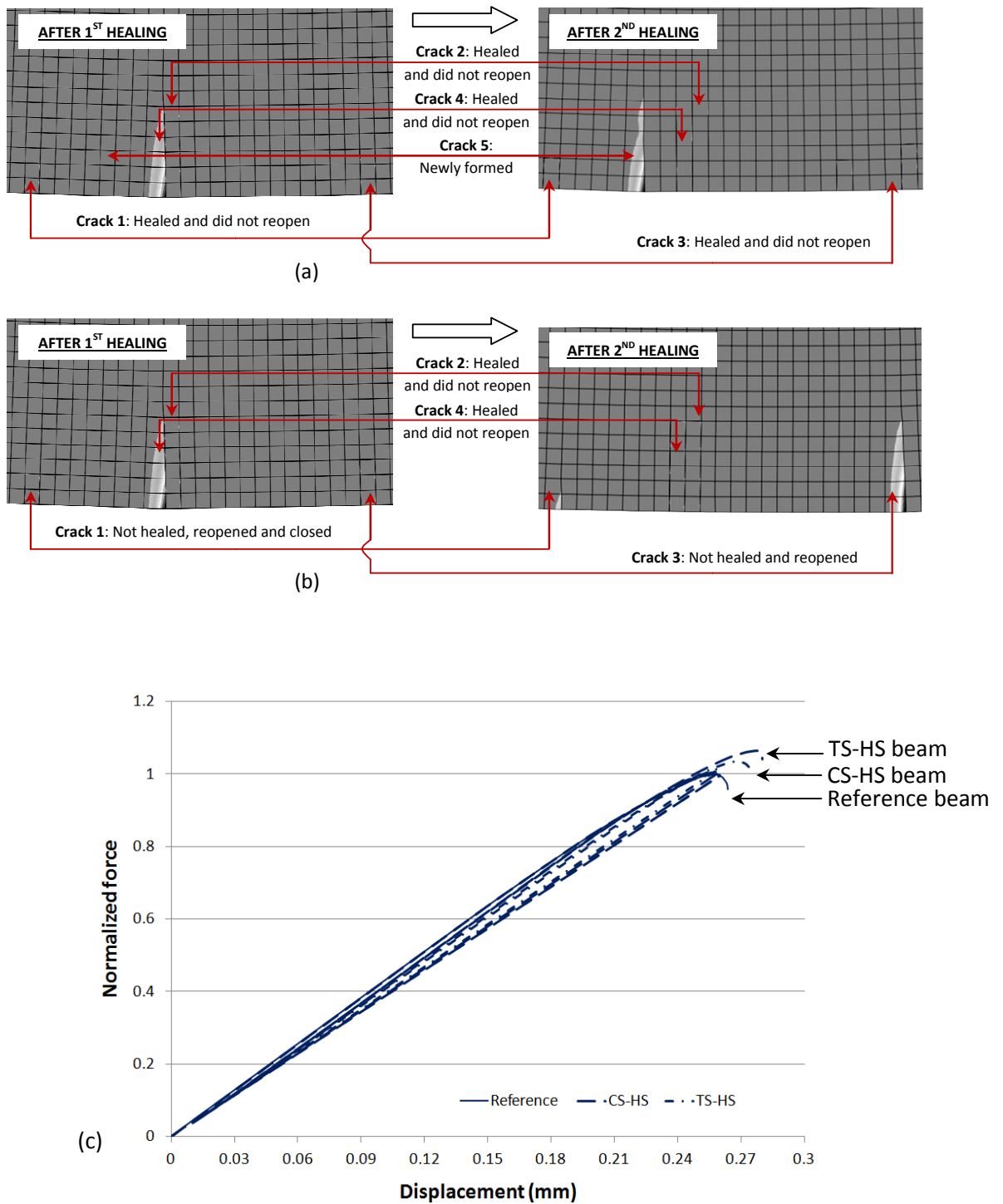
Figure 4.14a-c: Results of simulations of self-healing beams after the 2nd healing: (a) damage evolution in CS-HS beam; (b) damage evolution in TS-HS beam; (c) normalized force-displacement curves
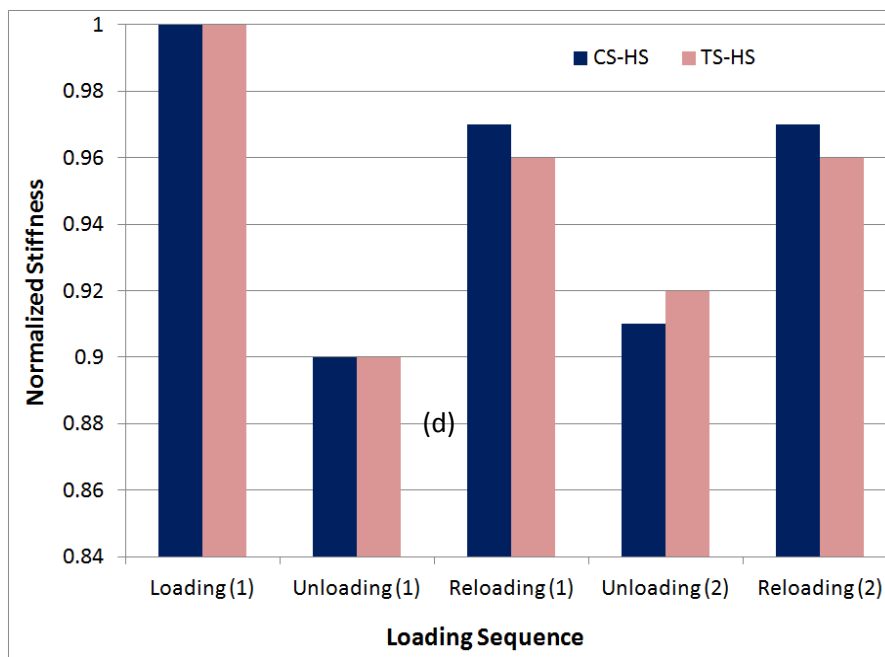
Figure 4.14d: Results of simulations of self-healing beams after the 2nd healing: (d)
normalized stiffness in all loading sequences

4.5.   SUMMARY

The material response and structural behaviour of micro-capsule based self-
self-healing material is simulated in this Chapter. Firstly, the elastic behaviour of
micro-capsules is investigated in the preliminary study using a biphasic model. It
comprises of a linear elastic material model for the capsule wall and a hyperelastic
neo-Hookean material model for the enclosed liquid healing agent. The model reveals
that the capsules are orders magnitude softer than the matrix to have any significant
contribution to the elastic response of the composite.

Secondly, RVE approaches are adopted to simulate mechanical response of
SHMs, containing 6% to 17% volume fraction of micro-capsules, and predict their
healing efficiency. In all RVEs, the capsules are modelled as voids and the shear
yielding effect in the matrix offered by the capsules is modelled by introducing shear

retention in the smeared crack model adopted for the matrix. For the elastic behaviour of the SHMs, the simulations show that MP-RVE approach can predict well the elastic behaviour of the SHM with the maximum error of 7.1% and 5.5% for the predictions of Young's modulus and of strength, respectively. SP-RVE approach is also able to predict both Young's modulus and strength of the SHMs; but at a lower accuracy of less than 11.5% of error, compared to MP-RVE approach.

To predict the healing efficiency of SHMs, a three-step procedure is proposed, in which the virgin fracture toughness of SHMs is modelled based on the calibration of the input ε_{max} of the shear retention model. It was found that only MP-RVE approach is suitable for the prediction of healing efficiency of SHMs as the shear retention model is inapplicable for the SP-RVE.

By replacing damaged elements in MP-RVEs with new elements that represents for cured healing agent, simulations are carried out to predict the healing efficiency. Compared to the published experimental data, the proposed model is able to generate good prediction, at less than 10%, of error for the healing efficiency of the SHM.

Lastly, a macro size self-healing beam subjected to three-point bending is numerically modelled to investigate the effect self-healing material on structural behaviour. The simulated effective properties of micro-capsule based SHM are fed into the model as inputs value. Random strengths are assigned for elements at the critical zone of the beam to model the inhomogeneous effect. The numerical model shows that using healing agent that is weaker than the beam's material will limit the healing effect, in terms of recovery of the maximum load capacity. In contrast, if strong healing agent is used, it is possible to induce the beam's load capacity.

Additional simulations with beams using tubular healing system, in which only severe

cracks are healed, show that ideally, capsulated system may offer better recoveries in

both stiffness and load capacity.

CHAPTER 5

APPLICATIONS OF SELF-HEALING CONCEPT IN CIVIL ENGINEERING

5.1.   INTRODUCTION

Although recent studies on self-healing materials are strongly focused on composites for high-tech applications in space and aeroplane areas, the idea of self-healing function was first investigated in civil engineering field with the study by Dry (1992) for cementitious materials. However, only in recent years, when the topic of sustainable materials is getting hotter and hotter, self-healing concrete has been an attractive topic as a possible solution for sustainability problem.

As a specific type of self-healing materials, self-healing concrete is also considered as a potential way out for damage problems. As the most common building material in the world, there are so many civil structures made of concrete. Any untimely remedy for the damage of these structures, especially bridges and buildings, can easily lead to a sudden collapse and may result in drastic consequences, not only for economics but also for human life. Unfortunately, there are many circumstances where damage in concrete structure may not be detected and repaired easily such as cracks deep inside the element or cracks in invisible positions. If self-healing function is implemented in concrete structure, damage propagation may be

stopped or postponed to provide valuable time for overhauling or evacuation and hence, severe losses can be prevented.

Classifying by techniques to create self-repairing function in concrete, there are two types of self-healing concrete namely, autogenous self-healing and autonomic self-healing ones.

5.1.1. Autogenous self-healing concrete

The main idea of autogenous self-healing concrete is to activate the hydration of unhydrated cement particles dispersed in the concrete structure to gain strength and stiffness. Indeed, the natural autogenous healing of cementitious materials has been well known for many years and it is acknowledged as one of the reasons for the survival of many old buildings and structures. Observations from the existing bridges built in the 18th century in Amsterdam, Roman aqueducts in Italy and Gothic churches in England reveal that cementitious materials are able to self-heal when moisture interacts with unhydrated cement clinker in the crack (Edvardsen, 1999). The main cause of this magnificent ability is attributed to the dissolution and re-precipitation of calcium carbonate within the lime-based mortar matrix.This re-precipitation happens on the surface of cracks, resulting in the crack-sealing and the reduction in permeability of the mortars (Jonkers and Schlangen, 2008).

Numerous researches have been carried out in recent years to explore the effect of various parameters, including of freeze-thaw cycles, temperature, crack width, and material age, on the amount and the rate of autogenous healing. Jacobsen and Sellevold (1996) examined concrete cubes damaged by rapid freeze-thaw cycles

and found that concrete cubes stored in water bath were able to recover compressive strength. Reinhardt and Loos (2003) found that higher temperature and the smaller cracks will lead to a faster healing rate. Ter Heide (Ter Heide et al, 2006) observed that autogenous self-healing is especially effective for early-age cracks. Pimienta and Chanvillard (2004) noticed that autogenous healing phenomenon also exists in ultra high performance concrete specimens reinforced by steel fibers and organic fibers for cracks that have crack width smaller than 300µm. Researches by Victor Li and colleagues at University of Michigan (Li. 2003; and Yang et al., 2009) have established the condition on crack width to achieve autogenous healing function in cementitious composites. They claimed that tight crack width, typically from 50µm to 150µm, is essential to ensure quality self-healing. Crack width of maximum 50µm is necessary to achieve full recovery of mechanical and transport properties, whereas partial recovery can only be attained for crack width of 50µm to 150µm. This requirement on crack width can be satisfied by using Engineered Composite Concrete (ECC), which uses fly ash and metal fibers to control the development of micro-cracking and prevent the damage localization.

Different methods have been used to activate the autogeneous healing process such as using temperature (Farage et al., 2003), natural water containing dissolved carbon dioxide (Cowie J. and Glassert F.P., 1992), water pressure (Nanayakkara A., 2003) and bacteria (Ramachandran et al. 2001; Ghosh et al. 2005; De Muynck W. et al., 2008; Jonkers, H.M., 2007, 2009). Amongst them, studies using bacteria to create bio-concrete have attracted the attentions of researchers from different countries such as Belgium (Van Tittelboom et al., 2010), Netherlands (Jonkers, H.M., 2007, 2009) and Japan (Kishi et al., 2007). Good results, in terms of crack sealing and increasing the water permeability ability, have been achieved as shown in Figure 5.1. However,

there is no report on the recovered strength or load capacity of the tested specimens after damage.
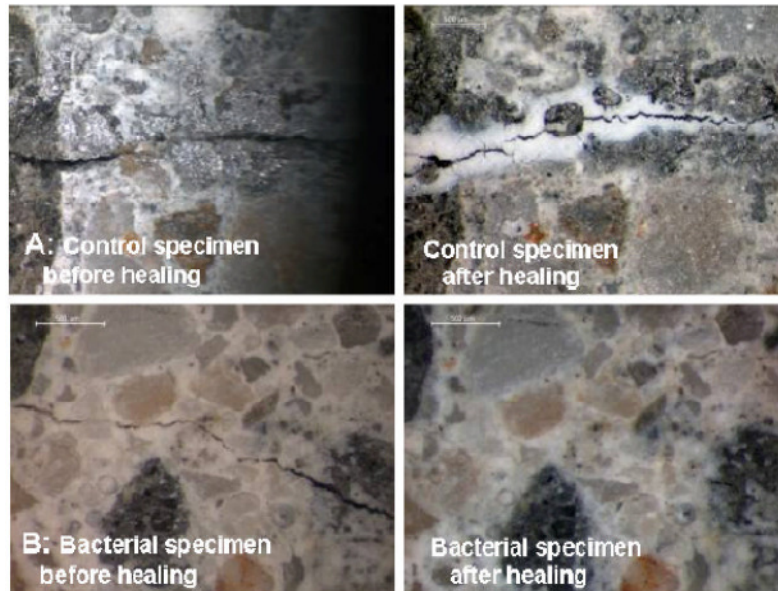
Figure 5.1: Bacteria-based self-healing concrete (after Jonkers H.M., 2007).

5.1.2. Autonomic self-healing concrete

Autonomic self-healing concrete shares the same concept with other artificial self-healing composites: self-healing function is created by embedding self-healing units comprising of the container and the healing agent in the host concrete. The first research on autonomic self-healing concrete was carried out by Dry (1992) using hollow glass tubes as containers and methyl methacrylate as healing agent. Afterwards, Dry and her colleagues (Dry, 1994; Dry and Mc Millan, 1996), Li et al. (1998) and Joseph et al., (2007) adopted this method to examine healing efficiency, in terms of recovered strength and flexural stiffness, of autogenous self-healing beams using lab scale specimens that are shorter or equals to 300mm. The detail literature

review of these researches can be found in Chapter 1 with the notice that all of them used tubular system to establish self-healing ability.

In recent years, there are interests in using micro-encapsulating system for self-healing concrete. The use of microcapsules to create self-healing function in cementitious materials was first investigated by Yang et al. (2009, 2011). In this study, microcapsules with oil core and silica gel shell were constructed by using methyl methacrylate monomer and triethyl borane as healing agent and catalyst. The microcapsules were dispersed in fresh cement mortar along with carbon micro-fibers to create self-healing mortar. Experiment results showed some enhancements in compressive strength of self-healing mortar. Autonomic repairing at room temperature yielded as much as 45% recovery of virgin fracture toughness while repairing at 80^0C increased the recovery to over 80%. Adopting the similar idea, chemical researchers in University of Rhode Island have embedded 2% volume fraction of micro-encapsulated sodium silicate healing agent into concrete matrix and found that the healing mix was able to recover 26% of its original strength (Science Daily, May 25, 2010).

Another approach is to employ the Shape Memory Alloy (SMA) as reinforcement for concrete. This study was carried out by Song and Ma (2006) and generated the concept of Intelligent Reinforced Concrete (IRC). IRC uses martensite SMA wires for post-tensioning, which resistance change can be used to monitor strain distribution inside the concrete. When crack occurs, the heated SMA wires cause the contraction which decreases crack width and restores concrete specimen into its initial form. Hence, this method has the ability to detect and heal cracks. Adopting the same ideas, as illustrated in Figure 5.2, researchers in Cardiff University (Jefferson et al., 2007, 2010) proposed the cementitious-shape memory or cementitious polymer

composite system to improve the durability of cementitious materials. The self repairing of cracks will prevent the ingress of harmful substances such as carbon dioxide in the air and chloride ions from sea water, which leads to reinforcement corrosion, degradation of material properties and a shortened lifespan of the structure. However, there are human interventions in its healing process, such as heating the tendons for the contraction. Therefore, this system cannot be considered as a fully self healing composite.
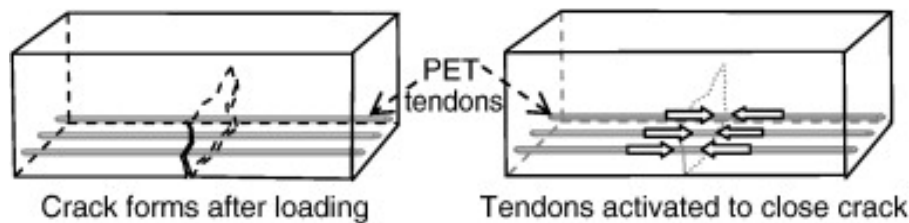
Figure 5.2: Crack closure system using shrinkable polymer tendons (Jefferson et al., 2010).

5.1.3. Remarks

Although numerous studies have been carried out on autogenous self-healing concrete with good results in the improvement in permeability, there are disadvantages for this method. First of all, there are various environmental and damage conditions, such as crack width, water pressure and environmental temperature, pH, water chloride concentration, have to be tailored to ensure the occur of the autogenous self-healing process. However, those factors are not easy to control and need a high level of monitoring and thus, quality control of autogenous self-healing concrete is still a challenge. On top of that, autogeneous self-healing will only

effective in an ample supply of unhydrated cement, particularly in low water-cement ratio concrete. This will limit the applications of autogenous self-healing concrete.

Compared to autogenous self-healing concrete, autonomic self-healing concrete is more reliable and not much dependent on the surrounding environment. Among three techniques used to create autonomic self-healing concrete, namely using tubular system, using microcapsules and using shape memory alloy, the method with shape memory alloy is not a fully automatic process. For the other two, tubular system is more preferable than micro-encapsulating system because the former one offers 3 main advantages as following:

i) In tubular system, self-healing units are concentrated and hence, protecting tubular self-healing units from pre-mature damages during concrete casting process is simpler. In contrast, as many microcapsules should be used to provide self-healing function, finding a method to protect them from pre-mature damage is almost impossible.

ii) Since self-healing units using hollow glass tubes is sizeable, it is possible to position them in structural members. As this task is impossible for micro-capsulated system, micro-capsules may float up and position at uncritical zones.

iii) The hollow glass tube is commercialized and easily found from the market while the microcapsules have to be produced from laboratories. As a result, self-healing unit using tubular system is more economic than that uses micro-capsules.

Another important remark drew from the literature review is most of researches on self-healing concrete are at the stage of conceptual proof on beam elements made of mortar or non-aggregate cementitious materials. As an illustration, Li and Yang (2007) used ECC specimens at the size of 230x76x13mm; Jonkers (2008) experimented with concrete bars of dimensions 160x40x40mm; Nishiwaki et al. (2006) utilized mortar specimens at size 320x60x20mm, Song and Mo (2003) demonstrated their theory with mortar specimens of dimensions 343x152x51mm.

While autonomic self healing approach appears as a great potential approach, it remains a great challenge to extend this idea from small-scale mortar specimens to large-scale concrete structural elements, in which the slower dissipation of heat generated during curing, the impact by the coarse aggregates during casting impact and the vibration of the concrete for compaction may cause the undesirable premature damage to the self-healing units.

This Chapter focuses on the implementation of autonomic self-healing function in large scale structural reinforced concrete members. Firstly, preliminary studies on the selection of self-healing unit components including of healing agent and container, along with proof-of-concept experiments to illustrate the effectiveness of the chosen self-healing unit components are presented in Section 5.2. Implementation issues of self-healing system in structural members including of methods to protect healing unit during casting process are also discussed in this Section. Next, the protected self-healing systems are implemented at structural scale for of the three essential structural elements namely beam, column and slab. The experimental set up and results for those structural elements are discussed in Section 5.3, 5.4 and 5.5, respectively. Finally, Section 5.6 summarizes the whole Chapter.

5.2.   PRELIMINARY STUDIES

5.2.1. Selection of healing agent and storage system

The self-healing functionality in concrete, which uses damage to trigger the healing process, relies heavily on the selection of two main components namely, the adhesive and the hollow tubes, both of which have to fulfil the following requirements:

a. The adhesive used for self-healing system in concrete must have a low viscosity, in the range of 100-500cps as recommended by ACI (1992), in order to flow within the confined crack space. The bond strength between the adhesive and the concrete should be larger than that of concrete and the adhesive must cure sufficiently fast to resist cracks from re-opening. There are currently 1-part and 2-part adhesives in the market. The 2-part adhesive comprises an adhesive base and a hardener and they have to be mixed properly in adequate proportions to ensure proper bonding. The latter may be difficult to be met since the two parts must be presented in separate containers embedded in the concrete. In addition, using 2-part healing agent will causes the difficult in activate healing procedure timely as both of containers need to be ruptured to activate the healing agent. Hence, the 1-part adhesive, which contains latent hardener, is preferred as the healing agent for embedded systems.

b. The hollow tubes used as the storage system must not react with concrete and the adhesive. The tubes must remain thermally stable during casting as well as when the structure is in-service. The tubes should be small enough so as not to cause significant changes to the overall properties of structure, but they should be large enough to transport sufficient amount of healing agent to the crack surfaces. The selection of the tube wall thickness plays an important role in the control of the

initiation of tube breakage. A thin wall may cause the tube to rupture before the crack reaches it whereas with a thicker wall, the fracture of the tube may not be timely to cause the release of adhesive to heal the cracks.

c. In concrete applications, both the adhesive and the hollow tubes have to remain intact during the casting process, which means the properties of the adhesive should not be altered by heat generated during curing and the hollow tubes should not be damaged by vibration and impact of aggregates.

In view of the aforementioned requirements, several adhesives were first chosen based on manufacturers' information on the viscosity, curing conditions, shelf-time and bond strength with concrete. A 1-part adhesive Isocyanate Prepolymer (commercial name is POR-15) with a low viscosity of 250-500cps was used. The material safety data sheet of POR-25 is shown in Appendix 1. The curing process is initiated upon contact with air at ambient condition and the hardened adhesive achieves a tensile strength of 22MPa when fully cured, which is higher than the tensile strength of normal concrete.

Perspex and glass hollow tubes were considered for the storage system. Observations from perspex and glass tubes filled with Isocyanate Prepolymer indicated that after 24 hours under indoor condition, visible cracks on the surface of perspex tubes were formed as shown in Figure 5.3a, while no cracks were found on the glass tubes. Beside the chemical reaction between the perspex tubes and the Isocyanate Prepolymer causing the aforementioned visible cracks, the higher strength and ductility of perspex delay the rupture of the tubes (Johnson, 2008). Glass is therefore sufficiently inert when used with the proposed Isocyanate Prepolymer adhesive.
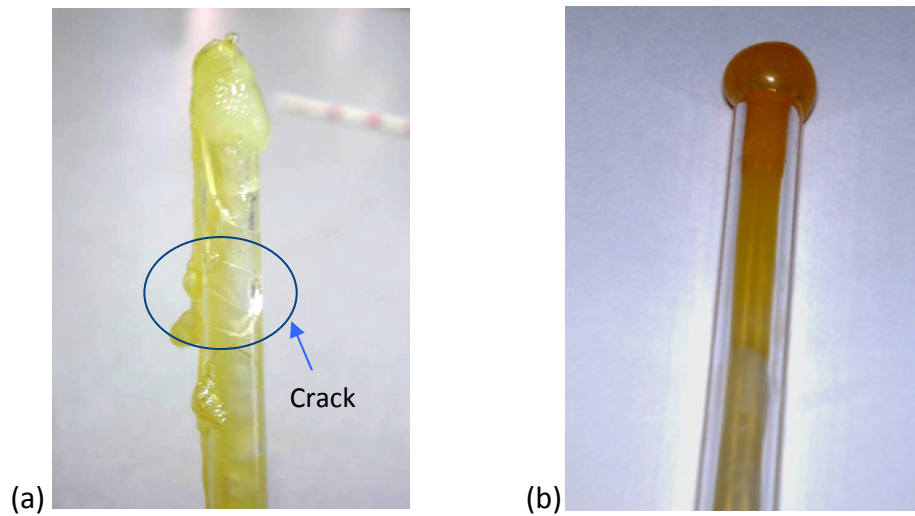
Figure 5.3: Encapsulation of Isocyanate Prepolymer using: (a) Perspex tube; (b) Glass tube

In order to investigate the effect of concrete curing temperature on the adhesive and hollow glass tubes, the encapsulated adhesive-filled glass tube was immersed in a Memmert waterbath. As a reference, Burg and Ost (Burg and Ost, 1994) measured the temperature rise of a high-cement-content 1.2-meter test cube and found that temperature at the center of the cube reached the peak of 55°C to 65°C after 2 days of curing. In the current preliminary study, the temperature of the waterbath was set of 65°C to 77.5°C over a period of 8 days and the tube containing Isocyanate Prepolymer showed no visible cracks on its surface. Also, the Isocyanate Prepolymer did not harden. The encapsulated Isocyanate Prepolymer was then injected to a small sample of cracked mortar specimens. After 24 hours, these specimens were subjected to a 3-point bending test, to investigate whether the Isocyanate Prepolymer healing agent is able to be used to seal the cracks. It was found that the bonding strength of the heated Isocyanate Prepolymer and the mortar is still higher than the tensile strength of the mortar, which was indicated by a new crack formed at a position in proximity to the old one.

Tests were also conducted to investigate the appropriate size of hollow glass tubes, using 2 groups of tubes, named as Group A and Group B, with inner diameter (ID) and outer diameter (OD) respectively are: ID=3mm, OD=5mm and ID=4mm, OD=6mm.

Two sets of steel-mesh-reinforced mortar beams with dimensions of 300mm x 80mm x 50mm, each containing two identical empty tubes from one tube group, were subjected to three-point bending test until the crack penetrated through almost half of the specimen depth. To determine the instant when the tubes cracked, strain gauges were attached on the glass tubes. After cracking the specimen, Isocyanate Prepolymer was injected manually into the hollow glass tubes using syringe. Observations showed that for all specimens, the leakage of adhesive into the crack was observed, implying that tubes in Groups A and B did crack. However, pumping the adhesive into hollow tubes in Group A was much more difficult than into the ones in Group B due to the larger surface tension associated with the smaller inner diameter. The first occurrence of fracture in the glass tubes was indicated by a sudden surge in strain measured by the strain gauge, accompanied by an audible "pop" sound. This event was preceded by the cracking of concrete which happened less than 10 seconds earlier.

Additional tests for tubes in Groups A and B were carried out to see if the adhesive from the rupture tube can be drawn upwards to the crack tip under capillary action, and also flow down towards the bottom surface of the beam under gravity. This test was identical to the previous ones except that the tubes were pre-filled with Isocyanate Prepolymer and sealed at the ends.

It is noticeable that sealing the filled adhesive glass tube was one of the difficulties encountered due to the reaction between the sealant and   Isocyanate

Prepolymer. Various sealants were tried with the glass tube. Using silicon and araldite to seal ends of the adhesive-filled glass tubes produced unsatisfactory results. The chemical reaction happened between these sealants and the adhesive produced air bubbles, which pushed the adhesive upwards causing leakage as shown in Figure 5.4. However, when Diglycidyl Ether of Bisphenol A, whose commercial name is Aquastick, was used to seal the ends, no leakage was observed even after a few days, indicating its suitability. Material Safety Data Sheet of Aquastick is attached in Appendix 2.
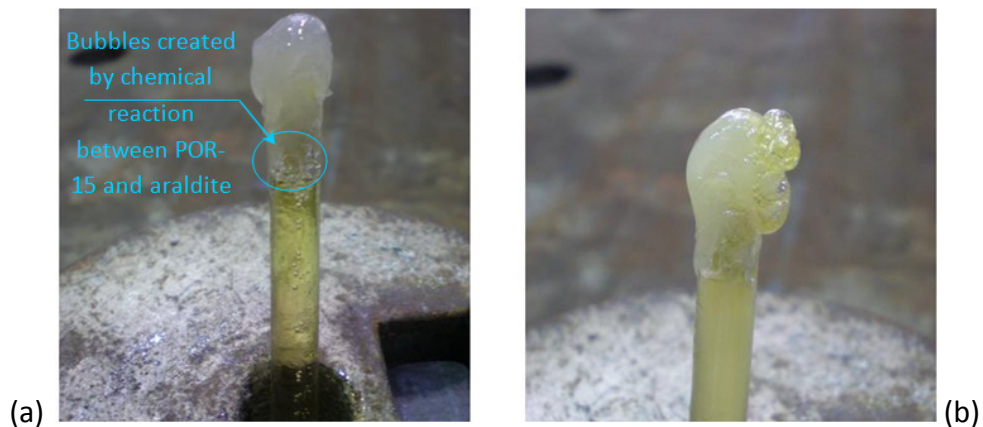
Figure 5.4: Leakage of adhesive when araldite was used as sealant: (a) 30 minutes after sealing; (b): 1 day after sealing

The mortar beams were also loaded until the visible crack tip approached the mid-depth of the beam. Observations showed that for beams containing tubes in Group B, the Isocyanate Prepolymer can virtually fill the entire crack planes from the bottom surface of the beam to the crack tip, whereas for the ones containing tubes in group A, there was no sign of adhesive leakage on the bottom surface of the beam even after the crack tip has reached the upper quarter of the beam height. The crack mouth opening at the time when the crack tip approached the middle level of the

beams was about 0.3µm. After dissecting the specimens containing the smaller tubes in group A, it was found that the adhesive only filled a small region around the rupture zone due to the large surface tension of the small tube that prevented the adhesive from flowing. For a comparison study, additional steel-mesh-reinforced mortar specimens, each containing one tube in Group A and another one in Group B, were also subjected to the three-point bending test. As it can be seen in Figure 5.5, part of the crack surfaces was filled by the leaked adhesive from the larger tube while no leakage was found in the area embedded with the smaller tube.
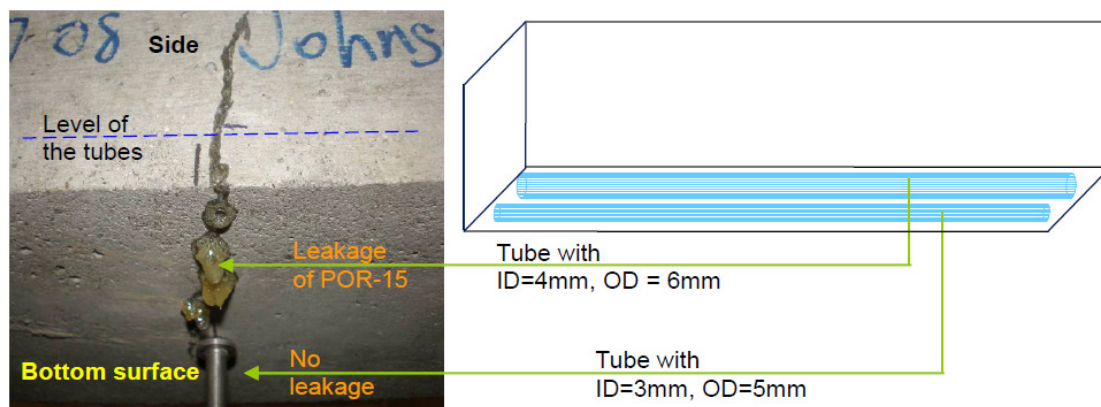
Figure 5.5: Testing for the leakage of ISOCYANATE PREPOLYMER using tubes in Groups A and B

In summary, the preliminary tests for selection of healing agent and container indicate that the suitable components of self-healing system for concrete are (a) 1-part adhesive Isocyanate Prepolymer and (b) hollow glass tube with ID=4mm and OD=6mm. This combination will be used for the proof-of-concept tests.

5.2.2. Proof-of-concept experiments

For artificial functionalized material to exactly mimic nature's self-repairing mechanism, it must be truly autonomic, with no manual intervention needed. It is thus necessary to experimentally test the autonomic bleeding of Isocyanate Prepolymer adhesive. Adhesive-filled glass tubes sealed at both ends were embedded in the tensile zone of the steel mesh reinforced mortar specimens. In addition to bleeding, the healed specimen must regain a significant portion of its original strength. This was experimentally done by comparing the strength of healed specimens against the control specimens which do not contain the self-healing system. The subsequent cracking of the healed specimen upon re-loading was also investigated.

5.2.2.1. Materials and specimens preparation

Mortar specimens of size 300mm x 80mm x 50mm (denoted as set D) were cast using a mortar mix of 0.41:1:1 (i.e. water: OPC: sand), each of which were embedded with two glass tubes of length = 250mm, inner diameter = 4mm and outer diameter = 6mm. The tubes were filled with Isocyanate Prepolymer using aquastick to seal both ends. They are placed at a depth of 10mm from the bottom of the specimen while the steel wire mesh (1.3mm diameter at 12mm spacing) was placed at 20mm from the bottom of the specimen. The horizontal distance between the tubes was 25mm as shown in Figure 5.6. A similar set of specimens (set C) but without the glass tubes was cast to serve as control specimens. All specimens were compacted using a vibrating table, demoulded after 24 hours and dried in air for 3 days before tests were carried out.
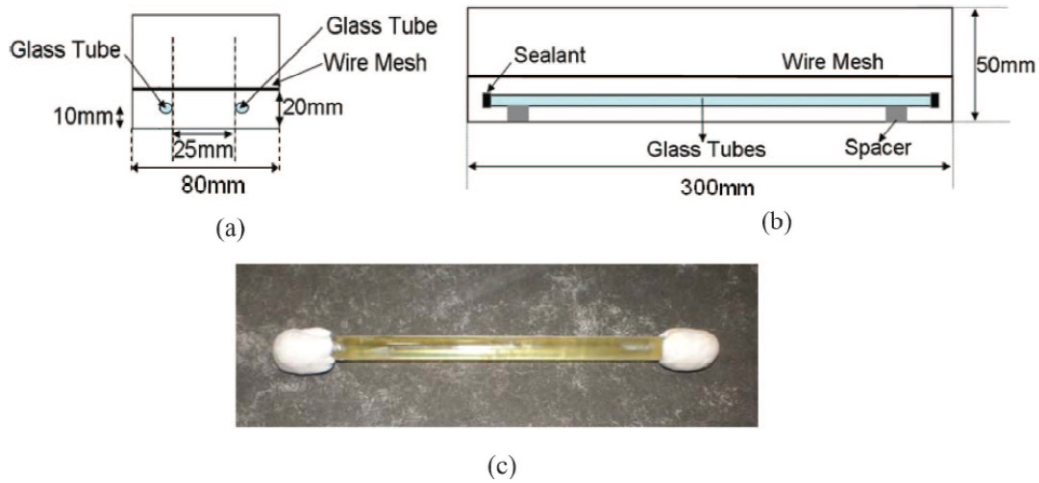
Figure 5.6: Self-healing system for autonomic bleeding test: (a) front elevation; (b) side view; (c) adhesive-filled glass tubes with aquastick as sealant

5.2.2.2. Test procedure

All specimens were subjected to three-point bending test, using the Instron Testing Machine, at 0.2mm/min. The control specimens (set C) were loaded to failure to determine the load-displacement curve. Each specimen in set D was tested beyond the point where an audible 'pop' sound was heard, which indicated fracturing of the glass tube. The load was held until leakage of the adhesive was observed on the bottom surface of the specimen. The specimen was then unloaded and left unloaded for 4 days before being loaded again using the same displacement rate. The test was terminated soon after more leakage of Isocyanate Prepolymer was observed. The load was then removed and the specimen left to heal for 3 days before being loaded again and tested to failure in the third loading test.

5.2.2.3. Results and discussions

Figure 5.7a shows the typical load-displacement behaviour observed for both the self-healing and the control beams. The presence of the self-healing system decreased the overall elastic modulus of the beam as the adhesive-filled glass tubes were less stiff than the concrete that was replaced. The crack strength of self-healing beam during the first loading, represented by the first peak at a load of 2.23 kN, was similar to the crack strength of the control beam. A second peak in load-displacement curve was observed which was caused by the fracture of glass tubes, typically occurring within 10 seconds after the crack in mortar beam was initiated. Once the tubes were broken, gravity and capillary force acted as driving force for the adhesive to flow towards the gap formed by the crack.

The second loading was performed after 4 days of healing and the load-displacement curve shows an initial peak of 1.44kN, which corresponds to the initiation of a second crack, but the specimen can be further loaded up to a higher load of 2.31kN. The newly formed crack initiated from a point at the bottom surface of the beam that is very close to the first crack and they bridged together when the second crack propagated further into the specimen. This suggests that the first crack has partially healed. The adhesive in the vicinity of the crack mouth cured fully having been in contact with air for 4 days. However in regions close to the crack tip which is depleted of air for curing, curing may not have completed with some adhesive still in its liquid state. This weak zone attracted nearby propagating cracks. Secondly, the smaller damage initiation load of 1.44kN may be due to the softening the beam caused by the formation of micro-cracks in the vicinity of the first crack zone during the first loading. Although the specimens were partially healed after 3 days, the recovered strength equaled the strength of the control specimen. The third loading

was performed after the specimen was left to heal for 3 days for both specimens. Similar to the previous loading, a new crack was formed, but this time, it did not merge with the previous cracks, suggesting that the damage has been fully healed. The order of crack formation is shown in Figure 5.7b.

(a)

(b)

(c)
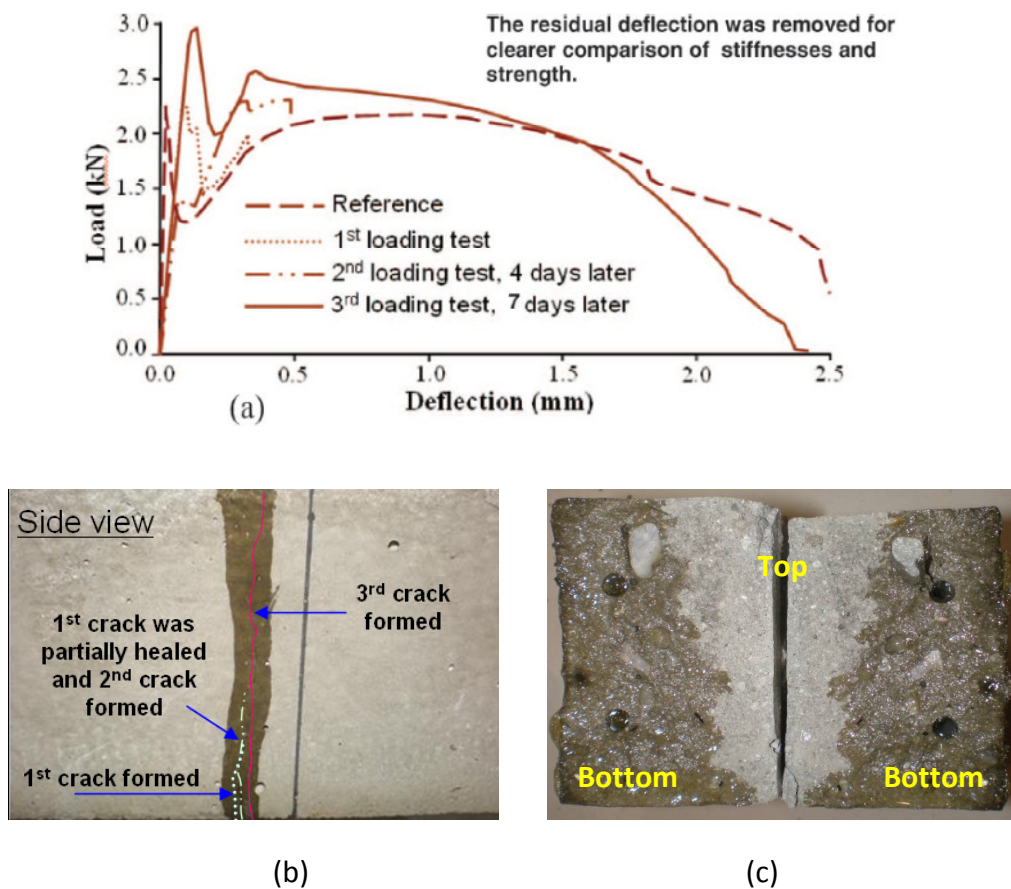
Figure 5.7: Experimental results of self-healed specimen: (a) load-deflection curve; (b) order of crack formation; and (c) dissected specimen after healing thrice.

As cracking only started from the weakest point in a specimen, complete healing strengthened this zone and it is not surprising that a new crack was initiated at a location corresponding to the next weakest zone in the specimen. This is confirmed by the result of the experiment showing the crack strength of the specimen has

increased to 2.95kN, which is 32% higher than that of the control specimen. Table 5.1 summarizes the experimental results.

Indeed, the waiting time of 7 days for epoxy hardening is relatively long and limits the applications of the current self-healing system. However, the scope of the current study focuses on mechanical aspect of implementing self-healing idea in civil engineering applications, rather than chemical aspect. Finding a faster response healing agent is strongly recommended for future work.

Table 5.1: Summary of proof-of-concept experimental results

Specimen	Crack Initiation Load (kN)	Ultimate Load (kN)
Control	2.25kN	2.25kN
Undamaged self-healing specimen	2.23kN	2.23kN
Self-healing specimen after first healing	1.44kN	2.31kN
Self-healing specimen after second healing	2.31kN	2.95kN

5.2.3. Implementation issues of self-healing system in structural members

5.2.3.1. Protection of self-healing system

In the foregoing experiments, the protection of self-healing system was not necessary as mortar specimens were used. However when casting actual structural concrete members, the self healing system may be damaged due to impact by aggregates or severe vibration. A protective layer for each glass tube has to be installed to prevent breakage during the casting process. Finding an effective protection method for the self-healing unit is the basic requirement to implement self-healing in concrete structural elements.

In the first trial, self-healing unit is protected by a 6.5mm thick mortar strip where demoulding was done after 1 day before the host beam was cast as illustrated in Figure 5.8a. The cement-based protective layer such as mortar is preferred as it might provide good bonding with the surrounding concrete mixture. The 6.5mm thickness of the mortar protection trip is used since it is the smallest thickness can be cast using a mould.
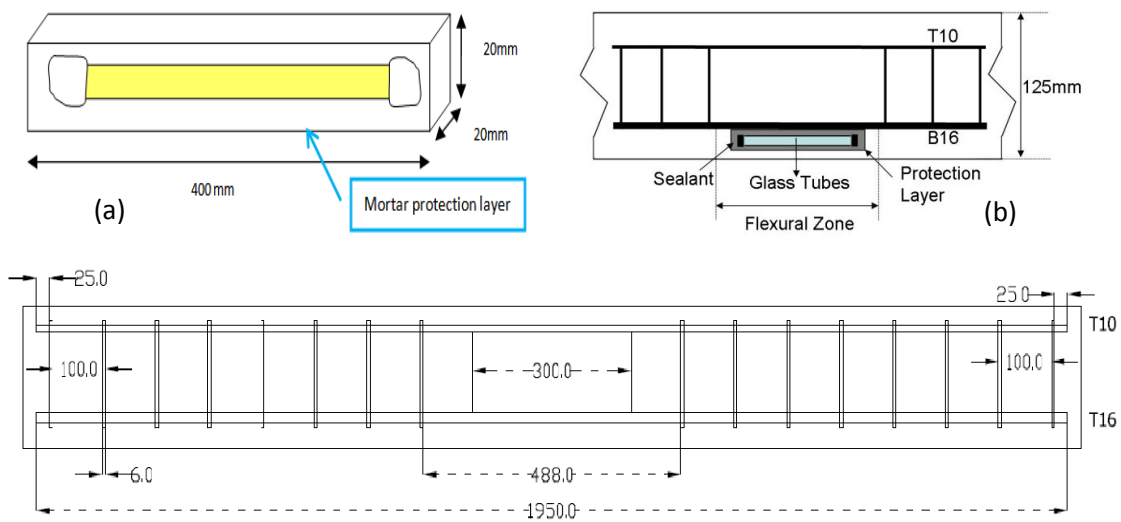
Figure 5.8: Testing for protected self-healing units: (a) self-healing unit protected by mortar trip; (b): diagram of the embedded self-healing system; (c) reinforcement detail.

To investigate if the protected self-healing system can work well in structural concrete beam, a concrete beam of size 2000mm x 125mm x 200 was embedded with 2 glass tubes of length = 310mm, inner diameter = 5mm, outer diameter = 7mm. The tubes were filled with Isocyanate Prepolymer using aquastick to seal both ends and protected as described earlier. They were tied beneath the bottom steel reinforcement before the host beam was cast. The beam was demoulded after 48 hours to air dry for 24 days. Figures 5.8b and 5.8c show the diagram of the self healing system implemented and the detailing of the reinforcements in the concrete beam. In fact, this

154

experiment can be considered as a pre-test for the real experiment with structural self-healing beam. The hollow glass tubes in this experiment are larger than those used in proof-of-concept test for the ability of storing and delivering sufficient amount of adhesive into meso-cracks. However, the thickness of the tubes still remains to be 2mm to preserve the brittleness.

The beam was subjected to displacement control four-point bending until failure. Although the leakage of Isocyanate Prepolymer could be seen at the crack on the bottom and the side surfaces on the beam, there was a delay at more than 5 minutes after the first crack occurred. Further investigation was made by dissecting the beam at the cracked area, as shown in Figure 5.9.

Figure 5.9: Self-healing unit protected with 6.5 strip mortar and the surrounding concrete

The image of the intact protected self-healing unit and the fact that there was no signal of a pre-dried Isocyanate Prepolymer at positions other than crack location strongly imply the capability of the mortar trip to protect the self-healing system. However, the delay in the leakage of Isocyanate Prepolymer recommended that the protective mortar layer is too thick to provide timely rupture of the tubes. In addition, bonding between the protective layer and the surrounding concrete mixture is very

poor, as can be seen in Figure 5.9, and may create slippage of the protected self-healing units.

After the first trial, three other protection methods were proposed, as imaged in Figure 5.10a-c, in an attempt to overcome the drawbacks of mortar trip protection layer:

i. Mesh: The glass tube is wrapped by fine steel mesh. This method protects the glass tubes from the impact of concrete during casting and does not provide extra strength to the glass tubes.

ii. Spiral Wire: The glass tube is wrapped by spiral wire. This method protects the glass tubes from the impact of concrete during casting, provides no extra strength to glass tubes and creates the roughness for better bonding between the self-healing system and the surrounding matrix.

iii. Mortar Layer: The glass tube is wrapped by spiral wire, followed by a thin layer of mortar that is applied an hour before the casting of the specimen. The thickness of the mortar layer is around 3.5 mm, as compared to 6.5mm in mortar strip method. The spiral wire helps to increase the bond between the mortar and the glass tube, and increase the roughness on the outer surface of the mortar layer for better interlock with the surrounding matrix.

To investigate the performance of these methods, three pairs of glass tubes were each filled with different color dyes, with each color representing one protection method. All six protected glass tubes were embedded into a mould for casting a 125x200x2000mm concrete beam. After curing, the concrete beam was loaded under a four-point bending test, in which all six embedded glass tubes were positioned in the

flexural zone. Any release of dyes during testing, as shown in Figure 5.10d, would indicate that the glass tubes remain intact during casting and the healing units with the protection layer can break successfully when the crack passes through it.
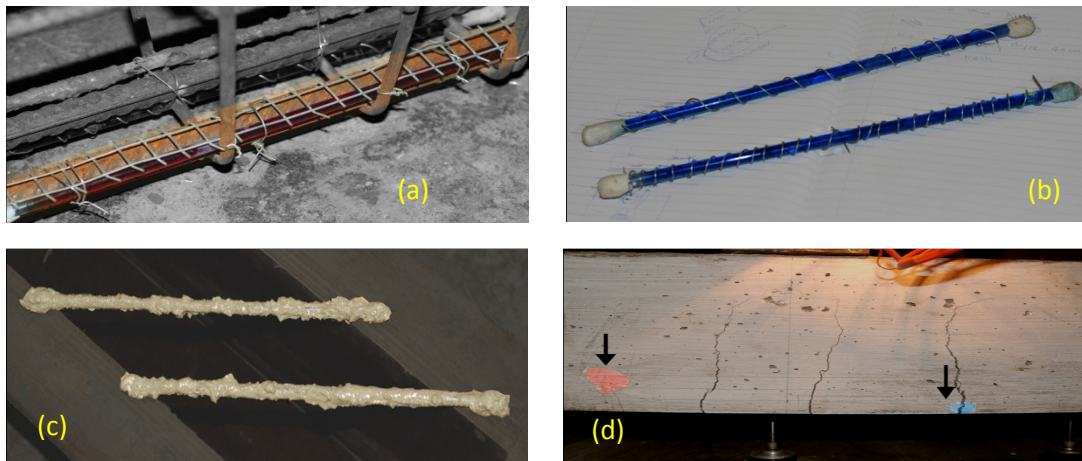
Figure 5.10: Protections for self-healing unit: (a) Mesh; (b) Spiral Wire; (c) Spiral Wire coated with mortar; (e) test results

Although results showed that both the Spiral Wire and Spiral Wire coated with mortar methods were qualified for protection through the observation of released dyes, it was found, after the test by dissecting the beam, that a small region of the concrete around the healing unit protected by Spiral Wire was pre-stained with the dye. This suggests that the Spiral Wire method did not protect the glass tube well during casting procedure and hence, the Spiral Wire coated with mortar approach is chosen to adopt for subsequent structural self-healing specimens.

5.2.3.2. Detection of breakage of glass tube

As part of the verification process, it would be informative to detect the instant that the glass tube breaks. Detection is difficult for embedded systems especially in deep beams, foundations or at the interfacial zone of the steel-concrete composite structure. Strain gauge can be used to detect the rupture of the tube but it relies on advance knowledge of rupture zone, otherwise, multiple gauges along the tube need to be installed. An efficient way is to use an optical fiber as shown in Figure 5.11.

(a)   (b)

(c)   (d)
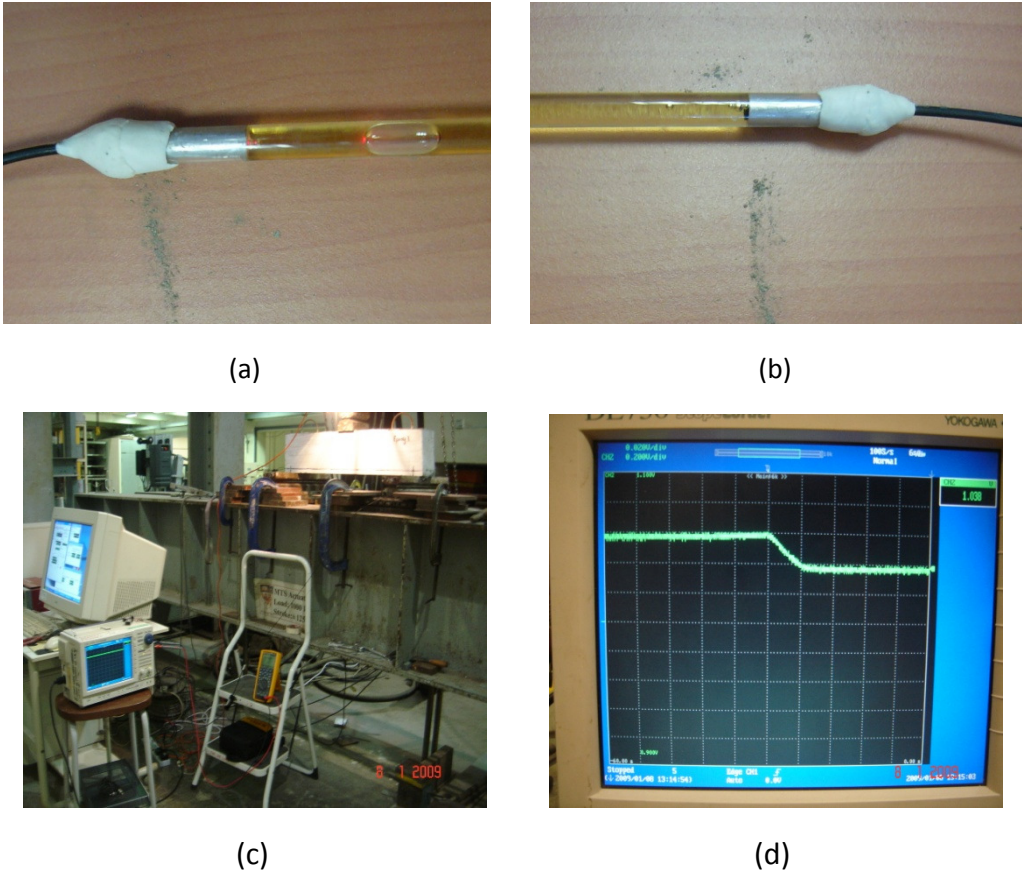
Figure 5.11: Detection of glass tube rupture using optical fiber: (a) head with input laser; (b) head that receive signal; (c) experimental set up with optical fibers; (d) dip in signal of laser when tube was ruptured.

At each end of the tube, a rivet (see Figures 5.11a-b) is used as a guide to align the ends of the optical fiber so that when a laser light is projected from one end, the other end can receive it. When the beam is loaded in flexure such that the glass tube is broken, the intensity of the laser light at the receiving end will dip, as shown in Figure 5.11d, due to the misalignment of the two ends.

5.3.   IMPLEMENTATION   OF   SELF-HEALING   FUNCTION   IN REINFORCED CONCRETE BEAM

5.3.1. Specimens fabrication and testing procedure

Self-healing reinforced concrete beams are experimented under three-point and four-point bending test to investigate the effectiveness of sensing and healing when vertical cracks are formed by different mechanism. In the former one, self-healing units were embedded in the zone where combined effect of bending and shear is active; while in the later one, self-healing units were embedded in pure flexural zone.

5.3.1.1. Beams under three-point bending experiments

Two concrete beams at size 900mm x 125mm x 200mm were cast. Among them, one is self-healing beam while the other one is the control beam. Both of them are identical except that in self-healing beam, two 300mm long protected self-healing units were tied beneath the longitudinal reinforcement. Material properties of the beams are presented in Tables 5.2, while the configuration of self-healing beam is depicted in Figure 5.12. It is notable that optimization study of self-healing units in

terms of locations and volume, which is out of the scope of the current research, is recommended for the future study.

Table 5.2: Properties of materials used for reinforced concrete beam

| Material Properties | Materials Used | | |
	Links	Concrete	Steel
Strength	500N/mm^2	35N/mm^2	460N/mm^2
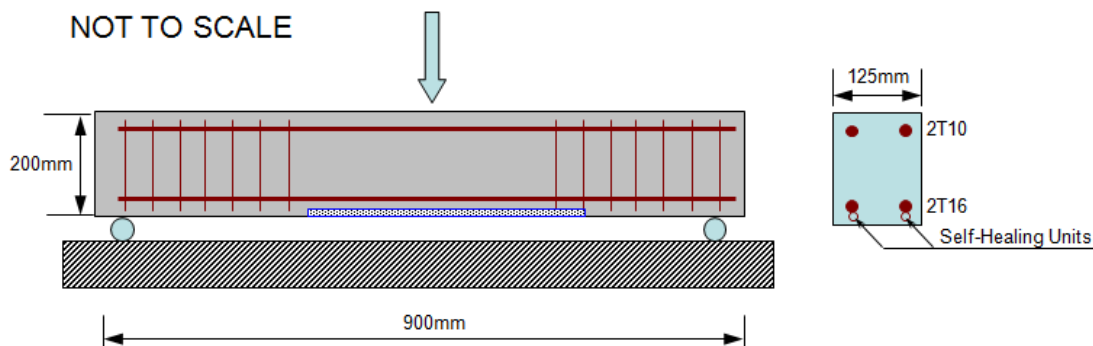
Figure 5.12: Self-healing beam under three-point bending test

Both beams were subjected to three-point bending test where displacement control actuator was used with loading rate 0.2mm/min. One transducer was installed at the mid-point of each beam to record the deflection data. The control beam was loaded until failure to provide reference on maximum load capacity and stiffness. Meanwhile, the self-healing beam was loaded until the leakage of healing agent was observed. Then, the beam was unloaded and unmounted to rest for 7 days before being reloaded again to examine the self-healing capacity.

5.3.1.2. Beams under four-point bending experiments

Two specimens, namely control beam and self-healing beam, were fabricated at the size of 125mm x 200mm x 2000mm using the same materials as in the three-point bending test series. No self-healing units were installed in the control beam whereas six self-healing units, each of length 400mm, were embedded in the flexural zone of the four-point bend beam and all tubes were positioned right below the tensile reinforcement bars as shown in Figure 5.13. Displacement control actuator was used with a loading rate of 0.2mm/min.

While the control beam was loaded to failure, the self-healing beam was loaded in loading – unloading sequence in which the resting period of 7 days was applied for curing process. During all experiments, displacement at the center of the beams were recorded continuously using transducers and plotted together with applied loading value to form load-displacement curves.
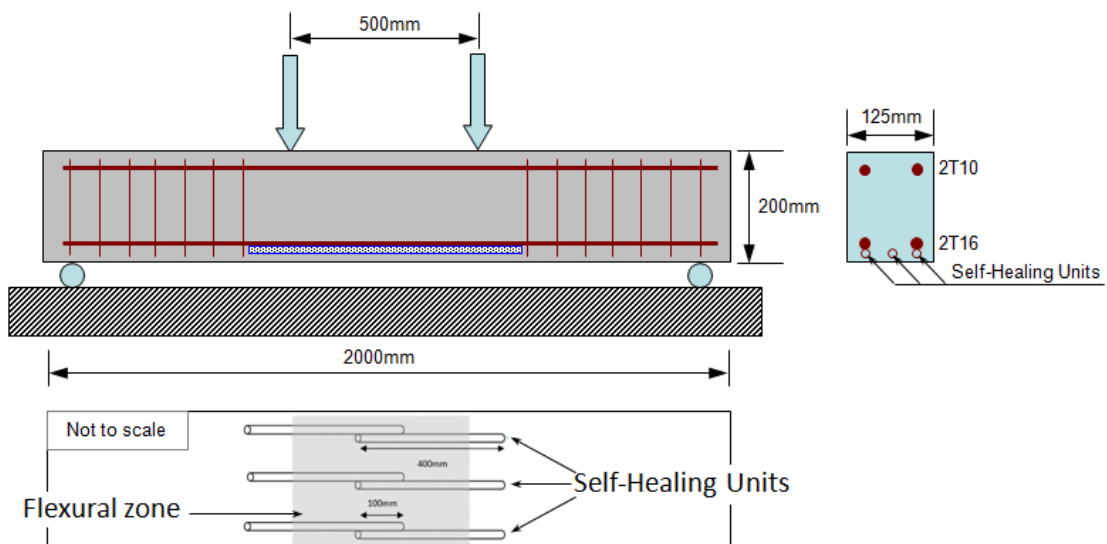
Figure 5.13: Self-healing reinforced concrete beam under four-point bending test

5.3.2. Results and discussion

5.3.2.1. Beams under three-point bending experiments

Load-displacement curves of self-healing beam and control beam were plotted in Figure 5.14 for comparison, in which there is a slight increase in maximum load capacity of self-healing beam (165.97kN) compared to that of control beam (157.65kN). Although the difference in maximum load capacity of self-healing and control beams are insignificant, there is strong evidence of healing effect in terms of stiffness of the beams.

(a)

(b)
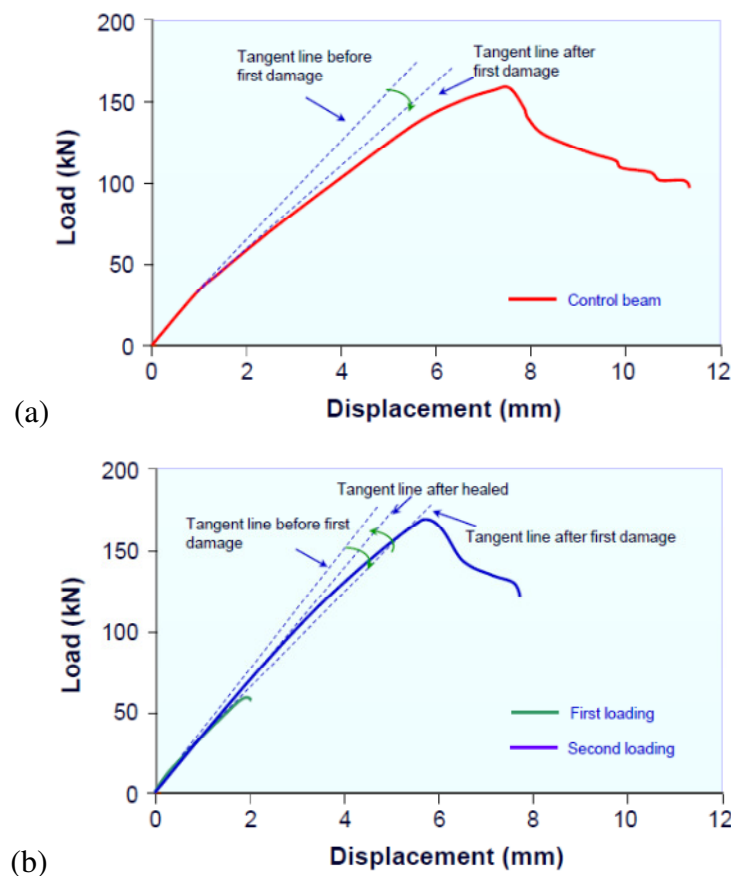
Figure 5.14: Load displacement curve of beams under three-point bending test: (a) control beam; and (b) self-healing beam.

As can be seen in the Figure 5.14, the tangent stiffness of both control and self-healing beams keep reducing from the loads 34.11kN and 35.09kN, respectively, signifying the crack localization and development to become the first severe damage in the beams, which coincides with the experimental observations. To be comparable, tangent stiffness of the self-healing beam is also calculated at the load value of 35.09kN when first damage was created. As shown in Figure 5.14b, there was a recovery in terms of stiffness in the healing beam.

Quantifying, tangent stiffnesses of both control and self-healing beams obtained from experiments are normalized with their pre-damage stiffnesses and presented in Figure 5.15, in which, 52% of loss stiffness or 86% of pre-damage stiffness was recovered in self-healing beam after being healed.
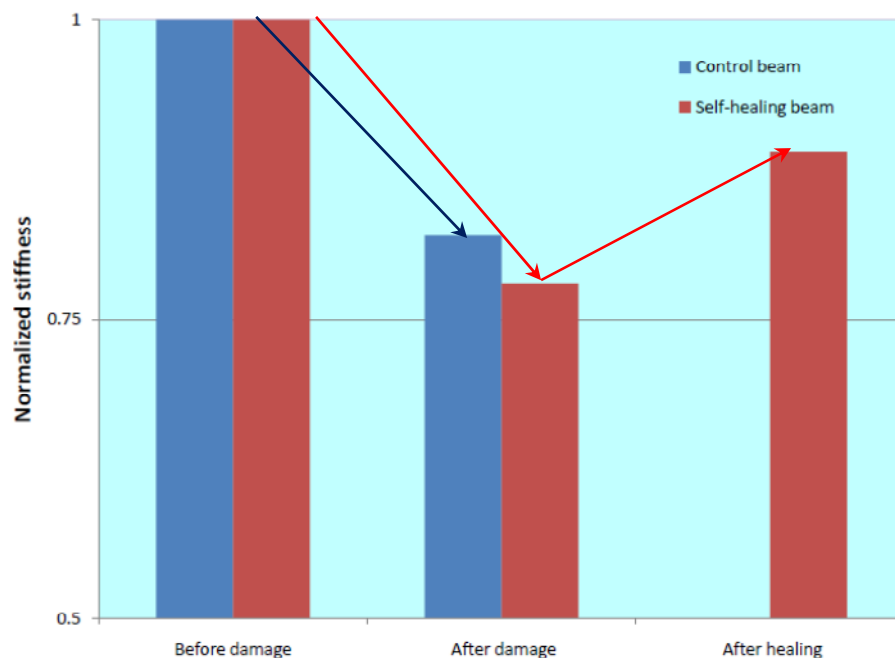
Figure 5.15: Normalized stiffness of control beam and self-healing beam.

5.3.2.2. Beams under four-point bending experiments

The first crack happened in the self-healing beam at around 18kN and the leakage of Isocyanate Prepolymer was observed shortly after when the load reached 24kN. The crack width at the level where self-healing units installed were 0.3mm. The timely flow out and the well distribution of healing agent into the opening cracks, which failed to happen in the preliminary tests with mortar strip protective layer, is another demonstration of the effectiveness of the using protection method. Loading was continued further to allow more healing agent flow out and then stopped at 37kN. After this, the beam was unloaded and was rested for 7 days to allow healing before it was re-loaded until fresh leakage of healing agent was detected. This unloading-reloading cycle was repeated twice and each time, new cracks were formed while the old cracks did not re-open, clearly signifying that the healing is effective and the beam has multiple self-healing abilities.

The effectiveness of the healing was also quantified in terms of the tangent stiffness recovery as depicted in Figure 5.16, in which stiffnesses after damage, after first healing and after second healing are normalized to the before damage one. Analogous to the beams under three-point bend, both self-healing and control beams experienced the continuously decrease of tangent stiffness after damage but the former one is able to recover its stiffness after healing. In detail, after the first damage, the stiffness of the control and self-healing beams were reduced to 76% and 74%, respectively, of before damage stiffness. After the first healing, the self-healing beam regained its stiffness back to 88% of the pre-damage stiffness. Nevertheless, stiffness of the self-healing beam after the second healing fell back to 85% of the pre-damage stiffness. This may due to the insufficient healing agent used for the second healing.

164

(a)   (b)
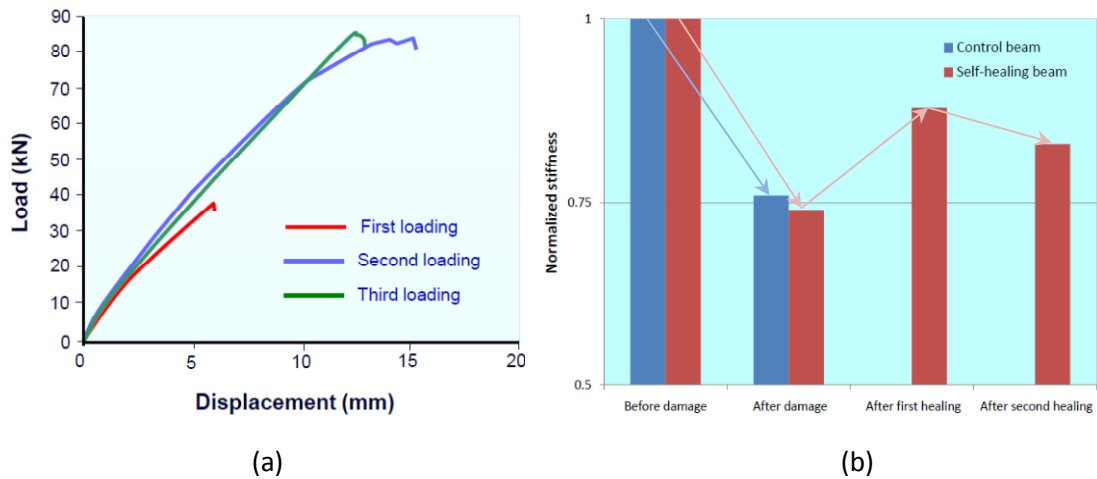
Figure 5.16: Result of self-healing beam under four-point bending test: (a) load-displacement curve; (b) normalized stiffness.

Experiments with self-healing beams under 3-point bending load, where there is shear effect at the healing zone, and 4-point bending load, where the healing zone is subjected to pure bending moment, show an insignificant influence of shear loading on healing effect. This may be because of the high shear strength of the healing agent. In addition, self-healing beams in the current study are reinforced concrete beams, in which the steel reinforcements will distribute the cracks along the damage zone regardless the loads are 3-point or 4-point loading. Thus, the results with self-healing beams under 3-point bending and 4-point bending loads in the current study are very similar.

5.4.   IMPLEMENTATION OF SELF-HEALING FUNCTION IN REINFORCED CONCRETE COLUMN

In this experimental series, self-healing units are embedded in column elements to investigate the effect of healing system for horizontal and inclined cracks

when the presence of gravity does not offer much help to the flow of the healing agent.

5.4.1. Specimens fabrication and testing procedure

One control column and one self-healing column were cast using the same concrete Grade35. Twenty 350mm-long self-healing units were tied to the longitudinal reinforcement bars of the self-healing column while no healing tubes were introduced in the control one. Self-healing units were designed to be short to avoid the buckling failure and to act as compartments to prevent all healing agent flows into one single crack and hence, allow multiple healings.

Figure 5.17 illustrates that configuration of the experiment on self-healing column in which, displacement controlled horizontal load was applied close to the top of the columns at the rate of 0.1mm/min. The self-healing column was loaded until the leakage of healing agent was observed and then, it was unloaded and rest for 7days for curing before being reloaded. The loading-unloading cycle was applied thrice to examine the multiple healings ability. The control column was loaded until damage propagated to half of the section then was unloaded before loading again. After being applied loading-unloading two times, the control column damaged severely and the experiment was stopped for safe.
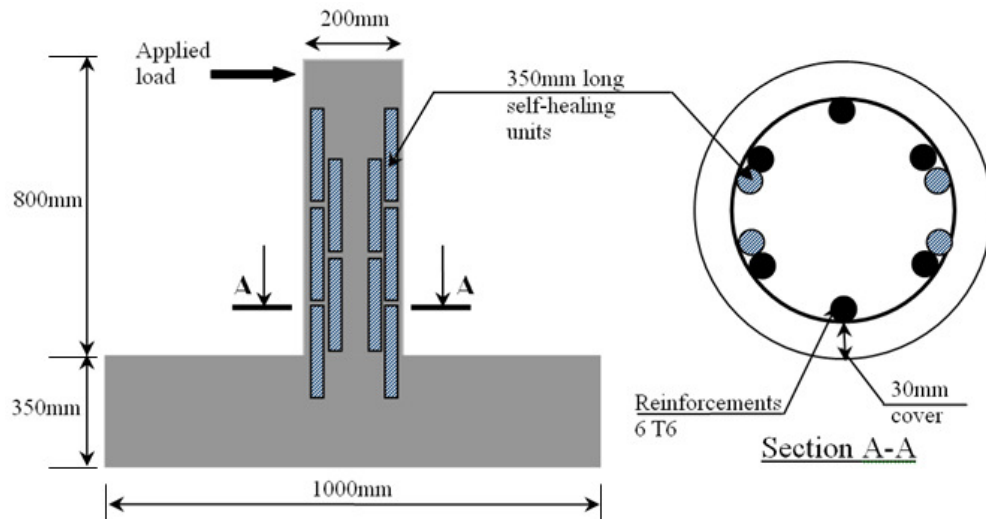
Figure 5.17: Elevation and cross sectional views of self-healing column.

5.4.2. Results and discussions

Load-displacement relationship of self-healing column and control column are plotted in Figure 5.18a and b. As can be seen, after each loading-unloading sequence, the stiffness of the control column reduced implying the damage condition became more and more significant. In contrast, the stiffness of self-healing column exhibited recuperation after each healing time. The trends in changing stiffness of both columns are quantified using normalized tangent stiffness and graphically plotted in Figure 5.18c, in which after the first damage, control column and self-healing column lost 42% and 51% of their original stiffness. After recuperation, the self-healing column is able to recover to 70% of their original stiffness.

(a)

(b)

(c)
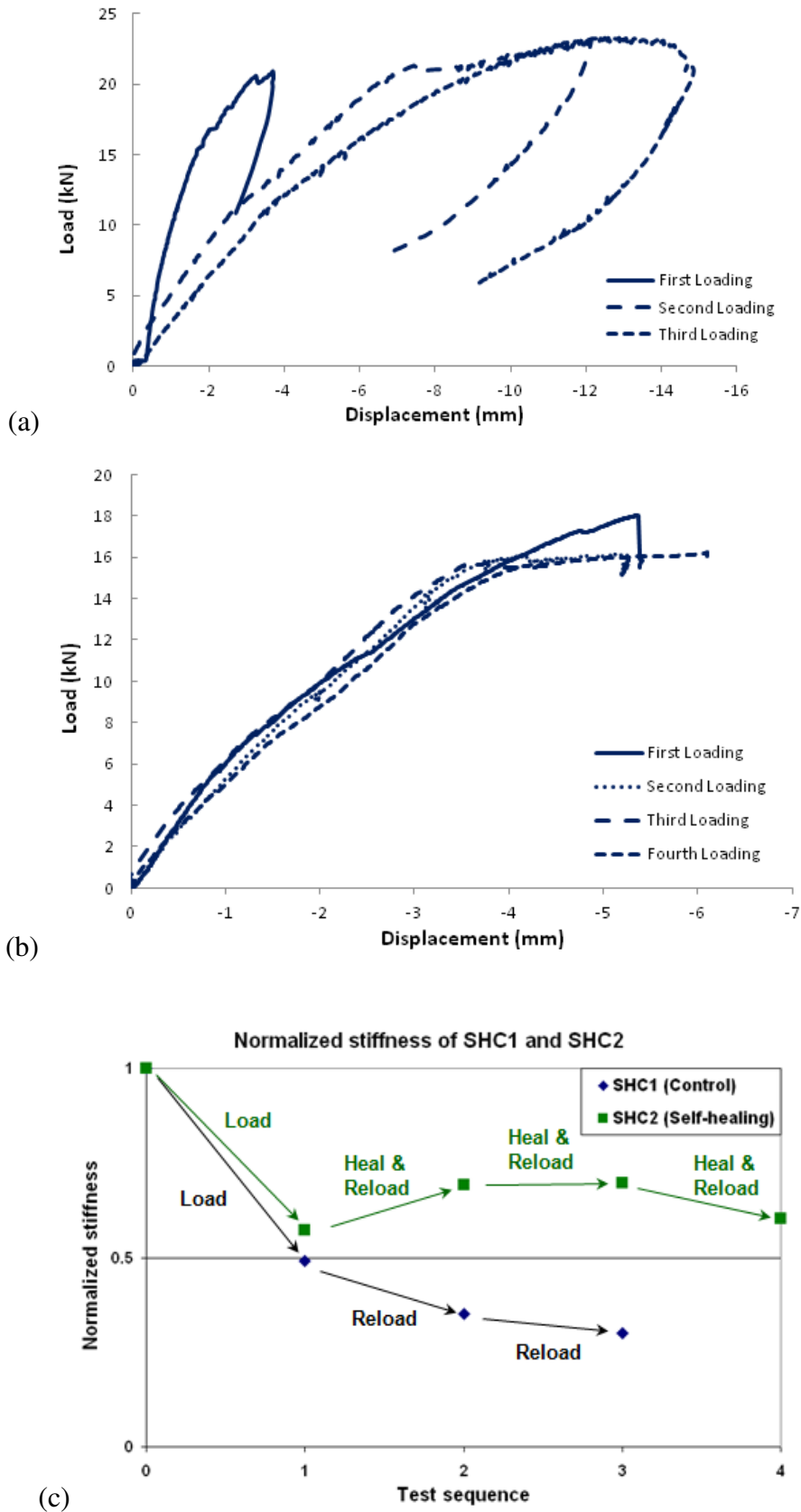
Figure 5.18: Results for cantilevered columns test: (a) load-displacement curve of control column; (b) load-displacement curve of self-healing column; (c) trend of changing normalized stiffness of columns
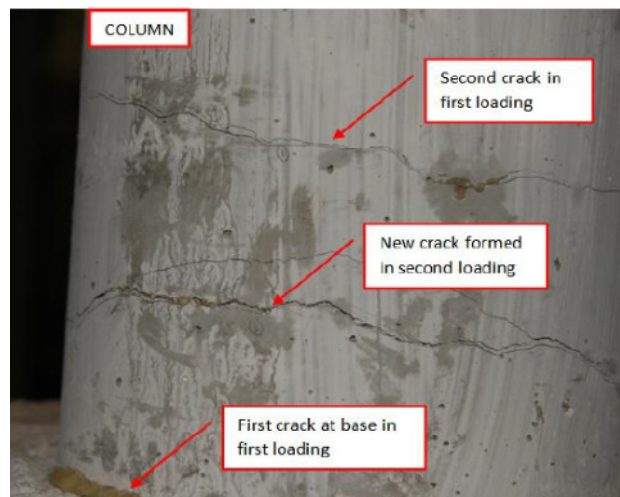
(d)

Figure 5.18: Results for cantilevered columns test: (d) observation from self-healing column.

Analogous to the observations in self-healing beam test, for each time of loading, there were new crack formed without any re-opening detected from the healed cracks. For instance, during the first loading, there were two cracks appeared at the bottom zone of the column where maximum moment was applied. Healing agent was observed to be leaked short after the crack propagated through the level where healing units were installed. After 7 days of curing, these two cracks were fully healed and not opened during the second loading; instead, a new crack was formed between them as illustrated in Figure 5.18d. The presence of newly formed cracks and the absence of old cracks re-opening after each loading signify that the self-healing column was able to perform the autonomic healing multiple times, which is also reflected from the multiple recovery of stiffness.

5.5.   IMPLEMENTATION   OF   SELF-HEALING   FUNCTION   IN REINFORCED CONCRETE SLAB

In this experimental series, the function of self-healing in slab element was evaluated for the case when cracks open and close fast due to the subjection of impact loading.

5.5.1. Specimens fabrication and testing procedure

Two specimens, namely the control slab and the self-healing slab, were used to compare and quantify the amount of stiffness recovery. The 1m square specimens with a thickness of 0.1m are cast in Grade 40 concrete with reinforcing steel meshes of opening spacing at 100mm and diameter of 4mm. In the self-healing slab, four 400mm long healing units were attached to both the top and bottom steel mesh in each of the two orthogonal axes as shown in Figure 5.19a.

The setup of the drop weight test, which used to create impact load onto two specimens, was shown in Figure 5.19b where (1) is a 20-kg impact hammer; (2) is a vertical aluminium guide to ensure the location of impact is at the center of the slab; (5) is a steel frame to provide the base for the test. The boundary conditions of the slabs were pinned at 2 opposite edges where G-clamps (4) were used to prevent the side displacement of the slabs. On each of the remaining 2 edges, one belt was used to fasten the slabs to the steel frame to prevent the bouncing of the slabs after being impact. The impact energy was standardized by dropping from a constant 2-meter height.

170

(a)   (b)

(c)   (d)
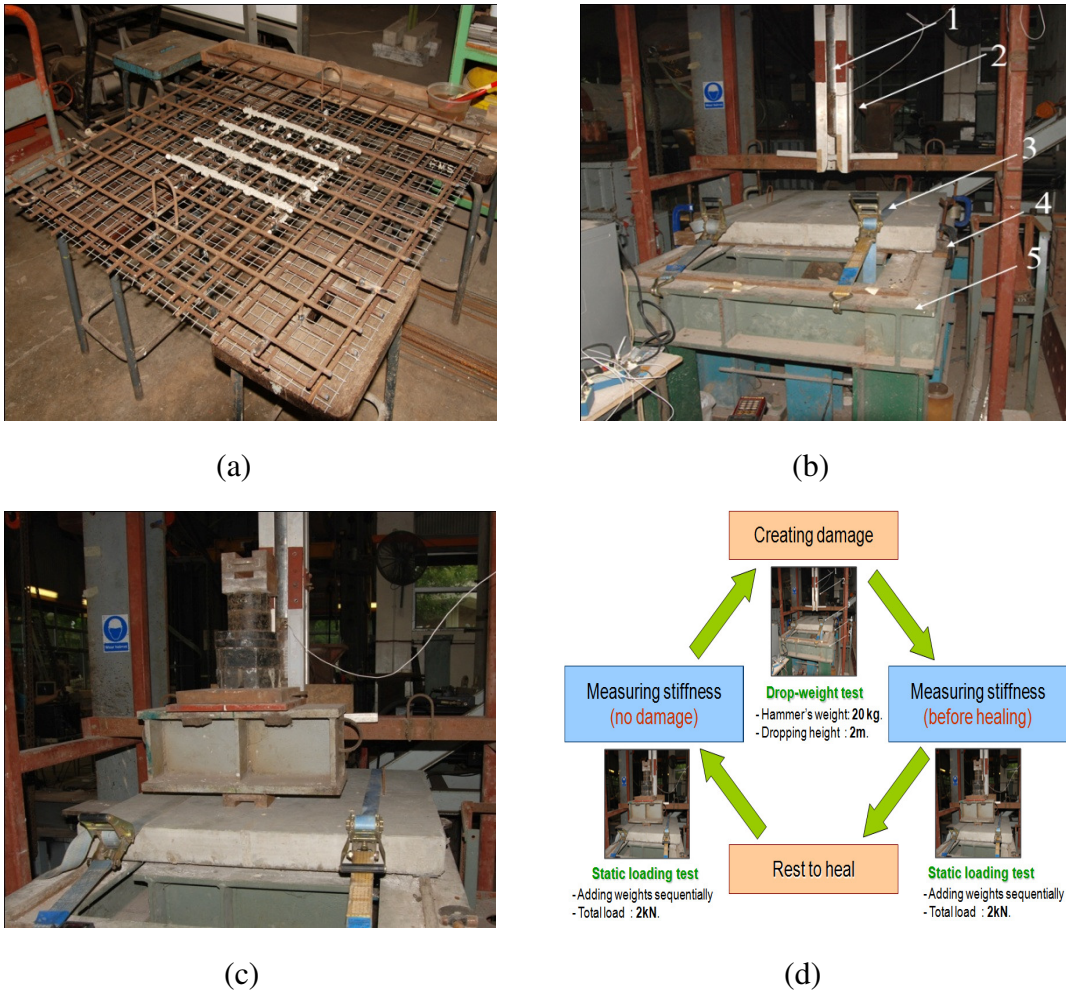
Figure 5.19: Experiments on self-healing slab: (a) reinforcement cage with self-healing units; (b) Drop-weight test to create damage; (c) Static loading test to measure stiffness; (d) Diagram of one typical sequence in the experiment.

To quantify the effect of self-healing, the static stiffness before and after impact were selected for comparison. The static stiffness is chosen as this quantified parameter reflects the "health" condition of the structure where damage in the structure is reflected in the loss of stiffness. The setup of the static loading test is shown in Figure 4c where a transducer with a resolution of 1μm was located beneath the center of the slab. Steel weights, sitting on a thick steel U-channel to localize the load, were sequentially applied on top of the slab until the limit of 2kN was achieved. The value of 2kN was chosen based on a preliminary test on the trial slab to ensure no

non-linear performance happened even in the case that the slab was heavily damaged. All steel weights range from 6.3kg to 29kg except a 98-kg I-beam used as the largest weight and served as a platform for adding the other weights.

Figure 5.19d illustrates a typical loading sequence in the experiment in which the self-healing slab was subjected to repeatedly impacts until the release of healing agent was spotted and then it was subjected to static loading test to measure the before healing stiffness. After that, the slab was left for 7 days for curing before being subjected to static loading test again to measure the stiffness after healing.

5.5.2. Results and discussions

The results of the test were tabulated in Table 5.3 and graphically presented in Figure 5.20 where the control slab suffered from a continuous loss in stiffness after each impact and failed after test sequence 3. In contrast, the self-healing slab exhibited a strong recovery after test sequences 2 and 3, in which up to 99% of the stiffness was recovered. The lowest healing efficiency is in test sequence 1 and this is possibly because the impact energy was not large enough to fully trigger the self-healing systems. Similar to the self-healing beams and column, crack reopening was not observed after healing. After test sequence 4, the center of the healing slab, where the healing units were placed, were strengthened by healing to the extent that meso- and macro-crack no longer form in this region but critical cracks were formed at the corner zones which could not be healed due to the absence of healing units.

Table 5.3: Stiffness of control and self-healing slabs under impact loading

Test Sequence	Control slab			Self-healing slab		
	No. of Impacts	Stiffness (kN/mm)		No. of Impacts	Stiffness (kN/mm)	
		Before impact	After impact		Before impact	After impact
1	1	43.8	34.3	1	42.9	33.2
2	1	34.2	20	2	38.8	24.5
3	1	20	N.A.	4	38.6	24.1
4	-	-	-	5	36.5	N.A.
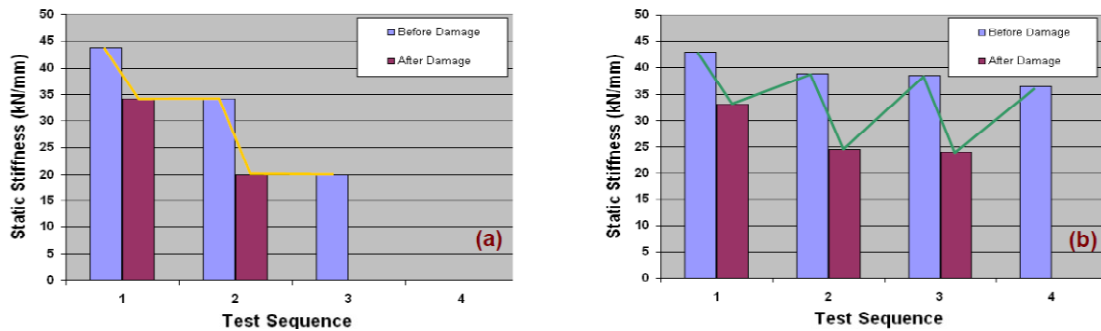
Figure 5.20: Stiffness of control and self-healing slabs under impact loading

5.6.   SUMMARY

This chapter addresses the implementation of self-healing function in reinforced concrete elements. First the combination of hollow glass tubes and air-cure adhesive Isocyanate Prepolymer were considered and verified through proof-of-concept experiments as promising healing units. Next, the protection methods of Isocyanate Prepolymer filled glass tubes to prevent the premature damage of self-healing system caused by aggregate impacts and severe vibration during casting procedure of structural members were examined. Experiments with 4 methods of protection using mortar strip, steel mesh, spiral wires and spiral wires coated with a mortar layer showed that a 3.5mm thick mortar layer wrapping around the glass tube spiralled with steel wires is able to protect the self-healing system during casting

procedure and facilitate timely rupture of the glass tube to release the healing agent. The proposed protected self-healing system was then implemented in three basic structural members namely, beam, column and slab. The self-healing beams were experimented under the three-point and four-point bending test repeatedly and the multiple crack healing was observed through the flowability of the healing agent into cracks to bond the crack surfaces. Although there was no increase in maximum loading capacity of self-healing beams, over 85% of initial flexural stiffness was able to be recovered. Similarly, self-healing was implement successfully in column element, where the major crack direction is horizontal, with up to 70% of stiffness was recovered. The self-healing slab was damaged using impact drop weight. Again, multiple crack healing ability was performed with the maximum healing efficiency was found to be 99% in terms of stiffness recovery.

In the current study, there is a need of load removal to allow the self-healing elements fully healed before they are reloaded. This trend is very common in literature studies on self-healing materials and it is applicable to deal with sudden accidental loads such as impact, blast and seismic loading. It would be much comprehensive if the study is extended, in the future, for cases of sustain load.

174

CHAPTER 6

CONCLUSIONS AND RECOMMENDATIONS FOR FUTURE WORK

6.1.   CONCLUSIONS

A numerical model to predict the macro behaviour of self-healing composites has been developed by adopting multi-scale modelling using Representative Volume Element concept. Good agreement between the predictions from numerical models and experimental data, in terms of Young's modulus, strength and healing efficiency, verifies the correctness of the proposed model.

Firstly, RVE approach is examined in detail based on simulations with porous epoxy. Results from the simulations reveal that the SP-RVE approach is more efficient for composites with low volume fraction of inclusions, since it can provide reasonably accurate prediction at a low computational cost. For instance, the SP-RVE can be used to predict elastic behaviour of porous materials less than 10% of error when the volume fraction of voids is less than 15%, which totally agrees with the critical volume fraction for SP-RVE approach using Drugan and Willis' criterion. While SP-RVE approach is more suitable for composites with low volume fraction of inclusions, MP-RVE approach is very effective for composites containing high volume fraction of reinforcements as it fully models particle-matrix and inter-particle interactions.

A comprehensive explanation on the contradict conclusions on the existence of RVEs for damage behaviour was offered in the current research through investigations on RVEs at different size. It was shown that there is size effect in homogenized stress-strain curve found from RVEs caused by the strong localization of damage with the formation of a single crack across the critical cross section. As such, the RVE concept is not suitable for predicting the inelastic stress-strain softening response of quasi-brittle composites. Instead, fracture energy or fracture toughness calculated through the stress versus crack opening displacement relationship were illustrated as size invariant properties and they could be used for to simulate the damage behaviour of heterogeneous materials. As an example for the case of porous epoxy, fracture toughness predicted from MP-RVE models compares well with the experimental data for up to 20% volume fraction of voids.

The RVE approach has been adopted to develop a numerical model to predict material behaviours and healing efficiency of micro-capsule based self-healing materials. In the proposed model, the matrix is modelled as a homogeneous material and its crack-softening behaviour is simulated using smeared crack model. A preliminary study found that the encapsulated healing agent can be modelled as Neo-Hookean material with shear modulus of 300kPa . This result suggests that the micro-capsules are too soft, at more than three orders of magnitude softer than the matrix, to have any significant contribution to the elastic response of self-healing composites and hence, can be modelled as void in the RVEs. The shear-yielding effect of the micro-capsules on the post-elastic behaviour of the composite is modelled by introducing shear retention in the smeared crack model. As the matrix toughening is attributed to the micro-capsules, the shear retention factor also varies with the volume fraction of the micro-capsules. Good results at less than 10% of error, compared to

experimental data, have been achieved for the predictions of Young's modulus, strength, and healing efficiency have been achieved with MP-RVE approach verified the proposed model.

The simulated material properties of micro-capsule based self-healing materials were then fed, as inputs, in a numerical simulation of simply supported beam three-point bend to study the effect of self-healing on structural behaviour. The simulation result reveals that healing with low strength healing agent, compared to the virgin material, will cause crack reopening and hence, limit the healing effect in terms of recovered load bearing capacity. In contrast, healing with high strength healing agent may induce the load bearing of the structure. Numerical study with tubular self-healing system was also carried out to make comparison with capsulated self-healing system. The results showed that self-healing beam using capsulated system may recover load bearing capacity and stiffness better. On the other hand, self-healing beam using tubular system sacrifices some degree of healing to concentrate the healing only severe cracks. These findings provide essential ideas for future researches on designing a self-healing system, which would be an interesting and important topic.

Lastly, self-healing function is implemented in reinforced concrete to develop a new sustainable and protective structure. For this class of applications, tubular system is more preferable than micro-encapsulating system because the former one is concentrated and sizeable, which provide the easiness and plausibility of positioning self-healing units and protecting them from possible pre-mature damage caused by heat generation and aggregate impact during casting process. In addition, the hollow tubes used as containers in tubular system are commercialized, and therefore, they are more economics than the micro-capsules, which can only be produced in laboratories.

Preliminary studies on the selection of self-healing unit's components were carried on with the consideration of requirements for healing agent and containers. It was found that the one-part air curing adhesive Isocyanate Prepolymer and the hollow glass tubes are a promising combination to be self-healing units. To protect the proposed self-healing unit from impact of aggregate and severe vibration during concrete casting process, four different methods, namely mortar strip, steel mesh, spiral wires and spiral wires coated with a 3.5mm thick mortar layer were experimented. Amongst the four, the method of protection using spiral wires coated with a thin mortar layer is the most effective one and is adopted in the current study.

The proposed protected self-healing units were implemented in three basic reinforced concrete structural members including beam, column and slab to test the healing efficiency. The experiments were conducted with specimens at structural scale, which have not been carried out until the current research. The self-healing beams were subjected to both three-point and four-point bending repeatedly. Multiple crack healings were observed through the leakage of healing agent into cracks and bond the crack surfaces; along with the presence of new cracks formed and the absence of old cracks reopening. The healing efficiency was quantified in terms of tangent stiffness recovered after healing and good results of over 85% of original flexural stiffness was able to be recuperated after healing. Similarly, self-healing was also successfully implemented in column element, where the cracks are horizontally or inclined causing the limited help of gravity force to drive the healing agent into the cracks. Once again, multiple healings with up to 70% original stiffness was recovered. Self-healing was also implemented in slab element and tested for the case when crack opening and closure appears quickly during impact loading. Analogous to two previous self-healing elements, experimental results showed that self-healing slab is

able to perform multiple healings with the maximum healing efficiency of 99% in terms of stiffness recovery.

6.2.   RECOMMENDATIONS FOR FUTURE WORKS

Based on the experimental result and simulation results obtained, discussion presented and conclusion drawn from the current study, some potential areas for further investigation are highlighted as following.

6.2.1.   Extension of RVE approach to predict shear-related material properties

Up to now, numerical models of material properties of composites using RVE concept are more focused on cases subjected to unidirectional tensile or compressive load. Although there have been limited studies on prediction of shear modulus of heterogeneous materials, there is still a need to conduct a comprehensive research on ability of RVE approach to capture the overall response of composites subjected to shear. The need is more significant if RVE concept can be used to capture the fracture energy of composites for mode 2 of fracture, which caused by shear deformation. Had the 2nd mode of fracture behaviour can be predicted using RVE concept, this approach will be able to capture the mechanical responses of composites in the two most common modes of fracture, namely mode I and mode II; and hence, it will be a very powerful tool to analyse and design composites for damage problems.

6.2.2. Optimized design for micro-capsule based SHM

Embedding more microcapsules in the composite will lead to lower the Young's modulus and strength. Moreover, as reported by Brown et al. (Brown et al., 2004), there is a critical volume fraction of microcapsules such that the healing efficiency gained is maximized. Therefore, an optimization search for the volume fraction of micro-capsule is needed to limit the reduction of Young's modulus and achieve a reasonable high level of healing efficiency. Objective functions $g(E_{eff}(f), \eta(f))$ or $g(\sigma_{max,eff}(f), \eta(f))$ needs to be constructed, where f is the volume fraction of microcapsule. The optimal f_0 is determined such that $\frac{\delta g(E_{eff}(f_0), \eta(f_0))}{\delta f}$ or $\frac{\delta g(E\sigma_{max,eff}(f_0), \eta(f_0))}{\delta f}$. Beside the Young's modulus and strength, fracture toughness can also be included in the objective functions to take into account the effect of toughening induced by embedding micro-capsules.

6.2.3. Design for self-healing structure

It is often to observe many cracks in structures made of quasi-brittle materials, such as reinforced concrete elements, under the design service load. When the applied load reaches a critical value or sudden accidental load is imposed, these cracks will localize to fewer major cracks signifying the severe damage that creates dramatic decrease in stiffness or strength of the structure. They are these major cracks are the desirable ones to be repaired, rather than the cracks happen under normal service load. This means, the self-healing system should be designed so that it is only triggered when critical load are imposed. To have such a design for self-healing structure, control parameters such as stiffness or strain/stress at critical location can be used as thresholds. For instance, based on the configuration of a reinforced concrete beam, one can establish an expression of the diminishing stiffness as a function of crack length. Self-healing units will be positioned based on the critical crack length found at the critical stiffness, where any further reduction is undesirable.

6.2.4. Effect of crack healing regime

As illustrated in Figure 6.1, there are healing regimes for a crack namely, full healing, partial healing at the crack tip and partial healing at the crack mouth.
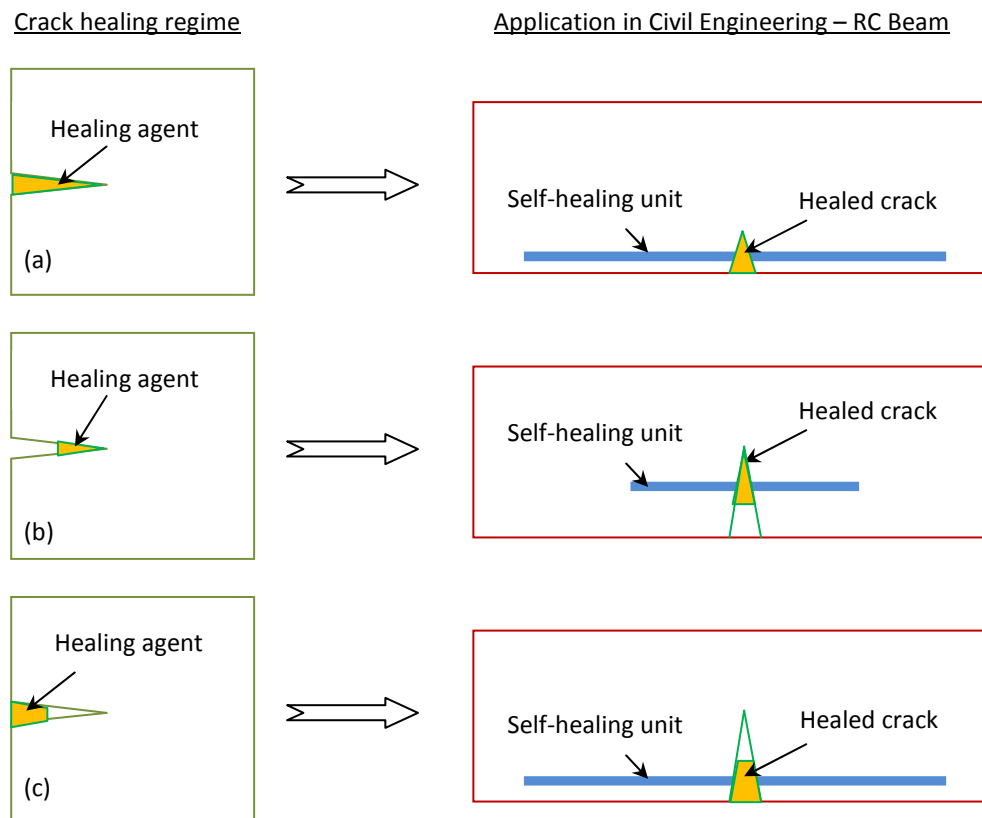
Figure 6.1: Three crack healing regimes and application in an RC Beam: (a) Full crack healing; (b) Partial crack healing at crack tip; and (c) Partial crack healing at crack mouth.

The first regime happens when all healing agent flow into the crack and fully bond crack surfaces together. This regime is the most ideal case that definitely can provides the maximum healing effect. However, this healing regime needs many healing agent or in other word, many healing units, which usually softer and weaker than the host matrix. As a result, side effect for self-healing composites designed with

fully healing ability, such as the decrease in overall Young's modulus and strength, would be more significant. As alternatives, partial healing at the crack tip or at the crack mouth can be considered. While healing at the crack tip can reduce the stress intensity factor by alter the sharpness of the growing crack, healing at the crack mouth can provide constrain for the crack opening. As a result, healing at crack tip or crack mouth may have significant effect on the prevention of crack propagation.

In fact, studies on crack healing regime are more important when incorporated in research on design of self-healing structure because different positioning of healing unit can lead to different crack healing regime. An example can be seen in Figure 6.1 with self-healing reinforced concrete beam. If the self-healing unit locates close to the bottom surface of the beam and the applied load in unsustainable, full crack healing regime can be obtained as observed in experiments with self-healing beams in Chapter 5. However, if the applied load is sustainable or the crack propagation is fast, partial healing at crack mouth will appear because the capillary force might not be large enough to suck healing agent to fulfil the space above the self-healing unit. The scenario with partial healing at crack tip appears when short self-healing units are used and the self-healing beam is designed to capture the deep cracks. In that case, the required volume of healing agent flow into the crack is not necessary equal to the volume of the crack space.

A detail version of the crack healing regime study can be conducted in the future to find out the reliability of healing effect. This recommend study is based on a notice that there are possibilities where fully bonding is not established in the healing zone because chemical properties of healing agent can be changed during storing or manufacturing process. For this study, numerical simulations with finite element

182

method, where properties of elements represent for healing agent are randomly assigned, can be adopted to simulate effect of different healing degree.

6.2.5 Novel self-healing system for reinforced concrete

One of the drawbacks of the current tubular based self-healing system in reinforced concrete is caused by healing agent. Since the healing agent is one-part air-curing adhesive, it is not effective for deep cracks where the contact of healing agent and the surrounding air is very limited. Because of this drawback, micro-capsulated system, where less constraint on healing agent are imposed, has been attracting the concentration of researchers as an alternative for the current tubular system. However, finding an effective protection method and ways to position micro-capsules are still very challenging issues. One possible solution for the above problems is to develop a hybrid tubular-micro-capsulated system as shown in Figure 6.2.
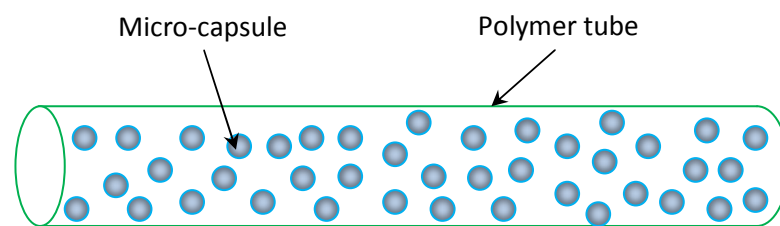
Figure 6.2: Hybrid tubular-micro-capsulated self-healing system

In this hybrid system, micro-capsules are contained in a thin polymer tube. The polymer tube is implemented to serve two purposes: (i) it acts as a barrier to protect the micro-capsules during casting process; and (ii) it provide tool to position the micro-capsules. Material for the polymer tube is chosen such that it will be melted under the heat generated from curing process of concrete. After the melt of the

polymer tube, micro-capsules are released and functional as normal in the micro-capsulated system.

References

Abaqus version 6.7 EF1 - User Manual, 2007. Simulia Inc.

Aragon A.M., Wayer J.K., Geubelle P.H., Goldberg D.E., White S.R. (2008). Design of microvascular flow networks using multi-objective genetic algorithms. *Comput. Methods Appl. Mech. Eng.* **197(49–50)**:4399–4410.

Askes H., M. Stroeven, Sluys L. J. (2004). Numerical determination of representative volumes for granular materials. *Comput. Methods Appl. Mech. Engrg.* **193**:3221 – 3238.

Bagheri R., Marouf B.T., Pearson R.A. (2009). Rubber-toughened epoxies: a critical review. *J. Macromolecular Sci. Part C: Polym. Rev.* **49**:201-22.

Bagheri R., Pearson R.A. (1996). Role of particle cavitation in rubbe-toughened epoxies: I. Microvoid toughening. *Polymer* **37**:4529-4538.

Bagheri R., Pearson R.A. (1995). Interfacial studies in CTBN-modified epoxy. *J. Appl. Polym. Sci.* **58**:427-437.

Bazant Z.P., Oh B.H. (1983). Crack band theory for fracture of concrete. *Materials and Structures* **16**:155-77.

Bazant Z.P., Planas P. (1998). Fracture and size effect in concrete and other quasibrittle materials. C.R.C Press, Boca Raton.

Becu L., Maazous A., Sautereau H., Gerard J.F. (1997). Fracture behaviour of epoxy polymers modified with core-shell rubber particles. *J. Appl. Polym. Sci.* **65**:2419-2431.

Belytschko T., Fish J. and Bayliss A. (1990). The spectral overlay on finite elements for problems with high gradients. *Comput. Methods Appl. Mech. Engrg.* **81**:71 – 89.

Benveniste Y. (1987). A new approach to the application of Mori–Tanaka's theory in composite materials. *Mech Mater.* **6**:147–57.

Blaiszik B.J., Caruso M.M., McLroy D., Moore J., White S.R. and Sottos N.R. (2009). Microcapsules filled with reactive solutions for self-healing materials. *Polymer* **50**: 990-997.

Bleay S. M., Loader C. B., Hawyes V. J., Humberstone L., Curtis P.T. (2001). A smart repair system for polymer matrix composites. *Composites A* **32**:1767-1776.

Bond I. P., Trask R. S.,Williams G. J. (2007). Bioinspired self-healing of advanced composite structures using hollow glass fibres. *J. R. Soc Interface* **4**:363-371.

Brown E. N., Sottos N. R., White S. R. (2002). Fracture testing of a self-healing polymer composite. *Experimental Mechanics* **42:**372-379.

Brown E. N., Kessler M. R., Sottos N. R., White S. R. (2003). In situ poly (urea-formaldehyde) microencapsulation of dicyclopentadiene. *Journal of Microencapsulation* **20**: 719-730.

Brown E. N., White S. R., Sottos N. R. (2004). Microcapsule induced toughening in a self-healing polymer composite. *J. Mater. Sci.* **39:**1703-1710.

Brown E. N., White S. R., Sottos N. R. (2005a). Retardation and repair of fatigue cracks in a microcapsule toughened epoxy composite - Part 1: Manual infiltration. *Composites Science and Technology*, Special Anniversary Issue **65**: 2466-2473.

Brown E. N., White S. R., Sottos N. R. (2005b). Retardation and repair of fatigue cracks in a microcapsule toughened epoxy composite - Part 2: In situ self-healing. *Composites Science and Technology*, Special Anniversary Issue **65**: 2474-2480.

Budiansky B. (1965). On the elastic moduli of some heterogeneous materials. *J. Mech. Phys. Solids* **13**:223-227.

Cowie J., Glassert F.P. (1992). The reaction between cement and natural water containing dissolved carbon dioxide. *Adv Cement Res* **14**(15):119–134.

Caruso M. M., Delafuente D. A., Ho V., Moore J. S., Sottos N. R., and White S. R. (2007). Solvent-promoted self-healing materials. *Macromolecules* **40**: 8830-8832.

Caruso M.M., Blaiszik B.J., White S.R., Sottos, N.R. and Moore J.S. (2008). Full recovery of fracture toughness using a non-toxic solvent-based self-healing system. *Advanced Functional Materials* **18**: 1898-1904.

Chen, X., Dam, M. A., Ono, K., Mal, A. K., Shen, H., Nutt., S. R., Sheran, K. & Wudl, F. (2002). A thermally re-mendable cross-linked polymeric material. *Science* **295:**1698-1702.

Chen X. H., Mai, Y. W. (1998). Micromechanics of rubber – toughened polymers. *J. Mater. Sci.* **33**:3529 – 3539.

Chen T.K., Jan Y.H. (1995). Fracture behaviour of rubber mounted high temperature epoxies. *Polym. Eng. Sci* **35**:778-785.

Chung C. M., Roh, Y. S. Cho S. Y. (2004). Crack healing in polymeric materials via photochemical [2+2] cycloaddition, *Chemistry of Materials*, **16:**3982-3984.

Christensen R. M. (1990). A critical evaluation of a class of micro-mechanics models. *J. Mech. Phys. Solids* **38:**379-404.

Christopher W. B., Kyle. A. W., Andrew. J. B. (2007). Towards electrically conductive, self-healing materials. *J. R. Soc Interface* **4**:359-362.

Collini L., Nicoletto G. (2003). Micromechanical modeling of the behavior of nodular cast iron and comparison with experiments. *Proc.* XXXII AIAS Congress.

Crisfield M.A. (1986). Snap-through and snap-back response in Concrete structures and the dangers of under-integration. *Inter. J. for Numerical Methods in Engineering* **22**:751–767.

David Taylor, Hazenberg J. G., Lee T. C. (2007). Living with cracks: Damage and repair in human bone. *Nature Material* **6**:263-268.

De Muynck W., Debrouwer D., De Belie N., Verstraete W. (2008). Bacterial carbonate precipitation improves the durability of cementitious materials. *Cement and Concrete Research* **38**:1005-1014.

Delves L.M. and Hall C.A. (1979). An implicit matching principle for global element calculations. *J. Inst. Math. & Appl.* **23**:223-234.

Delves L.M. and Philips C. (1980). A fast implementation of the global element method. *J. Inst. Math. & Appl.* **25**:177-197.

Dong S.B. (1983). Global-local finite element methods. in: *State-of-the-Art on Finite Element Technology*, edited by A.K. Noon, American Society of Mechanical Engineers: 451-474.

Drago A., Pindera M. J. (2007). Micro-macromechanical analysis of heterogeneous materials: Macroscopically homogeneous vs. periodic microstructures. *Composites Sci. and Tech.* **67**:1243-1263.

Drugan W. J., Willis J. R. (1996). A micromechanics-based nonlocal constitutive equation and estimates of representative volume element size for elastic composites. *J. Mech. Phys. Solids* **44**:497–524.

Dry C. M. (1992). Smart materials which sense, activate and repair damage; hollow porous fibres in composites release chemicals from fibers for self-healing, damage prevention and /or dynamic control. *Proc 1st European Conf on Smart Struct and Mats, Glasgow, UK* 367-370, 1992.

Dry C. (1994). Matrix cracking repair and filling using active and passive modes for smart timed release of chemicals from fibres into cement matrices. *Smart Matls. & Structs.* **3**:118–123.

Dry C. (1996). Procedure developed for self-repair of polymer matrix composite materials. *Comp. Struct.* **35**:263–269.

Dry C. and McMillan W. (1996). Three-part methylmethacrylate adhesive system as an internal delivery system for smart responsive concrete. *Smart Matls. & Structs.* **5**:297–300.

Dry C. (2000). Three designs for the internal release of sealants, adhesives and waterproofing chemical into concrete to release. *Cem. and Conc. Res.* **30**:1969–1977.

Dry C. and Corsaw M.(2003). A comparison of the bending strength between adhesive and steel reinforced concrete with steel only reinforced concrete. *Cement and Concrete Research* **33**:1723-1727.

Edvardsen C. (1999). Water permeability and autogenous healing of cracks in concrete. *ACI Mater J* **96**:448–55.

REFERENCES

El-Hadek M. A., Tippur H. V. (2002). Simulation of porosity by microballoon dispersion in epoxy and urethane: mechanical measurements and models. *J. Mater. Sci.* **33**:1649-1660.

Ellyin F., Grufman C. (2008). Numerical modelling of damage susceptibility of an inhomogeneous representative material volume element of polymer composites. *Comp. Sci. Technol.* **68**:650-657.

Eshelby J. D. (1957). The determination of the elastic field of an ellipsoidal inclusion and related problems. *Proc Roy Soc A* **241**:376–396.

Farage M.C.R., Sercombe J., Galle C. (2003). Rehydration and microstructure of cement paste after heating at temperatures up to 300°C. *J Cement Concrete Res* **33**:1047–1056.

Feyel F., Chaboche JL.(2000). FE2 multiscale approach for modelling the elastoviscoplastic behaviour of long fibre SiC/Ti composite materials. *Comput. Methods Appl. Mech. Engrg.* **183:**309-330.

Fish J., Belsky V., Pandheeradi M. (1996). Composite grid method for hybrid systems. *Computer methods in applied mechanics and engineering* **135**:307-325.

Fish J., Suvorov A., Belsky V. (1997). Hierarchical composite grid method for global – local analysis of laminated composite shells. *Applied numerical mathematics* **23**, 241-258.

Gent A.N. (2001). Engineering with rubber: how to design rubber components. Hanser. ISBN 3-446-21403-8.

Gitman I. M., Gitman M. B., Askes H. (2006). Quantification of stochastically stable representative volumes for random heterogeneous materials. *Arch. Appl. Mech.* **75**:79-92.

Gitman I. M., Askes H., Sluys L. J. (2007): Representative volume: existence and size determination. *Engrg. Frac. Mech.* **74:**2518-2534.

González C., Segurado C. and LLorca J. (2004): Numerical simulation of elasto-plastic deformation of composites: Evolution of stress microfields and implications for homogenization models. *J. Mech. and Phys. Solids* **52**:1573-1593.

González C. and Llorca J. (2007). Virtual fracture testing of fiber-reinforced composites: A computational micromechanics approach. *Engrg. Frac. Mech.* **74:**1126-1138.

Ghosh P., Mandal S., Chattopadhyay B.D., Pal S. (2005). Use of microorganism to improve the strength of cement mortar. *Cement Concrete Res* **35**:1980-1983.

Ghosh S., Bai J., Raghavan P. (2007). Concurrent multi-level model for damage evolution in microstructurally debonding composites. *Mechanics of Materials* **39**:241–266.

Guild F.J. and Kinloch A.J. (1995). Modelling the properties of rubber-modified epoxy polymers. *J. Mat. Sci.* **30**:1689-1697.

Gusev A. A. (1997). Representative volume element size for elastic composites: a numerical study. *J Mech Phys Solids* **45**:1449–1459.

Hansen C.J., Wu W., Toohey K.S., Sottos N.R., White S.R., Lewis J.A. (2009). Self-healing materials with interpenetrating microvascular networks. *Adv. Mater.* **21(41)**:4143–4147.

Hashin Z. (1983). Analysis of composite materials – a survey. *J. Appl. Mech.* **50**:154-166.

Hayes S. A., Jones F. R., Marshiya K., Zhang W. (2005). Self-Healing composite materials, *Proc 15th Int. Conf. on Composite Materials*, *Durban, South Africa,* 27 June-01 July 2005.

Hayes S. A., Jones F. R., Marshiya K., Zhang W. (2007). A self-healing thermosetting composite material. *Composites A* **38**:1116-1120.

Heide T., Schlangen N., van Breugel K. (2006). Crack healing of early age cracks in concrete. Measuring, Monitoring and Modelling Concrete Properties. Springer, the Netherland. ISBN-10 1-4020-5103-4.

Hill R. (1965). A self-consistent mechanics of composite materials. *J. Mech. Phys. Solids* **13:**213-222.

Hillerborg A, Modeer M, Peterson PE (1976). Analysis of crack formation and crack growth in concrete by means of fracture mechanics and finite elements. *Cement Concrete Res.* **6**: 773-782.

Hirai I., Uchiya Y., Mizuta Y. (1985). An exact zooming method, *Finite Elements in Analysis and Design* **1:** 61-69.

Huang C. Y., Williams H. R., Trask R. S., Bond I. P. (2007). Self-healing composites incorporating microvascular networks. *Proc 1st Int. Conf. on Self Healing Materilas*, *Noordwijk aan Zee, Netherlands,* 18-20 April 2007.

Huet C. (1990). Application of variational concepts to size effects in elastic heterogeneous bodies. *J. Mech. Phys. Solids* **38**:813–841.

Jacobsen S., and Sellevold E.J. (1996). Self healing of high strength concrete after deterioration by freeze/thaw. *Cement and Concrete Research* **26**: 55-62.

Janssen M, Zuidema J, Wanhill RJH. Fracture mechanics, 2nd Edition. Spon Press, London and New York, 2004.

Jefferson A., Joseph C., Lark R., Isaacs B., Dunn S., Weager B. (2010). A new system for crack closure of cementitious materials using shrinkable polymers. *Cement and Concrete Research* **40**:795-801.

Jin H., Miller G.M., Sottos N.R., White S.R. (2011). Fracture and Fatigue Response of a Self-Healing Epoxy Adhesive. *Polymers* **52**: 1628-1634.

Jin H., Mangun C.L., Stradley D.S., Moore J.S., Sottos N.R. and White S.R. (2012) Self-healing thermoset using encapsulated epoxy-amine healing chemistry. *Polymer*. DOI: 10.1016/j.polymer.2011.12.005

Jones F. R., Hayes S. A., Zhang W., Branthwaite M. (2007). Self-healing of damage in fibre-reinforced polymer-matrix composites. *J. R. Soc Interface* **4**:381-387.

Jones A. S., Rule J. D., Moore J. S., Sottos N. R., White S. R. (2007). Life extension of self-healing polymers with rapidly growing fatigue cracks. *J. R. Soc Interface* **4**: 395-403.

Jonkers H.M. (2007). Crack repair by concrete-immobilized bacteria. In "Self Healing Materials: An Alternative Approach to 20 Centuries of Materials Science". Springer, Netherland. ISBN 978-1-4020-6249-0.

Jonkers H.M., Schlangen E. (2008). Development of a bacteria-based self-healing concrete. In "Tailor Made Concrete Structure". Taylor & Francis Group. London. ISBN 978-0-415-47535-8.

Jonkers H.M., Schlangen E. (2009). Towards a sustainable bacterially-mediated self healing concrete. *Proc 2nd Int. Conf. on Self Healing Materilas*, *Chicago, USA,* 28 June - 01 July 2009.

Joseph C., Jefferson A.D., Cantoni M.B. (2007). Issues relating to the autonomic healing of cementitious materials. *Proc 1st Int. Conf. on Self Healing Materilas*, *Noordwijk aan Zee, Netherlands,* 18-20 April 2007.

Kari S., Beger H., Rodriguez-Ramos R., Gabbert U. (2007). Computational evaluation of effective material properties of composites reinforced by randomly distributed spherical particles. *Composite Structures* **77**:223–231.

Keller M. W., Sottos N. R. (2006). Mechanical properties of microcapsules used in a self-healing polymer. *Exp. Mech.* **46**: 725-733.

Keller M. W., Beiermann B. A., White S. R., Sottos N. R. (2007). Fatigue of self-healing elastomer. *Proc 1st Int. Conf. on Self Healing Materilas*, *Noordwijk aan Zee, Netherlands,* 18-20 April 2007.

Keller M.W., White S.R. and Sottos N.R. (2008). Torsion fatigue of a self-healing poly(dimethyl siloxane) elastomer. *Polymer* **49**: 3136-3145.

Kersey F. R., Loveless D. M. and Craig S. L. (2007). A hybrid polymer gel with controlled rates of cross-link rupture and self-repair. *J. R. Soc Interface* **4**:373-380.

Kessler M. R., White S. R. (2001). Self-activated healing of delamination damage in woven composites. *Composites A* **32:**683-699.

Kessler M. R., Sottos N. R.,White S. R. (2003). Self-healing structural composite materials. *Composites A* **34:**743-753.

Kim S., Lorente S., Bejan A. (2006). Vascularizedmaterials: tree-shaped flow architectures matched canopy to canopy. *J. Appl. Phys.* **100(6)**:63525.

Kingsbury C.M., May P.A., Davis D.A., White S.R., Moore J.S. and Sottos N.R. (2011) [Shear activation of mechanophore-crosslinked polymers](). *Journal of Materials Chemistry*. Published online on 17 February 2011. DOI: 10.1039/c0jm04015k.

Kishi T., Ahn T.H., Hosoda A., Suzuki S., Takaoka H. (2007). Self-healing behavior by cementitious recrystallization of cracked concrete incorporating expansive agent. *Proc 1st Int. Conf. on Self Healing Materilas*, *Noordwijk aan Zee, Netherlands,* 18-20 April 2007.

Kotsovos D, Pavlovic M.N. (1995). Structural concrete: Finite element analysis for limit state design. Thomas Telford, ISBN-10: 0727720279.

Kryger M.J., Ong M.T., Odom S.A., Sottos N.R., White S.R., Martinez T.J. and Moore J.S. (2010). Masked Cyoanoacrylates Unveiled by Mechanical Force. *Journal of American Chemical Society*, **132**: 4558-4559.

Kuna M. and Sun D.Q. (1996). Analyses of void growth and coalescence in cast iron by cell model. *Journal de Physique IV* **6**:113-122, 1996.

Lemaitre J. (1987). Continuum damage mechanics theory and applications. Springer, Berlin Heidelberg, New York.

Li V. C., Lim Y. M., Chan Y. W. (1998). Feasibility of a passive smart self-healing cementitious composite. *Composites B* **29B**:819-827.

Li V. C. (2007). Self-healing in concrete materials. In "Self Healing Materials: An Alternative Approach to 20 Centuries of Materials Science". Springer, Netherland. ISBN 978-1-4020-6249-0.

Lorente S., Bejan A. (2009). Vascularized smart materials: designed porous media for self-healing and self-cooling. *J. Porous Media* **12(1)**:1–18.

Martha J. H. (2005). Closing wounds [online]. American Institute of Physics. Available from: http://www.aip.org/dbis/stories/2005/14390.html [Accessed 14 March, 2008].

Mauldin T. C., Rule J. D., Sottos N. R., White S. R., Moore J. S. (2007). Self-healing kinetics and the stereoisomers of dicyclopentadiene. *J. R. Soc. Interface* **4**,389–393.

McIlroy D.A., Blaiszik B.J., Caruso M.M., White S.R., Moore J.S. and Sottos N.R. (2010). Microencapsulation of a reactive liquid-phase amine for self-healing epoxy composites. *Macromolecules* **43**: 1855-1859.

Margolina A., Wu S. (1988). Percolation model for brittle-tough transition in nylon-rubber blends. *Polymer* **29**:2170-2173.

Michel, J.C., Moulinec, H., Suquet, P. (1999). Effective properties of composite materials with periodic microstructure: a computational approach. *Comput. Methods Appl. Mech. Eng.* **172**:109–143.

Mishnaevsky Jr L, Dong M., Hoenle S., and Schmauder S. (1999). Computational mesomechanics of particle reinforced composites. *Computational Materials Science* **16**:133-143.

Mishnaevsky Jr L., Lippmann N. and Schmauder S. (2003a). Computational modelling of crack propagation in real microstructures of steels and virtual testing of artificially designed materials. *International journal of fracture*, **120**:581-600.

Mishnaevsky Jr L., Lippmann N. and Schmauder S. (2003b). Micromechanisms and modelling of crack initiation and growth in tool steels: role of primary carbides. *International Journal of Materials Research*, **94**:676-681.

Mori T. and Tanaka K. (1973). Average stresses in matrix and average energy of materials with misfitting inclusions. *Acta Metall.* **21:**571-574.

Mostovoy S., Crosley P. B., Ripling E.J. (967): Use of crack-line loaded specimens for measuring plain-strain fracture toughness. *J. Mater.* **2**: 661-681.

Mote C.D.: Global-local finite element (1971). *lnternat. J. Numer. Meths. Engrg.* **3**: 565-574.

Motuku M., Vaidya U. K., Janowski G. M. (1999). Parametric studies on self-repairing approaches for resin infused composites subjected to low velocity impact.: *Smart Matls. & Structs.* **8**:623-638.

REFERENCES

Muliana A. H., Kim J. S. (2007). A concurrent micromechanical model for predicting nonlinear viscoelastic responses of composites reinforced with solid spherical particles. *Inter. J. Solids and Struct.* **44**:6891-6913.

Nanayakkara A. (2003). Self-healing of cracks in concrete subjected to water pressure. Symposium on new technologies for urban safety of mega cities in Asia. Tokyo, Japan, 2003.

Nemat-Nasser S., Hori M. (1999). Micromechanics: Overall Properties of Heterogeneous Materials, second ed. Elsevier.

Ostoja-Starzewski M. (1998). Random field models of heterogeneous materials. *Int J Solids Struct* **35**:2429–2455.

Ostoja-Starzewski M. (1999). Scale effects in materials with random distributions of needles and cracks. *Mech Mater* **31**:883–893.

Ostoja-Starzewski M. (2002). Microstructural randomness versus representative volume element in thermomechanics. *ASME J. Appl Mech.* **69**:25–35.

Pang J. W. C. & Bond I. P. (2005a). Bleeding composites - damage detection and self-repair using a biomimetic approach. *Composites A* **36**:183–188.

Pang J. W. C. & Bond I. P. (2005b). A hollow fibre reinforced polymer composite encompassing self-healing and enhanced damage visibility. *Compos. Sci. Technol.* **65**:1791–1799.

Patel A. J., Sottos N. R., White S. R. (2007). Self-healing composites for mitigation of low-velocity impact damage. *Proc 1st Int. Conf. on Self Healing Materilas*, *Noordwijk aan Zee, Netherlands,* 18-20 April 2007.

Patel A.J., Sottos N.R., Wetzel E.D. and White S.R. (2009). Autonomic healing of low-velocity impact damage in fiber-reinforced composites. *Composites: Part A* **41**: 360-368.

Pelissou C, Baccou J, Monerie Y, Perales F.(2009). Determination of the size of the representative volume element for random quasi-brittle composites. *Inter. J. Solids and Struct.* **46**:2842-2855.

Pearson R.A., Yee A.F. (1986). Toughening mechanisms in elastomer-modified epoxies: Part 1: Mechanical properties. *J. Mater. Sci* **21**:2462-2474.

Pierard O., Llorca J., González C., Segurado J., Doghri I. (2007a). Micromechanics of elasto-plastic materials reinforced with ellipsoidal inclusions. *Inter. J. Solids and Struct.* **44**:6945-6962.

Pierard O., LLorca J., Segurado J. and Doghri I. (2007b). Micromechanics of particle-reinforced elasto-viscoplastic composites: Finite element simulations versus affine homogenization. *Inter. J. of Plasticity* **23**:1041-1060, 2007b.

Pindera M. J., Drago A. (2007). Micro-macro mechanical analysis of heterogeneous materials: Macroscopically homogeneous vs periodic microstructure. *Composites Science and Technology* **67**:1243-1263.

Ramachandran S.K., Ramakrishnan V., Bang S.S. (2001). Remediation of concrete using micro-organisms. *ACI Mater J* **98**:3-9.

Reinhardt H-W and Loos M. (2003). Permeability and self-healing of cracked concrete as a function of temperature and crack width. *Cement and Concrete Research* **33**:981-985.

Reuss A. (1929). Berechnung der fliessgrenze von mischkristallen auf grund der plastizita¨tsbedingung fu¨ r Einkristalle. Z Angew. *Math. Mech.* **9**:49–58.

Rule J. D., Sottos N. R., White S. R. (2007). Effect of microcapsule size on the performance of self-healing polymers, *Polymer* **48**: 3520-3529.

Science Daily (May 25, 2010): Self-healing concrete: Research yields cost-effective system to extend life of structures.

Segurado J. and LLorca J. (2002): A numerical approximation to the elastic properties of sphere-reinforced composites. *J. Mech. and Physics of Solids* **50:**2107-2121.

Segurado J., González C. and LLorca J. (2003). A numerical investigation of the effect of particle clustering on the mechanical properties of composites. *Acta Materialia* **51:**2355-2369.

Segurado J. and LLorca J. (2004). A new three-dimensional interface finite element to simulate fracture in composites. *Inter. J. Solids and Struct.* **41:**2977-2993.

Segurado J. and LLorca J. (2005). A computational micromechanics study of the effect of interface decohesion on the mechanical behavior of composites. *Acta Materialia* **53**:4931-4942.

Segurado J. and LLorca J. (2006). Computational micromechanics of composites: The effect of particle spatial distribution. *Mechanics of Materials* **38**:873-883.

Sharma R., Socrate S. (2009). Micromechanics of uniaxial tensile deformation and failure in high impact polystyrene. *Polymer* **50**:3386-3395.

Song G., Ma N., Li H.N. (2006). Application of shape memory alloys in civil structures. *Engineering Structures* **28**:1266-1274.

Sun C. T. and Vaidya R. S. (1996). Prdiction of composite properties from a representative volume element. *Composites Science and Technology* **56**:171-179.

Takano N., Zako M., Kubo K., Kimura K. (2003). Microstructure-based stress analysis and evaluation for porous ceramics by homogeneization method with digital image-based modelling. *Int. J. Sol. Struct.*: **40**: 1225-1242.

Taya M. and Chou T. W. (1981). On two kinds of ellipsoidal inhomogeneities in an infinite elastic body: An application to a hybrid composite. *Int. J. Solids Struct.* **17**: 553-563.

Terada K., Hori M., Kyoya T., Kikuchi N. (2000). Simulation of the multi-scale convergence in computational homogenization approaches. *Inter. J. Solids and Struct.* **37**:2285-2311.

Toohey K. S., White S. R., Lewis J. A., Sottos N. R. (2007). Development of a protocol for microvascular self-healing. *Proc 1st Int. Conf. on Self Healing Materilas*, *Noordwijk aan Zee, Netherlands,* 18-20 April 2007.

Toohey K. S., Sottos N. R., Lewis J. A., Moore J. S., and White S. R. (2007). Self-healing materials with microvascular networks. *Nature Materials* **6**:581-585.

Toohey K.S., Sottos N.R., White S.R. (2009). Characterization ofmicrovascular-based self-healing coatings. *Exp. Mech.* **49(5)**:707–717.

Trask R. S. and Bond I. P. (2006). Biomimetic self-healing of advanced composite structures using hollow glass fibres. *Smart Mat. & Struct.* **15**:704-710.

Trask R. S., Bond I. P. and Semprimoschnig C. O. A. (2006a). Enabling self-healing capabilities – a small step to bio-mimetic materials. *ESA Technical Note, Materials Report Number 4476*.

Trask R. S., Bond I. P. and Semprimoschnig C. O. A.: Bioinspired self-healing of advanced composite structures in a space environment submitted to J. AIAA, 2006b.

Van Mier J.G.M. *Fracture processes of concrete.* C.R.C Press, Boca Raton, 1997.

Van Tittelboom K., De Belie N., De Muynck W., Verstraete W. (2010). Use of bacteria to repair cracks in concrete. *Cement and Concrete Research* **40**:157-166.

Voigt W. (1989). U ber die Beziehung zwischen den beiden Elastizita¨tskonstanten isotroper Ko¨ rper. *Wied Ann Physik* **38**:573–587.

Wang, H, Qian Z, Liu S., Wu J, Wong C. P., Okuno A. (1999). Mechanical modelling of underfills based on two-phase composites. *Electronic Component and Technology Conference*.

Weng G. J. (1984). Some elastic properties of reinforced solids, with special reference to isotropic ones containing spherical inclusions. *Int. J. Eng. Sci.* **22**:845–856.

White S., Sottos N., Geubelle P., Moore J., Kessler M., Sriram S., Brown E., Viswanatham S. (2001). Autonomic healing of polymer composites. *Nature* **409**:794–797.

Whitney J..M. (1985). Stress Analysis of the double cantilever beam specimen. *Composites Science and Technology* **23**:201-219.

Wilson G.O., Moore J.S., White S.R., Sottos, N.R., Anderssom H.M. (2008). Autonomic healing of epoxy vinyl esters via ring opening metathesis polymerization. *Adv. Funct. Mater.* **18**: 44-52.

198

Wilson G.O., Porter K.A., Weissman H., Wilson S.R., White S.R., Sottos N.R. and Moore, J.S. (2009). Stability of second generation grubbs' alkylidenes to primary amines: formation of novel ruthenium-amine complexes. *Advanced Synthesis & Catalysis* **351**, 1817-1825.

Wilkins D.J. (1983). A preliminary damage tolerance methodology for composite structures. *Failure Analysis and Mechanisms of Failure of Fibrous Composite Structures*, **NASA CP-2278**, 67-93.

William M. (2007) Blood clot formation [online]. U.S. National Library of Medicine. Available from: http://www.nlm.nih.gov/medlineplus/ency/imagepages/19462.htm [Accessed 14 March, 2008].

Williams H. R., Bond I. P., Trask R. S. (2007). Design of vascular networks for self-healing sandwich structures. *Proc 1st Int. Conf. on Self Healing Materilas*, *Noordwijk aan Zee, Netherlands,* 18-20 April 2007.

Williams H.R., Trask R.S., Weaver P.M., Bond I.P. (2008a). Minimum mass vascular networks in multifunctional materials. *J. R. Soc. Interface 5*, **18**:55–65.

Williams H.R., Trask R.S., Knights A.C., Williams E.R., Bond I.P. (2008b). Biomimetic reliability strategies for self-healing vascular networks in engineering materials. *J. R. Soc. Interface 5*, **24**:735–747.

Williams H.R., Trask R.S., Bond I.P. (2008c). Self-healing sandwich panels: restoration of compressive strength after impact. *Compos. Sci. Technol.* **68**: 3171–3177.

Wu W., Hansen C. J., Aragon A. M., Sottos N. R., White S. R., Geubelle G. H., Lewis J. A. (2007). Direct ink writing of microvascular networks. *Proc 1st Int. Conf. on Self Healing Materilas*, *Noordwijk aan Zee, Netherlands,* 18-20 April 2007.

Xia Z., Zhang Y., Ellyin F. (2003). A unified periodical boundary conditions for representative volume elements of composites and applications. *Inter. J. Solids and Struct.* **40**:1907-1921.

Yang Y., Lepech M.D., Yang E.H., and Li V.C. (2009). Autogenous Healing of Engineering Cementitious Composites under Wet-Dry Cycles. *J. Cement and Concrete Research* **39**:382-390.

Yang Z., Hollar J., He X., Shi X. (2011). A self-healing cementitious composite using oil core/silica gel shell microcapsules. *J Cement & Concrete Composite* **33**:506-512.

Zako M. and Takano N. (1999). Intelligent material systems using epoxy particles to repair microcracks and delamination damage in GFRP. *J Int Mat Sys & Struc.* **10**:836-841.

Zhang H.L., Lorente S., Bejan A. (2007). Vascularization with trees that alternate with upside-down trees. *J. Appl. Phys.* **101(9)**:094904.

Appendix 1

MATERIAL SAFETY DATA SHEET – POR15

Material Safety Data Sheet   POR-15, Inc. PO Box 1235, Morristown, NJ 07962-1235
Emergency telephone numbers: Chemtrec 800-424-9300, 973-887-1999, 800-457-6715, 973-539-3236

PRODUCT NAME: POR-15 Rust Preventive Paint
CHEMICAL NAME: Isocyanate Prepolymer based on MDI
CHEMICAL FAMILY: Solution Aromatic Isocyanates (26447-40-5)

FORMULA: Mixture
T.S.C.A. STATUS: Ok
TRADE NAMES/SYNONYMS: POR-15 Rust Paint, POR-15 Paint

II. HAZARDOUS INGREDIENTS

Diphenylmethane Diisocyanate(MDI)(26447-40-5)%:ca 20
Naptha Petroleum (68333-23-3)

Current TLV: ACGIH: 0.005ppm(0.2 mg/m^3)
Ceiling value OSHA (PEL): Same

III. PHYSICAL DATA

BOILING POINT: 232 Degrees F
VAPOR PRESSURE: 38mm Hg
VAPOR DENSITY: (Air = 1) 4.5
SOLUBILITY IN WATER: Nil
ODOR: Aromatic   LBS. PER GALLON: 8.9
VISCOSITY: Range @ 77^0 F/25^{0}C: 200-500 CPS

SPECIFIC GRAVITY: (Water =1) 1.6
% VOLATILE BY VOLUME: 26%
EVAPORATION RATE (Ether = 1): For solvent, 4.5
COLOR: Black, Silver, Clear (light brown trans)
VOLATILE ORGANICS: For POR-15 Clear - 236 grams per liter
                For POR-15 Silver & Black - 223 grams per liter

IV. FIRE & EXPLOSION HAZARD DATA

FLASH POINT (Method used): TCC 104 Degrees F
EXTINGUISHING MEDIA: Dry chemical (e.g.monoammonium phosphate, potassium sulfate, and potassium chloride, carbon dioxide, high expansion (proteninic) chemical foam, water spray for large fires.
SPECIAL FIRE FIGHTING PROCEDURES/USUAL FIRE OR EXPLOSION HAZARDS: Full emergency equipment with self-contained breathing apparatus should be worn by firefighters. During a fire, MDI vapors and other irritating, toxic gases may be generated by thermal decomposition (see section VIII). At temperatures greater than 400 degrees F (204 degrees C), polymeric MDI can polymerize and decompose. Use cold water to cool fire-exposed containers.
HAZARD CLASS: B   HEALTH: 3   FIRE: 2   REACTIVITY: 1   FLAMMABLE LIMITS LEL: 1%   FLAMMABLE LIMITS UEL: 7.1%

V. HEALTH HAZARD DATA

THRESHOLD LIMIT VALUE: For isocyanates, 0.02ppm; for solvent, 200ppm
EFFECTS OF OVEREXPOSURE: Eyes-severe irritation; tearing skin, discoloration-drying; breathing-irritation, dizziness, unconsciousness (for solvent). For isocyanates, coughing, irritation of mucous membranes and respiratory tract.
SKIN EFFECTS: Slight to moderate irritation(MDI); skin sensitizer in guinea pigs(MDI). No conclusive evidence has been developed to indicate that MDI or POR-15 is carcinogenic, teratogenic or that either one causes reproductive effects in animals or humans. MDI has been reported by NIOSH to be mutagenic to Salmonella Typhimurium bacteria in the presence of a mammalian liver activation system. There is not full agreement in the scientific community on the significance of these Ames test results and their relationship to human safety in assessing the risk of cancer in man. A commitment has been made to perform an animal life-time inhalation study on polymeric MDI.
HUMAN EFFECTS OF OVEREXPOSURE: INHALATION-Inhalation of MDI vapors or aerosols in concentrations above 0.02ppm can produce irritation of the mucous membranes in the respiratory tract, running nose, sore throat, productive cough and a reduction of lung function. Extensive exposures to concentrations well above the TLV could lead to bronchitis, bronchial spasm and pulmonary edema. These effects are usually reversible. However, due to low volatility, high exposures are not anticipated except if the material is overheated or sprayed as an aerosol into the air. Hypersensitivity pneumonitis has also been reported. Another type of response is hyperreactivity or hypersensitization. Persons with a preexisting unspecific bronchial hyperreactivity or persons with a specific isocyanate hypersensitivity (as a result of previous repeated overexposure or a single large dosage) will respond to small isocyanate concentrations at levels well below the TLV of 0.02ppm. Symptoms could be immediate or delayed and include chest tightness, respiratory distress or asthmatic attack. SKIN: Polymeric MDI reacts with skin protein and tissue moisture and can cause localized irritation as well as discoloration. Prolonged contact could produce reddening, swelling, or blistering and, in some individuals, skin sensitization resulting in dermatitis. EYES: Liquid, vapors, or aerosols are irritating to the eyes and can cause lachrymation (tearing effect). Corneal damage can occur; however, indications are that the damage is reversible and does not result in permanent injury. INGESTION: Ingestion could result in irritation and some corrosive action in the

VI. EMERGENCY & FIRST AID PROCEDURES

EYE CONTACT: Flush with clean, lukewarm water(low pressure) for at least 15 min., occasionally lifting eyelids; obtain medical attention.
SKIN CONTACT: Remove contaminated clothing. Wash affected areas thoroughly with soap and water. Wash contaminated clothing thoroughly before re-use.
INHALATION: Move to an area free from risk of further exposure. Administer oxygen or artificial respiration as needed. Obtain medical attention. Asthmatic-type symptoms may develop and may be immediate or delayed up to several hours. Treatment is essentially symptomatic.
INGESTION: Do not induce vomiting. Give 250 ml of milk or water to drink. DO NOT GIVE ANYTHING BY MOUTH TO AN UNCONSCIOUS PERSON. Consult physician.

VII. PROTECTION RECOMMENDATIONS

EYE PROTECTION: Safety glasses with side shields, splash goggles or face shield. Contact lenses should not be worn. SKIN PROTECTION: Chemical-resistant gloves. Cover as much of the exposed skin area as possible with appropriate clothing. If skin creams are used, keep the area covered to a minimum. RESPIRATORY PROTECTION: Use respirator that is recommended or approved for use in isocyanate containing environments (air purifying or fresh air supplied). Consider type of application and environmental concentrations. In spray applications you must protect against exposure to both vapor and spray mist. An air-supplied respirator is strongly recommended for spray application. Observe OSHA regulations for respirator use 29 CFR, 1910.134. VENTILATION: Ventilation as required to maintain air concentrations below TLV's. If material is spray-applied, ventilation should be provided and air supplied respirators worn. Exhaust air may need to be cleaned by scrubbers or filters to reduce environmental contamination.

VIII. REACTIVITY DATA

STABILITY: Stable under normal conditions. POLYMERIZATION: Will not occur in unopened cans under normal conditions. CONDITIONS TO AVOID: Temperatures below 32 degrees F (0°C) or above 122 degrees F (50 degrees C). To maintain freshness: Avoid contact with water, alcohols, amines, strong bases, metal compounds or surface active materials. HAZARDOUS DECOMPOSITION(typical of all paints): By fire, carbon dioxide, CO, oxides of nitrogen, traces of HCN, MDI., and elements unknown.

IX. SPILL OR LEAK PROCEDURES

STEPS TO BE TAKEN IN CASE MATERIAL IS RELEASED OR SPILLED: Eliminate source of ignition of vapors, wear protective clothing while cleaning up; absorb on sand, clay, or absorbent material. WASTE DISPOSAL METHOD: Dispose of in accordance with local, state, and federal regulations. Incineration is preferred. Decontaminate empty containers.

X. SPECIAL PROTECTION INFORMATION

RESPIRATORY PROTECTION: NIOSH/MSHA approved respirator. EYE PROTECTION: Goggles or face mask. VENTILATION: Use in well-ventilated areas only. Have adequate general exhaust. PROTECTIVE GLOVES: Solvent protective gloves. OTHER PROTECTIVE EQUIPMENT: Self-contained breathing apparatus if threshold limit is exceeded.

XI. SPECIAL PRECAUTIONS & STORAGE DATA

STORAGE TEMPERATURE (min/max): 32 degrees F (0 degrees C)/122 degrees F (50 degrees C)
AVERAGE SHELF LIFE: 6 months to 2 years (unopened can) @ 77 degrees F (25 degrees C)
SPECIAL SENSITIVITY(heat, light, moisture): If container is exposed to high heat, container may pressurize slightly. If container is opened and used as supply can, do not re-seal can as pressure may build up due to reaction producing carbon dioxide, which might cause re-sealed container to pressurize and burst.
PRECAUTIONS TO BE TAKEN IN HANDLING AND STORING: Store in tightly closed container and protect from moisture and foreign materials. At maximum storage temperatures noted, material may slowly polymerize without hazard. Ideal storage temperature range is 50-81 degrees F (10 - 27 degrees C).

Appendix 2

MATERIAL SAFETY DATA SHEET – AQUASTICK

Material Safety Data Sheet: AQUA STICK

Supercedes Date 10/19/2006   **Issuing Date** 04/12/2010

1. PRODUCT AND COMPANY IDENTIFICATION

Product Name AQUA STICK
Recommended Use Epoxy resin
Information on Manufacturer
Mega Metals,Partsmaster,Div of NCH Corp.

P.O. Box 655326
Dallas, TX 75265-5326

Product Code 57200500
Chemical Nature Phenolic resin
Emergency Telephone Number
CHEMTREC ® 800-424-9300

2. HAZARDS IDENTIFICATION

Emergency Overview
WARNING
Severe eye irritation
Causes skin irritation
May cause allergic skin reaction
Keep out of reach of children

Color Off white   **Physical State** Solid   **Odor** Amine-like
Potential Health Effects

Principle Route of Exposure	Eye contact, Inhalation, Skin contact.
Primary Routes of Entry	None known.
Acute Effects	
Eyes	Moderately irritating to the eyes.
Skin	May cause skin irritation. Repeated or prolonged skin contact may cause allergic reactions with susceptible persons.
Inhalation	Not hazardous by inhalation.
Ingestion	Low hazard for usual industrial or commercial handling.
Chronic Toxicity	May cause sensitization by skin contact
Target Organ Effects	No information available.
Aggravated Medical Conditions	Skin disorders
Potential Environmental Effects	See Section 12 for additional Ecological information.

3. COMPOSITION / INFORMATION ON INGREDIENTS

Component	CAS-No
Diglycidyl ether of bisphenol A	25085-99-8

The product contains no substances which at their given concentration, are considered to be hazardous to health

4. FIRST AID MEASURES

General Advice	Avoid contact with skin, eyes, and clothing.
Eye Contact	Rinse thoroughly with plenty of water, also under the eyelids. Get medical attention if irritation develops and persists.
Skin Contact	Wash off with plenty of water.
Inhalation	Not hazardous by inhalation .
Ingestion	No hazards which require special first aid measures.
Notes to Physician	Treat symptomatically.

5. FIRE-FIGHTING MEASURES

Flash Point   140°F/60°C   **Method**   Estimated
Autoignition Temperature No information available.
Upper No data available   **Lower** No data available
Suitable Extinguishing Media
Foam. Alcohol-resistant foam. Carbon dioxide (CO2). Dry chemical. Water.
Specific hazards arising from the chemical
The product causes irritation of eyes, skin and mucous membranes.
Protective Equipment and Precautions for Firefighters
As in any fire, wear self-contained breathing apparatus pressure-demand, MSHA/NIOSH (approved or equivalent) and full protective gear.

NFPA	Health 1	Flammability 2	Instability 0
HMIS	Health 1	Flammability 0	Instability 0

6. ACCIDENTAL RELEASE MEASURES

Personal Precautions	Avoid contact with the skin and the eyes.
Environmental Precautions	Do not flush into surface water or sanitary sewer system.
Methods for Containment	Pick up and arrange disposal without creating dust.
Methods for Cleaning Up	Pick up and transfer to properly labeled containers.
Neutralizing Agent	Not applicable.

7. HANDLING AND STORAGE

Handling	Avoid contact with skin, eyes, and clothing.
Storage	Keep away from open flames, hot surfaces and sources of ignition. Keep in a dry, cool and well-ventilated place.

Storage Temperature	**Minimum**	No information available	**Maximum**	<90°F/27°C
Storage Conditions	**Indoor** X	**Outdoor**	**Heated**	**Refrigerated**

8. EXPOSURE CONTROLS / PERSONAL PROTECTION

Exposure Guidelines   This product does not contain any hazardous materials with occupational exposure limits established by the region specific regulatory bodies.

Component	ACGIH TLV	OSHA PEL	NIOSH
Diglycidyl ether of bisphenol A	No data available	No data available	No data available

Engineering Measures	Not required.
Personal Protective Equipment	
Eye/Face Protection	Safety glasses with side-shields.
Skin Protection	Wear suitable protective clothing, Impervious gloves.
Respiratory Protection	None required under normal conditions of use .
General Hygiene Considerations	Ensure that eyewash stations and safety showers are close to the workstation location.

9. PHYSICAL AND CHEMICAL PROPERTIES

Physical State	Solid	**Viscosity**	Solid
Color	Off white	**Odor**	Amine-like
Appearance	Opaque	**pH**	Not applicable
Specific Gravity	1.97201	**Evaporation Rate**	Not applicable
Percent Volatile (Volume)	No information available	**VOC Content (%)**	<0.1
Vapor Pressure	No information available	**Vapor Density**	No information available
Solubility	Negligible	**Boiling Point/Range**	446°F/230°C

10. STABILITY AND REACTIVITY

Chemical Stability	Stable. Hazardous polymerization does not occur.
Conditions to Avoid	None known
Incompatible Products	None known.
Hazardous Decomposition Products	Oxides of Carbon, Nitrogen, and Sulfur, Aldehydes.
Possibility of Hazardous Reactions	Hazardous polymerization does not occur

11. TOXICOLOGICAL INFORMATION

Product Information   No information available.

Acute toxicity

Component	LD50 Oral	LD50 Dermal	LC50 Inhalation	Draize Test	Other
Diglycidyl ether of bisphenol A	no data available	no data available	no data available	no data available	no data available

Chronic Toxicity

Component	Mutagenicity	Sensitization	Developmental Toxicity	Reproductive Toxicity	Target Organ Effects
Diglycidyl ether of bisphenol A	no data available	no data available	no data available	no data available	no data available

Carcinogenicity   There are no known carcinogenic chemicals in this product.

Component	ACGIH	IARC	NTP	OSHA	Other
Diglycidyl ether of bisphenol A	not applicable	not applicable	not applicable	not applicable	not applicable

12. ECOLOGICAL INFORMATION

Product Information   No information available.

Component Information   No information available.

Component	Toxicity to Algae	Toxicity to Fish	Microtox	Water Flea	log Pow
Diglycidyl ether of bisphenol A	no data available	no data available	no data available	no data available	N/A

Persistence and Degradability	No information available.
Bioaccumulation	No information available.
Mobility	No information available.

13. DISPOSAL CONSIDERATIONS

Product Disposal   Dispose of in accordance with all Federal, state, and local regulations. .
Container Disposal   Do not re-use empty containers.

14. TRANSPORT INFORMATION

DOT   Not regulated

TDG   Not regulated

ICAO   Not regulated

IATA   Not regulated

IMDG/IMO   Not regulated

15. REGULATORY INFORMATION

Inventories
TSCA   Complies
DSL   Complies

U.S. Federal Regulations

SARA 313
Section 313 of Title III of the Superfund Amendments and Reauthorization Act of 1986 (SARA). This product does not contain any chemicals which are subject to the reporting requirements of the Act and and Title 40n of the Code of Federal Regulations, Part 372.

SARA 311/312 Hazardous Categorization

Acute Health Hazard	Chronic Health Hazard	Fire Hazard	Sudden Release of Pressure Hazard	Reactive Hazard
Yes	Yes	Yes	No	No

CERCLA

Component	Hazardous Substances RQs	CERCLA EHS RQs
Diglycidyl ether of bisphenol A	Not applicable	Not applicable

Canada

This product has been classified in accordance with the hazard criteria of the Controlled Products Regulations (CPR) and the MSDS contains all the information required by the CPR.

WHMIS Hazard Class
D2B Toxic materials

16. OTHER INFORMATION

Prepared By   Ana Santiago
Supercedes Date   10/19/2006
Issuing Date   04/08/2010
Reason for Revision   No information available.
Glossary   No information available.
List of References.   No information available.

Mega Metals,Partsmaster,Div of NCH Corp.assumes no responsibility for personal injury or property damage caused by the use, storage, or disposal of the product in a manner not recommended on the product label. Users assume all risks associated with such unrecommended use, storage or disposal of the product. The information provided on this MSDS is correct to the best of our knowledge, information and belief at the date of its publication. The information given is designed only as a guide for safe handling, use, processing, storage, transportation, disposal and release and is not to be considered as a warranty or quality specification. The information relates only to the specific material designated and may not be valid for such material used in combination with any other material or in any process, unless specified in the text.

List of Publications

o   P.T. Tran Diep, S.D. Pang, S.T. Quek (2011). Self-healing reinforced concrete: Feasability study with basic structural members. *Cement and Concrete Research* (submitting).

o   P.T. Tran Diep, S.D. Pang, S.T. Quek (2011). Does representative volume element exist for quasi-brittle materials? *Material Science and Engineering: Part A,* **528:**7757-7767.

o   S.D. Pang, P.T. Tran Diep, S.T. Quek (2011). Self-healing concrete structural members. *The 3rd International Conference on Self-Healing Materials* – June 27-29, 2011, Bath, UK.

o   S.D. Pang, P.T. Tran Diep, S.T. Quek (2011). Numerical simulation of micro-capsule based self-healing materials. *The 3rd International Conference on Self-Healing Materials* – June 27-29, 2011, Bath, UK.

o   P.T.Tran Diep, S.D. Pang, S.T. Quek (2010). Implementation of self healing in basic concrete structural members. *The 23rd KKCNN Symposium on Civil Engineering* – November 13-15, 2010, Taipei, Taiwan.

o   P.T.Tran Diep, S.D. Pang, S.T. Quek (2009). On implementation of self healing function in concrete – proof of concept and practical issues. *The 2nd International Conference on Self-Healing Materials* – June 28th to July 1st, 2009, Chicago, Illinois USA.

o   P.T. Tran Diep, T.J.S. Johnson, S.T. Quek, S.D. Pang (2009). Implementation of self healing in concrete. *The IES Journal Part A: Civil and Structural Engineering,* **2**:116-125.

o   P.T. Tran Diep, S.D. Pang, S.T. Quek (2008). Numerical model to capture the Young's modulus of self-healing material. *The First American Academy of Mechanics Conference* – June 17-20, 2008, New Orleans, USA.

THIS PAGE IS INTENTIONALLY LEFT BLANK